

POLITECNICO DI TORINO

Facoltà di Ingegneria I

Corso di Laurea in Ingegneria Biomedica

Tesi di Laurea Magistrale

**Adhesion, friction and wear on
nanoscale of MWNT probes and
CNT arrays**



Relatore:

Prof. Ing. Cristina Bignardi

Correlatore:

Ph.D. D.Sc.(Hon.) Bharat Bhushan

Candidata:

Barbara Galasso

Ottobre 2007

Acknowledgements

I would like to thank Prof. Bhushan for the opportunity he gave me to work in his laboratory. I would also like to sincerely thank all the NLIM researchers, in particular Dr. Xing Ling for the helpful discussions, and Dr. Manuel L. Palacio for his support during my stay at The Ohio State University.

Un grosso ringraziamento va alla mia Famiglia, per avermi permesso di vivere un'altra esperienza negli U.S.A., sostenendomi nel modo migliore possibile durante tutto il periodo.

Contents

Acknowledgements	i
Introduction	1
1 Scanning Probe Microscopy	3
1.1 Scanning Tunneling Microscopy	4
1.2 Atomic Force Microscopy	8
1.2.1 Contact Mode	11
1.2.2 Tapping Mode	14
1.3 AFM Probes	17
2 Friction and wear on the atomic scale	22
2.1 Friction Force Microscopy (FFM)	23
2.2 Force calibration	24
2.2.1 Friction force measurement techniques	25
2.2.2 The one-dimensional Tomlinson Model	38
2.2.3 The Frenkel-Kontorova-Tomlinson Model	39
2.3 Thermal effects on atomic friction	40
2.4 Geometry effects on atomic friction	43
2.4.1 The estimation of the contact area	45
2.5 Wear on atomic scale	46

2.5.1	Molecular dynamics simulations of atomic friction and wear	47
3	Carbon Nanotubes	50
3.1	Synthesis of Carbon Nanotubes	52
3.2	Mechanical properties of carbon nanotubes	56
3.3	Carbon nanotubes applications	59
4	Nanotribological characterization of carbon nanotubes	68
4.1	Experimental	71
4.1.1	AFM tips	71
4.1.2	Test samples	73
4.1.3	Adhesive force, friction force, and wear measurements	74
4.2	Results and discussion	76
4.2.1	Adhesive forces and friction measurements	76
4.2.2	Wear tests	84
	Conclusions	87
	Bibliography	89

Adesione, attrito ed usura alla nanoscala di punte AFM con MWNT e di array di SWNT e MWNT

I nanotubi in carbonio (CNT) furono scoperti da Iijima nel 1991 [1]. Essi esistono in tre forme: *single walled nanotubes* (SWNT) costituiti da un piano atomico di atomi di carbonio perfettamente arrotolato in un cilindro; *double walled nanotubes* (DWNT) formati da due strati di grafene (fogli di arrangiamenti grafiteici di atomi di carbonio); *multi walled nanotubes* (MWNT) caratterizzati da strutture cilindriche concentriche di grafene, nelle quali le interazioni fra i diversi strati sono dominate dalle forze di van der Waals [2]. Dalla loro scoperta, i ricercatori hanno studiato queste strutture nanometriche, documentandone le notevoli proprietà. Grazie alla loro unica struttura molecolare, alle eccellenti proprietà elettriche, ad una buona stabilità chimica e ad ottime proprietà meccaniche, i nanotubi in carbonio sembrano promettenti per una grossa varietà di applicazioni. La produzione in larga scala di tali nanostrutture fu avviata da Ebbesen e Ajayan [3], e proseguita da Iijima e Iichashi [4] e molti altri per il grosso interesse verso questo nuovo materiale. Nel 1995, de Heer ed i suoi collaboratori [5] svilupparono il primo metodo per allineare verticalmente i nanotubi su un substrato. L'attenzione sia della ricerca che dell'industria è ora concentrata sulla produzione di singoli nanotubi, compositi ceramici, metalli e polimerici, ed array di nanotubi. I nanotubi in carbonio sono interessanti per svariate applicazioni: emettitori di campo, transistor molecolari, dispositivi microfluidici,

biosensori, a fase dispersa in nanocompositi, dispositivi biomimetici, nanopinze, dispositivi funzionalizzati per applicazioni biomedica ed optoelettroniche, elettrodi per display a pannello piatto [6, 7, 8, 9, 10, 11, 12], e molte altre.

Grazie al loro piccolo diametro ed alla loro elevata resistenza meccanica, singoli nanotubi sono particolarmente indicati nell'impiego in punte per microscopi a forza atomica (AFM) [13, 14, 15]. Infatti, la geometria cilindrica e il piccolo diametro del nanotubo consentono la scansione in strette e profonde cavità, aumentando la risoluzione laterale in confronto a quella ottenibile con punte convenzionali [16].

Grazie alla loro resistenza meccanica, combinata alla loro bassa densità, i carbonanotubi sembrano particolarmente adatti all'utilizzo come fase dispersa in compositi con vari materiali. Diversi studi hanno dimostrato che l'uso di nanotubi in carbonio in matrici polimeriche possono migliorare notevolmente le caratteristiche meccaniche e tribologiche dei compositi [17, 18, 19, 20, 21, 22, 23]. Compositi metallici con i CNT sono interessanti per la loro alta resistenza all'usura [24, 25, 26, 27, 28], e le loro proprietà termiche, rendendoli adatti nell'impiego della gestione del calore in dispositivi ad alta potenza [29]. I nanotubi in carbonio sono anche stati aggiunti a matrici ceramiche. In particolare è stato dimostrato che possono aumentare la deformazione elastica e la resistenza alla frattura del SiC e dell'allumina [30, 31, 32, 29].

E' stato osservato che l'allineamento dei CNT rispetto alla superficie del substrato può aumentare l'emissione di campo di tali nanostrutture [33, 34], e può inoltre influenzarne le proprietà termiche [35]. E' pertanto di grosso interesse lo studio di array di carbonanotubi allineati sul substrato.

E' inoltre di notevole interesse la realizzazione di strutture organizzate in nanofibre usando array di CNT per varie applicazioni, includendo la mimica delle zampe dei gechi e l'effetto lotus [36, 37, 38, 39].

Focalizzandosi sull'impiego dei CNT in punte per AFM, nonostante siano già

stati riportati molti studi sulle loro caratteristiche, tutti sono stati svolti in tapping mode. Nguyen et al. [40] hanno analizzato la stabilità e la capacità risolutiva laterale dei CNT nelle punte per AFM, usando sia SWNT che MWNT. Acquisendo immagini in tapping mode, hanno confrontato la risoluzione raggiungibile usando punte con i nanotubi e punte convenzionali in silicio. Con questo studio, Nguyen e i suoi collaboratori hanno illustrato come la punta con il MWNT non si degrada dopo un lungo periodo di scansioni (oltre 15 ore) e come la punta con il SWNT consenta di raggiungere risoluzioni laterali fino a 2 nm. Larsen et al. [41] hanno comparato l'usura e la degradazione di commerciali punte in silicio inciso, con quella di punte con MWNT durante la scansione in tapping mode di campioni fragili, quali una superficie di silicio policristallino. I loro test hanno portato alla conclusione che usando una punta con un MWNT, né la sonda né il campione hanno risentito dell'acquisizione continua di oltre 1100 scansioni. In uno studio successivo, Guo et al. [42] hanno condotto un esperimento sulle caratteristiche di usura sia di punte con CNT che di punte in silicio. Il loro test ha portato alla conclusione che le punte col nanotubo sono resistenti all'usura, distinguendosi conseguentemente per buone caratteristiche anti usura e lunga resistenza nel tempo, in confronto alle punte in silicio; inoltre, le sonde con il nanotubo producono danni molto minori al campione analizzato, quando paragonate alle punte in Si.

Le proprietà meccaniche dei nanotubi in carbonio sono state studiate sia teoricamente che empiricamente. Le risposte elastiche non lineari e la resistenza meccanica di nanotubi e nanofibre sono stati analizzati da diversi ricercatori [43, 44, 45, 46, 47, 48, 49]. Yu et al. [50] hanno analizzato il meccanismo di frattura dei MWNT sottoposti a carichi di trazione, mentre Daraio et al. [51, 52] si sono soffermati sul meccanismo di nanoframmentazione dinamica e sull'interazione nonlineare al contatto e sulla risposta all'impatto di foreste di nanotubi in carbonio. Cao et al. [53] hanno riportato il comportamento a compressione completamente reversibile dei film

di nanotubi.

Oltre all'analisi delle proprietà meccaniche, la comprensione del comportamento nanotribologico, quale l'adesione e l'attrito, tra i nanotubi in carbonio e diversi materiali ha un ruolo chiave nell'esplorazione di nuove applicazioni per i CNT [54, 55]. Kinoshita et al. [56] hanno studiato il comportamento all'attrito di una foresta di nanotubi allineati verticalmente usando una punta per AFM in oro in aria. Turq et al. [57] hanno focalizzato il loro interesse sugli effetti dell'ambiente sulle proprietà tribologiche di nanotubi allineati verticalmente. I loro esperimenti sono stati svolti usando una punta in oro, e in ambiente ad umidità relativa controllata, variandola fra 0 e 100%. A causa della scala micrometrica della punta utilizzata e delle forze applicate, tali studi riguardano la caratterizzazione microtribologica dei nanotubi, più che la loro analisi su scala nanometrica. Per l'emergente potenziale dell'applicazione dei nanotubi in strutture che mimano le zampe dei gechi e l'effetto lotus, e in compositi al fine di migliorare specifiche proprietà, quali la conduttività elettrica o l'aumento della resistenza meccanica nei compositi polimerici, è ancora necessaria un'analisi dell'interazione fra i CNT e diversi materiali su scala nanometrica.

In questo contesto, un'accurata caratterizzazione nanotribologica delle sonde AFM con CNT è ancora necessaria, in termini di analisi di adesione ed attrito fra diversi materiali, così come una sua analisi della resistenza all'usura. Inoltre, una caratterizzazione tribologica di array di CNT è scarsamente riportata e focalizzata sull'analisi micrometrica della tribologia di nanotubi orientati.

Materiali e metodi

Sonde AFM

La sonda con il MWNT usata in questo studio è presentata in Fig.1. *Multiwalled carbon nanotubes* sono stati preparati in bassa densità e ben separati tra loro per

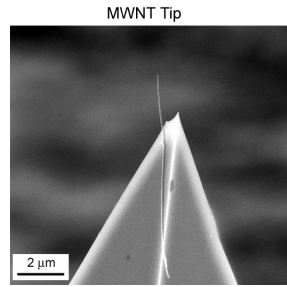


Figura 1: Immagine SEM della sonda AFM con il MWNT usata per lo studio

deposizione chimica in fase vapore (CVD) su un filo di Pt rivestito con una soluzione catalitica liquida descritta in [58]. Usando un microscopio invertito con un ingrandimento a 500x, un singolo MWNT di lunghezza superiore ai $10\ \mu\text{m}$ è stato trasferito sulla punta di un cantilever in silicio rivestito con un film di Ni spesso 15 nm. La posizione relativa del MWNT rispetto alla punta in silicio è stata manipolata manualmente usando un paio di microtrasduttori. Quando il nanotubo e la punta in silicio erano a distanza ravvicinata, è stato applicato un potenziale elettrico di 1-2 V al fine di migliorare l'allineamento del nanotubo col vertice della punta in Si. Una volta raggiunto l'allineamento desiderato, il MWNT è stato staccato dalla fonte aumentando il voltaggio a 10 V ed oltre. Il distacco avviene per effetto Joule in corrispondenza del punto lungo la lunghezza del nanotubo in cui si concentrano i difetti, a questa alta resistenza elettrica. Il voltaggio applicato ha causato anche un surriscaldamento localizzato all'interfaccia fra il MWNT e la punta in Si rivestita in Ni, rafforzando l'interfaccia probabilmente inducendo una saldatura fisica del nanotubo al film di Ni e/o creando dei legami chimici fra il MWNT e la punta in Si rivestita con il Ni. I diametri delle punte con i nanotubi generalmente variano fra 10 e 30 nm, con una lunghezza, oltre alla struttura silicica di sostegno, altamente variabile da qualche micrometro a decine di μm . I MWNT sono aperti, poiché il loro diametro è relativamente grosso affinché la chiusura possa avvenire con un cap. Il cantilever ha una frequenza di risonanza di di circa 75 kHz e una costante elastica

nominale di 2 N/m. L'effettiva lunghezza del cantilever è stata misurata con un microscopio ottico e risulta essere pari a circa 200 μm . L'altezza totale della punta, includendo la struttura silicica di supporto e la lunghezza del MWNT attaccato, è approssimativamente pari a 17 μm , e la lunghezza del nanotubo, sporgente dalla punta in Si, è di circa 2 μm , come si può notare in Fig.1.

Per confronto, una punta in silicio intagliato a modulazione di forza (RFESP, Veeco) e una punta in nitruro di silicio ossido-appuntita (NP-S, Veeco), sono state usate per le stesse misure di forza di adesione e coefficiente di attrito. Le punte in silicio RFESP sono ricavate da un wafer di silicio (100) dopato al fosforo (n) con 0.5-2 Ωcm , il quale viene lavato in una soluzione calda acquosa di HCl:H₂O₂:H₂O ed intagliato in una soluzione 6:1 di HF in acqua distillata tamponata con fluoruro di ammonio. Tale lavaggio continua con una soluzione di idrossido di potassio, una di acido fosforico caldo ed infine è seguito dall'intaglio mediante HF. Dopo l'intaglio, le punte sono state sciacquate in acqua distillata ed asciugate con nitrogeno che fluiva attraverso un tubo in plastica. La lunghezza del cantilever sulla punta è pari a 225 μm , la sua frequenza di risonanza nominale è pari a 75 kHz, con costante elastica nominalmente pari a 3 N/m. L'altezza nominale della punta è di 15 μm , con raggio di circa 10 nm. Le punte in nitruro di silicio sono sostenute da un cantilever con lunghezza nominale di 11 μm e costante elastica di 0.58 N/m. La loro altezza varia fra 2.5 e 3.5 μm , con raggio di punta nominale pari a 20-50 nm. I test sugli array di nanotubi allineati verticalmente sono stati condotti utilizzando due punte in silicio (RFESP, Veeco).

Campioni in analisi

Al fine di studiare l'effetto della punta con il MWNT in interazione con diversi materiali, i test sono stati condotti su un monocristallo di silicio (100), mica, monocristallo di alluminio e un film di oro. Il primo rappresenta i materiali ceramici,

gli ultimi due rappresentano metalli duttili. Il film d'oro ha uno spessore di 100 nm ed è stato depositato su un substrato di silicio mediante evaporazione.

Per la seconda parte dello studio sono stati testati due diversi array di nanotubi in carbonio allineati verticalmente (Fig.2). Un array è costituito da SWNT, con

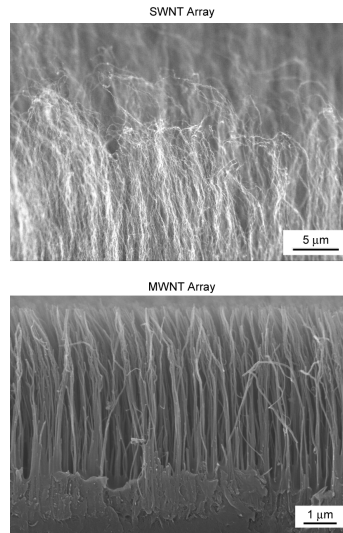


Figura 2: Immagini SEM degli array di nanotubi utilizzati nello studio

diametro inferiore ai 5 nm. Il secondo array è realizzato con MWNT, con diametri compresi fra 20 e 50 nm. Per entrambi gli array, la lunghezza dei nanotubi è di 5-10 μm . I nanotubi sono aperti senza cap di chiusura. I SWNT allineati sono stati sintetizzati dalla deposizione di ~ 1 nm Fe su un substrato di Al (~ 10 nm) rivestito con SiO_2/Si , seguita da un processo di PECVD (80 W, 13.56 MHz) di ~ 30 mTorr di C_2H_2 per 10-15 min a 750 $^\circ\text{C}$. Dopo la sintesi, i SWNT sono stati trasferiti su un film d'oro tramite rivestimento per sputtering, seguito da un intaglio in una soluzione acquosa di HF al 10% [59]. L'allineamento del campione di MWNT su polimero è stato eseguito secondo il metodo proposto da Qu e Dai [60]. Un appropriato film polimerico sottile, polistirene (PS) nel caso in esame (peso molecolare $M_w = 350.000$; temperatura di transizione vetrosa $T_g \sim 105$ $^\circ\text{C}$; punto di fusione $T_m \sim 180$ $^\circ\text{C}$; temperatura di decomposizione $T_c \sim 350$ $^\circ\text{C}$; spessore ~ 50 μm), è

stato inizialmente posizionato sulla superficie superiore del film di nanotubi [59]. Riscaldando il substrato di SiO₂/Si tramite posizionamento su un piatto ad una temperatura superiore a T_m ma inferiore a T_c, il film fuso di PS gradatamente penetra nella foresta di nanotubi per effetto combinato di gravità e forze capillari. La profondità di penetrazione del PS all'interno della foresta dipende fortemente dalla temperatura e dal tempo di riscaldamento. Dopo un tempo di riscaldamento prestabilito, l'array di nanotubi infiltrati con il polimero è stato rimosso dal substrato di SiO₂/Si in una soluzione acquosa di HF al 10% in peso per ottenere un film di nanotubi con un'estremità libera allineati verticalmente sulla matrice polimerica.

Misure di adesione, attrito ed usura

Le forze di adesione ed attrito sono state misurate usando un MultiMode AFM (Digital Instruments, Santa Barbara, CA). La calibrazione della forza di adesione e le misure di attrito con la punta in silicio ed in Si₃N₄ sono stati eseguiti su una linea di scansione di 2 μm di lunghezza, con una velocità di scansione di circa 4 μm/s (corrispondente a una frequenza di scansione di 1 Hz) ed un angolo di scansione di 90°, applicando un carico normale in variazione fra 0 e 250 nN. Sono stati realizzati tre set di misure per ciascuna punta su ogni campione, eseguendo 3 cicli di carico e scarico [55]. I relativi coefficienti di attrito sono stati valutati seguendo il metodo II presentato da Ruan e Bhushan [61]. Il coefficiente di attrito è ottenuto dalla pendenza della curva del carico normale in funzione del valore medio di TMR (Trace minus retrace), i cui valori sono monitorati durante la scansione della punta in direzione perpendicolare all'asse del cantilever. Con la punta col nanotubo, sono stati utilizzati gli stessi settaggi, ad eccezione dell'angolo di scansione, che è stato imposto pari a 0° al fine di scansionare la punta lungo l'asse longitudinale del cantilever, come previsto dal metodo I della procedura sviluppata da Ruan e Bhushan [61]. I relativi coefficienti d'attrito sono stati valutati dalla pendenza della curva

della posizione del cantilever lungo l'asse Z in funzione del valore medio del TMR. I dati di attrito sono stati raccolti con 3 cicli di carico e scarico su 3 aree diverse per ogni campione.

I test di attrito sono stati svolti su un'area di $2 \times 2 \mu\text{m}^2$, con una velocità di scansione di $4 \mu\text{m/s}$, applicando al cantilever due carichi normali di 100 nN e 200 nN [55]. Al fine di analizzare l'usura del campione, dopo ciascun test le superfici sono state scansionate in tapping mode. Per la valutazione dell'usura della punta è stato seguito il metodo proposto da Tao e Bhushan [62]. Quando si scansiona una struttura localizzata molto più appuntita della punta stessa, l'immagine risultante è l'immagine della punta. Basandosi su questo principio, è stato scansionato il grating di silicio TGT1 (NTMTD, Mosca, Russia) con una delle punte in silicio e la punta col nanotubo. Tale grating è caratterizzato da un array di punte acuminate sulla superficie, organizzate su ogni angolo ed al centro di un quadrato di $3 \times 3 \mu\text{m}^2$ di area. L'altezza di ogni punta è pari a $0.4 \mu\text{m}$, l'angolo di punta è di circa 30° ed il raggio è inferiore ai 10 nm. La scansione è stata svolta su un'area di $2 \times 2 \mu\text{m}^2$, ad una velocità media della punta di $2 \mu\text{m/s}$, corrispondente a una frequenza di 0.5 Hz, lungo la direzione parallela all'asse del cantilever. Il software SPIP (Image Metrology A/S, Danimarca) è stato utilizzato per la caratterizzazione delle punte utilizzate per i test, e per la stima dei loro raggi e angoli di conicità. Il profilo delle punte è stato generato mediante l'algoritmo di ricostruzione cieca dall'immagine del campione TGT1. Per ogni punta è stato ottenuto un profilo bidimensionale. La caratterizzazione della forma della punta col nanotubo utilizzando il software descritto non è stata possibile a causa della struttura del nanotubo. Infatti, essendo esso caratterizzato da una punta aperta, il suo raggio è infinito; non è quindi possibile ottenerne un'immagine utilizzando il grating in silicio.

Tutti gli esperimenti sono stati svolti in condizioni ambientali, a $22 \pm 1 \text{ }^\circ\text{C}$ e 45-55% di umidità relativa.

Risultati e discussione

Forze di adesione e misure d'attrito

Punta con il MWNT su campioni di Si, Al e mica

Le curve di calibrazione della forza ottenute durante le misure dell'adesione, riportate in Fig.3a, mostrano un comportamento nonlineare che può essere ricondotto alle interazioni fra la punta ed il campione. Il nanotubo sulla punta entra in contatto con la superficie al punto A; man mano che il cantilever viene pressato contro il campione, le forze di contatto causano una deflessione lineare del cantilever. Dopo questa flessione iniziale, mentre la punta viaggia verso la superficie (da B a C), la deflessione del cantilever (e di conseguenza il carico) resta pressoché costante, mostrando qualche variabilità. Un comportamento nonlineare simile è stato precedentemente osservato operando l'AFM in tapping mode [63]. Tale andamento nonlineare indica che, durante la pressione della sonda contro la superficie, il MWNT è indotto a flettersi e ad ingobbirsi, e la deflessione del nanotubo risulta superiore a quella del cantilever (Fig.3b). E' stato osservato che, durante il cedimento elastico, o *buckling*, i legami grafitici C-C, più nello specifico i legami σ e π lungo le catene ibridizzate sp^2 , si trasformano dall'ibridazione sp^2 all'ibridazione sp^3 quando un carico meccanico è applicato lungo l'asse del nanotubo. Tale trasformazione è dovuta alla rottura dei legami C-C π ed è reversibile dal momento che l'ibridazione sp^2 è termicamente più stabile dell'ibridazione sp^3 [64]. Il nanotubo si imbozza finché la forza applicata non raggiunge il valore della forze di Eulero [65]:

$$F = \frac{2EI}{L^2} \quad (1)$$

dove E è il modulo elastico del nanotubo (~ 1 TPa, [46]), I è il momento d'inerzia ($I = (r_2^4 - r_1^4)/4$, con r_1 ed r_2 rispettivamente raggio interno ed esterno del nanotubo,

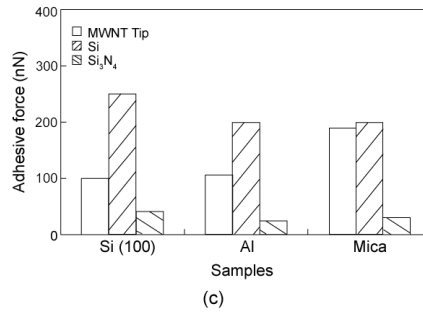
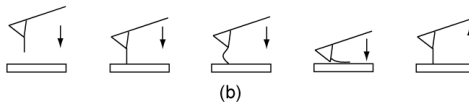
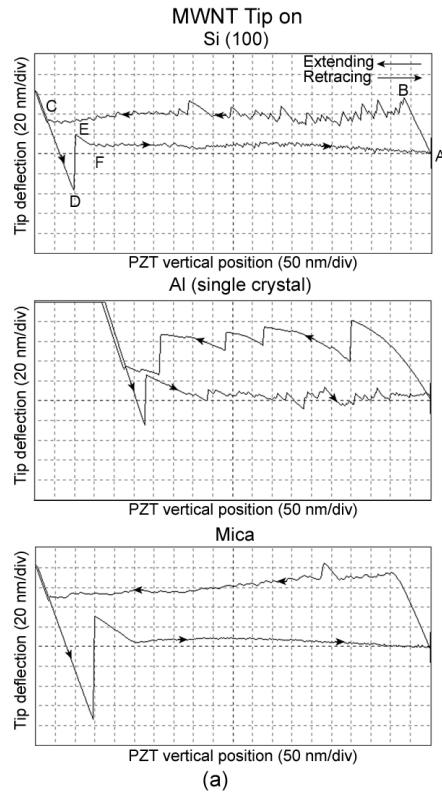


Figura 3: (a) Curve di calibrazione della forza per la punta con il MWNT in interazione con tre diversi campioni; (b) schema del *buckling* del nanotubo e della sua flessione durante la calibrazione della forza; (c) istogramma dei valori medi delle forze di adesione valutate con tre punte su tre campioni. La deviazione standard dai valori media è di circa il 20%

con $r_2 \sim 10$ nm per la punta in uso) ed L la lunghezza del nanotubo ($\sim 2 \mu\text{m}$). Per valori di carico superiori alla forza di Eulero, il MWNT diventa elasticamente instabile ed inizia a cedere lateralmente, adagiandosi sulla superficie e strisciandovi. La forza di *buckling* per la punta in studio è stata valutata attorno ai 20 nN. Ciò suggerisce che, dal momento che il carico applicato al punto B (circa 100 nN) è dell'ordine della forza di Eulero, il nanotubo si ingobbisce dal punto B al punto C, adagiandosi poi lateralmente lungo la superficie. L'attrito tra il nanotubo e la superficie caratterizzata da rugosità, e la continua flessione del nanotubo, sono responsabili delle oscillazioni osservabili tra i punti B e C.

Al punto C, la punta silicica che supporta il MWNT entra in contatto con la superficie, inducendo una deflessione lineare del cantilever. Quando la sonda è ritratta dal piezo (punto D), la forza elastica del cantilever supera l'adesione tra la punta ed il campione e la punta in Si perde il contatto (punto E). Dopo che la punta interrompe il contatto (punto E), l'energia elastica immagazzinata dal MWNT è rilasciata (da E ad F). Dopodiché il nanotubo ancora piegato, gradualmente scarica la tensione accumulata precedentemente durante il regime di estensione del piezo, quando la punta si allontana dal campione. Da tale processo è ragionevole aspettarsi la generazione di una forza repulsiva comparabile a quella mostrata da Lee et al. [66] nel regime di estensione. Comunque ciò è in contraddizione con quanto osservato, dal momento che la deflessione del cantilver durante il regime di ritrazione F-A è notevolmente inferiore rispetto a quella presente nel regime di estensione B-C. La discrepanza qui può essere spiegata dall'inversione del verso della scansione tra il MWNT ed il campione. La forza di attrito inverte il verso quando la punta in silicio si stacca dalla superficie, riducendo la tensione immagazzinata nel nanotubo anziché aumentarla come nel regime di estensione B-C. Inoltre, la deflessione al punto E si trova esattamente al centro fra il punto C ed il punto F, in corrispondenza di uno stato intermedio prima che la forza di attrito inverta il verso.

Dai grafici di calibrazione della forza sono state valutate le forze adesive (D-E), ed i valori corrispondenti sono riportati in Tab.1. Si tratta di una combinazione di

Sample	Tip		
	Si	Si ₃ N ₄	CNT
Si	80	250	40
Al	150	200	25
Mica	200	200	30

Tabella 1: Forze di adesione (nN) per diverse punte su tre campioni

contributi derivanti dall'adesione fra la punta in silicio che supporta il nanotubo e dal MWNT piegato sulla superficie, oltre agli stress elastici immagazzinati dal nanotubo. Sebbene non si possa escludere la possibilità che durante l'istante di interruzione del contatto il MWNT giacente sulla superficie sia lentamente rimosso dalla superficie, il contributo all'adesione misurata derivante dalla rimozione graduale del MWNT può essere trascurata con un buon margine di sicurezza, dal momento che la lunghezza della porzione di nanotubo allontanato dalla superficie dovrebbe essere inferiore alla distanza del salto fuori dal contatto (pari a 50 nm), il quale è molto inferiore alla lunghezza del nanotubo in uso ($\sim 2 \mu\text{m}$).

Inoltre, come riportato da Barber et al. [67], i CNT hanno un angolo di contatto di circa 80° , e sono bagnati più facilmente dall'acqua rispetto alla grafite per l'alto componente polare dell'energia superficiale, ma la loro struttura è ancora idrofobica. Quindi ogni forza capillare interattiva derivante dalla porzione di nanotubo distaccata dalla superficie non dovrebbe contribuire in modo influente sull'adesione riscontrata. Tali valori potrebbero essere attribuiti alla combinazione del nanotubo piegato ed in contatto strisciante con la superficie e della punta in Si in contatto statico con il campione.

Ai fini di confronto, le forze adesive sono state anche valutate usando una punta in Si ed una in Si₃N₄, ed i dati sono riportati in Fig.3c. L'adesione cui è soggetto il silicio è la maggiore, e ciò può essere giustificato con l'elevata forza capillare a

cui tale materiale è sottoposto a causa del suo basso angolo di contatto, pari a 51° [62]. Il nitruro di silicio è caratterizzato da un angolo di contatto di 48° , quindi la forza di adesione dovrebbe avere intensità comparabile a quella osservata per la punta in silicio. Le differenze riscontrate potrebbero essere ricondotte alle differenze nell'energia superficiale [54].

Il coefficiente di attrito per il MWNT è stato calcolato durante lo scorrimento su diverse superfici, ed i dati raccolti sono presentati in Fig.4 ed in Tab.2.

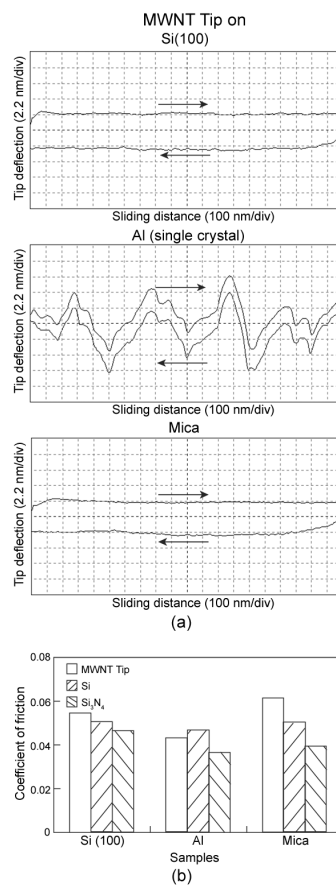


Figura 4: (a) Deflessione verticale a carico costante (100 nN) del cantilever durante le misure di attrito; (b) valori medi dei coefficienti di attrito. La deviazione standard è circa 15%

Samples	Tips		
	Si	Si ₃ N ₄	CNT
Si	0.051	0.047	0.054
Al	0.047	0.037	0.043
Mica	0.050	0.040	0.061

Tabella 2: Coefficienti di attrito di diverse punte su vari campioni

I coefficienti di attrito stimati per la punta con il MWNT risultano avere valori leggermente superiori ai corrispettivi ottenuti con le punte in Si e Si₃N₄. Tale andamento può essere dovuto ad una combinazione della chimica superficiale ed alla flessione del nanotubo durante la scansione. Mentre la sonda è pressata contro la superficie in esame, il nanotubo cede elasticamente e si piega lateralmente, inducendo un aumento dell'area di contatto, che provoca una maggiore resistenza al moto della punta. Nel caso particolare del campione di alluminio, le grosse variazioni del segnale della deflessione laterale sembra siano la conseguenza dell'elevata rugosità superficiale che lo caratterizza.

Punte in Si sugli array di SWNT e MWNT

Gli esperimenti di adesione sono stati condotti anche sugli array di SWNT e MWNT, le cui immagini AFM sono riportate in Fig.5. I dati raccolti sono riportati

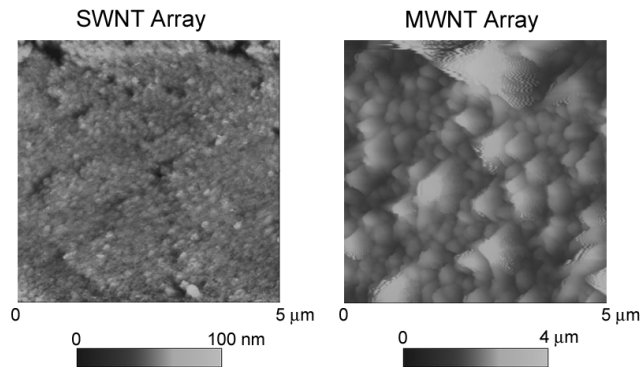


Figura 5: Immagini AFM degli array di SWNT (a sinistra) e di MWNT (a destra)

in Fig.6 ed in Tab.3.

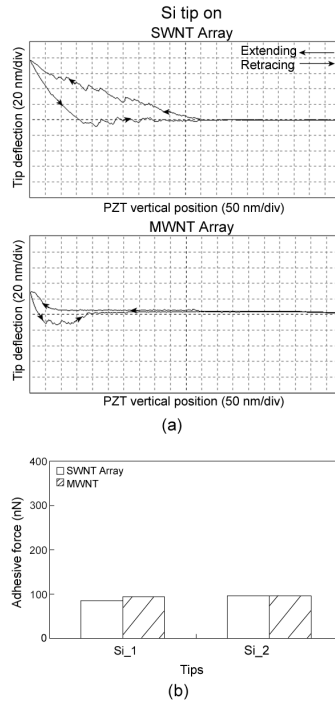


Figura 6: (a) Curve di calibrazione della forza fra le punte in Si e gli array di nanotubi; (b) valori medi della forza di adesione. La deviazione standard di tali valori è pari al 40%

Samples	Tips	
	Si ₁	Si ₂
Si ₁	86	96
Si ₂	94	96

Tabella 3: Forze di adesione (nN) fra le punte in Si e gli array di SWNT e di MWNT

Analizzando le forze di adesione presentate in Fig.6b, è possibile notare come i valori di adesione siano inferiori per l'array di SWNT in confronto a quello di MWNT.

Le curve di calibrazione della forza per la punta in Si sui due array di CNT sono mostrate in Fig.6a. Da tali grafici è possibile osservare che, una volta che è

avvenuto l'effettivo contatto fra la punta ed il campione, man mano che la distanza punta-campione si riduce, il cantilver è delicatamente deflesso finché il piezo non ritrae la punta in un profilo lineare, il cui andamento è comunque diverso da quello tradizionalmente osservabile per campioni omogenei. Ciò può essere spiegato come segue: man mano che la punta è spinta in profondità all'interno dell'array, un maggior numero di nanotubi entra in contatto con la sonda, contribuendo gradatamente alla sua repulsione. Tale condizione è opposta quando la punta viene allontanata dalla superficie, portando ad avere curve di retrazione nonlineari. Le forze di adesione osservate in questo caso derivano dalle forze di van der Waals conseguenti al contatto tra la punta e diversi nanotubi allo stesso momento, o ad un'ampia area di contatto tra la punta ed un singolo nanotubo per effetto della sua elevata flessibilità.

Nonostante i nanotubi siano idrofobici, le forze capillari potrebbero comunque rappresentare un contributo importante nell'adesione fra il silicio ed i CNT per via dell'alta energia superficiale dei nanotubi [36]. E' stato dimostrato che per foreste di nanotubi, con lunghezze pari a 10-15 μm , l'angolo di contatto iniziale è di 161° ; in ogni caso le gocce non sono stabili e dopo pochi minuti si infiltrano nei vuoti della foresta. Per CNT più corti, le gocce penetrano immediatamente nei vuoti ed i nanotubi sono anche forzati in raggruppamenti per effetto della tensione superficiale dell'acqua in evaporazione all'interno dell'array, riducendone conseguentemente l'idrofobicità. I grafici di calibrazione della forza monitorati durante le misure sono simili a quelli presentati da Decossas et al. [68] nei loro test su tappeti di CNT (dove i nanotubi non sono allineati) con una punta in nitruro di silicio; ed ai grafici riportati da Yurdumakan et al. [37], ottenuti scansionando una punta in silicio su un array di MWNT. Nei valori di adesione è stata osservata grossa variabilità, ed è possibile che ciò sia dovuto alla diversa organizzazione dei nanotubi in diversi punti dei campioni, considerando anche la diversa densità (Fig.5).

I dati di attrito rilevati per gli array di SWNT e MWNT sono riportati in Tab.4

e schematizzati in Fig.7.

Samples	Tips	
	Si 1	Si 1
SWNT	0.223	0.132
MWNT	0.309	0.256

Tabella 4: Coefficienti di attrito valutati con due punte in Si sugli array di SWNT e di MWNT

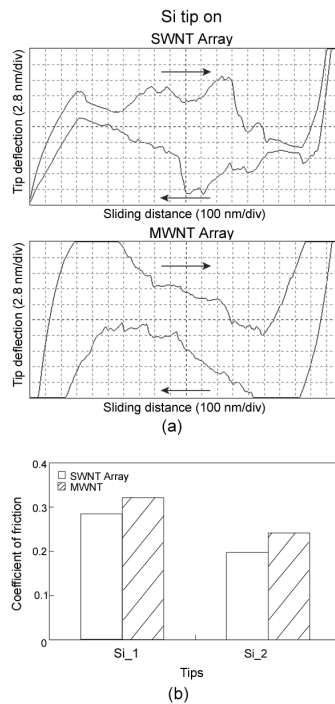


Figura 7: (a) Deflessione laterale del cantilever durante le misure di attrito; (b) valori medi dei coefficienti di attrito ($\sigma=20\%$) rilevati con le punte in Si sugli array di CNT

Il coefficiente di attrito stimato per l'array di SWNT ha un valore inferiore a quello osservato per l'array di MWNT, seguendo lo stesso andamento della forza di adesione. Oltre alla diversa densità, la maggiore rigidezza dei MWNT, rispetto ai SWNT, potrebbe contribuire all'elevato attrito riscontrato. I SWNT hanno una costante di flessione inferiore, dal momento che il loro diametro è minore, quindi sono

meccanicamente più flessibili rispetto ai MWNT ed oppongono minore resistenza al moto della punta.

Le forze di coesione fra i nanotubi nell'array possono influenzare il comportamento tribologico, ed è verosimile che tali forze siano maggiori nel campione di MWNT dal momento che la loro densità è superiore a quella dei SWNT nell'array verticale.

Test di usura

Sonda con il MWNT e punta in Si su un film d'oro

Le mappe d'usura sul campione di oro sono presentate in Fig.8. Si può notare

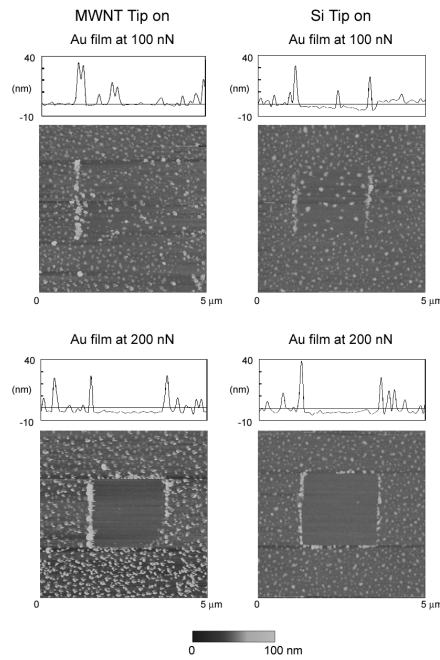


Figura 8: Immagini AFM e profili della superficie del film di oro usato per i test d'usura. Le immagini di sinistra sono ottenute con la punta alla quale è attaccato il MWNT, quelle di destra mediante la punta in Si

come l'usura indotta sul campione dopo il test condotto con un carico di 100 nN sia molto limitata, e come il materiale sia stato spinto lungo la direzione di scansione

della sonda. Le variazioni topografiche sono maggiormente evidenti nel campione usurato con la punta in Si. In particolare, è difficile quantificare una profondità di usura nel campione scansionato con la punta con il MWNT, mentre la profondità di usura indotta dalla punta in Si è quantificabile attorno ai 3 nm. La minore usura legata all'uso della sonda con il nanotubo può essere dovuta al cedimento elastico del nanotubo durante la scansione, il quale può assorbire parte della forza al contatto comportandosi come una molla compliante moderando l'impatto della punta sulla superficie [41, 58]. Inoltre, il diametro del nanotubo, inferiore rispetto al diametro della punta in Si, offre una minore area di contatto sul campione, danneggiandola conseguentemente di meno [54, 42]. Applicando un carico di 200 nN, i danni indotti al film d'oro sono praticamente gli stessi per le due punte usate, ed in media la profondità di usura è di 5 nm sia per la punta con il MWNT che per la punta in Si. Tale risultato può suggerire che sotto tale carico la punta in silicio che sostiene il nanotubo possa essere anch'essa in contatto con la superficie, potando ad un comportamento simile nel caso di entrambe le punte.

Punta in Si su array di SWNT e MWNT

Le immagini topografiche degli array di SWNT e MWNT dopo i test d'usura sono le stesse presentate in Fig.5, indicando che non è stato provocato alcun danno su nessuno dei due campioni. I profili della punta prima e dopo i test sono riportati in Fig.9. Da tale figura si può osservare come la sonda si sia usurata. Sebbene i cambiamenti della forma della punta dopo i test sull'array di SWNT siano trascurabili, il profilo della sonda varia dopo gli esperimenti sui MWNT. Inoltre, sembra che il profilo della punta dopo il test col carico di 100 nN sia più appuntito, ma ciò può essere attribuito ad un accumulo di materiale sulla punta stessa. Per quel che concerne la divergenza alla distanza di circa 300 nm nei profili ottenuti dopo i test sui MWNT, può essere dovuta ad artefatti del grating in silicio utilizzato per la

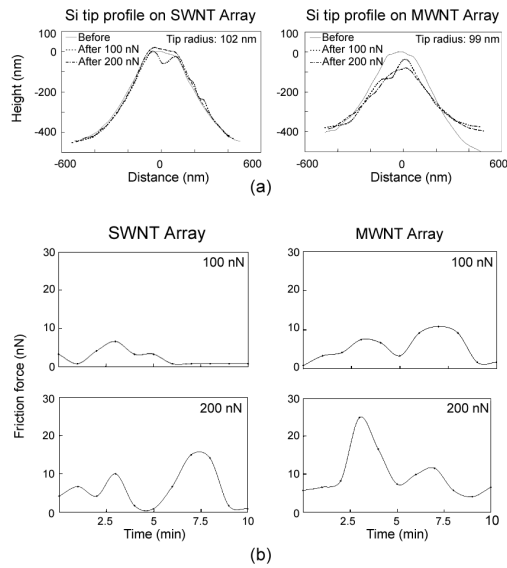


Figura 9: (a) Profili della punta in Si prima e dopo i test d’usura sugli array di CNT; (b) andamenti delle forze di attrito durante i test

generazione dell’immagine. Il volume d’usura della punta causato dall’interazione con i MWNT è stato calcolato con la procedura sviluppata da Tao e Bhushan [62] ed è, in prima approssimazione, pari a $34 \cdot 10^4 \text{ nm}^3$ dopo il test svolto con un carico di 100 nN, ed a $51 \cdot 10^4 \text{ nm}^3$ dopo il test a 200 nN. Tali valori sono comparabili con quelli riportati da Tao e Bhushan [62] per punta in Si su campioni in Si a carichi normali applicati pari a 100-200 nN.

I valori della forza di attrito monitorati durante i test sono presentati in Fig.9b. Il valor medio di tale forza, durante tutto il periodo degli esperimenti svolti, è maggiore quando la punta è scansionata sull’array di MWNT; di conseguenza è ragionevole riscontrare dell’usura sulla punta quando questa interagisce con tale campione. Le cause nel diverso comportamento dei due array e nelle fluttuazioni della forza di attrito sono le medesime presentate precedentemente nella sezione relativa all’adesione ed all’attrito.

Conclusioni

In questo studio è stata svolta un'analisi completa di adesione, attrito ed usura dei nanotubi in carbonio.

Dall'analisi dell'adesione si può concludere che, quando la punta con il MWNT è portata in contatto e successivamente distaccata dalla superficie, essa mostra un comportamento nonlineare dovuto principalmente alla flessione ed al cedimento elastico del nanotubo, portando ad un'alta area di contatto ed allo strisciamento del MWNT lungo la superficie del campione. Inoltre, sono stati osservati valori relativamente elevati della forza di adesione, e ciò si ritiene sia dovuto ad un contributo derivante dalla punta in silicio al quale è attaccato il nanotubo, la quale potrebbe essere in contatto con la superficie. La flessione ed il cedimento elastico del nanotubo, oltre alla chimica superficiale, possono essere anche la causa dei valori dei coefficienti di attrito stimati con la punta con il nanotubo, relativamente elevati rispetto a quelli ottenuti usando la punta in Si ed in Si_3N_4 sui campioni di Si, Al e mica. Quando il nanotubo si flette, si crea una conseguente elevata area di contatto che provoca una maggiore resistenza al moto della sonda.

Le forze adesive valutate tra le punte in Si e gli array di SWNT e MWNT sono affette da una grossa variabilità. Ciò è legato alla densità ed all'arrangiamento dei nanotubi all'interfaccia. Inoltre, i valori relativamente elevati di tali forze osservati per l'array di MWNT, possono essere dovuti alla presenza di elevate forze di van der Waals derivanti dal contatto della punta con numerosi nanotubi allo stesso istante, o ad un'ampia area di contatto fra la punta ed un singolo nanotubo. Il coefficiente di attrito stimato per l'array di SWNT è inferiore a quello relativo all'array di MWNT. Tale fatto può essere la conseguenza di minori intensità per le forze di van der Waals ed una maggiore flessibilità dei single walled nanotubes, che assecondano più che opporsi al moto.

I test di usura condotti sul film d'oro con due carichi normali mostrano un minor

danno quando è stata utilizzata la punta con il MWNT ed il carico minore tra i due. Ciò può essere legato al *buckling* del nanotubo, che si comporta come una molla compliant, assorbendo parte della forza trasmessa dal cantilever. Quando è stato applicato il carico di 200 nN non è stata osservata alcuna differenza nelle tracce d'usura sulle superfici scansionate con entrambe le sonde. E' quindi possibile concludere che tale carico possa portare la punta in silicio che supporta il nanotubo in contatto con il substrato.

Test di usura sono stati condotti sull'array di SWNT e MWNT usando una punta in Si, e non sono stati osservati cambiamenti topografici in nessuno dei due campioni. La punta mostra un'usura trascurabile dopo l'interazione con i SWNT, mentre un maggiore danno si può osservare dopo i test sui MWNT. Ciò è coerente con l'andamento delle forze di attrito monitorate durante i test: il valor medio della forza di attrito fra la punta e l'array di SWNT è leggermente inferiore al corrispettivo valore per i MWNT. E' possibile concludere che la maggiore flessibilità dei nanotubi giochi un ruolo fondamentale nell'interazione con la punta, permettendo ai nanotubi di flettersi più che di opporsi al moto e, conseguentemente, usurare la sonda.

Introduction

Carbon nanotubes (CNTs) were discovered in 1991 by Iijima [1]. Since then, researchers have been studying these nanometer-scale structures and have discovered their extraordinary properties. Due to their unique molecular structure, outstanding electrical properties, good chemical stability and excellent mechanical properties, carbon nanotubes seem promising for a variety of applications. The nanotribological characterization of carbon nanotubes is fundamental for the exploration of new sliding purposes, therefore a comprehensive investigation of adhesion, friction and wear of such structures has been carried out in this study.

The research has been performed at the Nanotribology Laboratory for Information Storage and MEMS/NEMS (NLIM) at the Ohio State University (Columbus, Ohio). The NLIM's main goal is to advance basic understanding of the nanotribology and nanomechanics which control the friction, wear and lubrication between two interacting surfaces in relative motion, and to develop methods for predictive reliability performance in electromechanical components and systems. Instrumentation used in this lab includes atomic force microscopy/scanning tunneling microscopy, microtriboapparatus, nanoindenter and industrial simulators.

In the present-day context, analyzed in Chap.4, an accurate nanotribological characterization of CNT AFM tips is still needed, in terms of adhesive and friction investigation on different materials, as well as a wear resistance analysis. Moreover,

a tribological characterization of CNT arrays is scarcely reported and focused on the micrometer scale analysis of the tribological behavior of aligned carbon nanotubes. The goal of this study is to systematically explore the nanotribological properties of the carbon nanotubes, both as part of an AFM tip, and organized in vertically aligned arrays. In particular, the objective is to evaluate adhesion and friction properties on nanoscale using MWNT, Si and Si₃N₄ tips on silicon, aluminum and mica samples, and using Si tips on SWNT and MWNT arrays. The intention is also to analyze the wear after tests at two normal loads using the MWNT tip and a Si tip on a gold film, and a Si tip on the SWNT and MWNT arrays.

This characterization of the tribological properties of the CNTs has been carried out using an atomic force microscope. Its principle of operation, and an overview of the scanning probe microscopy techniques, of which AFM is a particularity, are presented in the first chapter of this essay. SPMs have become of increasing interest in the recent years, due to their allowance of investigation and manipulation of surfaces down to the atomic scale. Atomic processes cannot be neglected when interpreting nanotribology experiments. Even on well-defined surfaces, experiments have revealed that atomic structure is directly linked to friction force. Chapter 2 will describe friction force microscopy experiments that reveal atomic processes during sliding contact. In the following section, the structures, the syntheses and growth methods and the mechanical properties of the carbon nanotubes will be described. Such structures look very promising for many different applications, some of which are presented at the end of the chapter. Chapter four deals with the actual study carried out. It contains the description of the experimental and the nanotribological properties found on the CNTs during the adhesive, friction and wear tests performed using a MWNT tip and on vertically aligned CNT arrays.

Chapter One

Scanning Probe Microscopy

Since the beginning of the ancient science, man has been interested in seeing and understanding the structure of objects and bodies, seeking for always finer details. This curiosity led to the development of microscopy, whose exact origin is hard to define.

The term *microscopy* comes from the Greek words *mikros*, meaning small, and *skopeo*, looking at. It refers to the microscopic investigation of the surface of different kind of samples. From this study, it is possible to obtain an image of the surface morphology, or even to get some information about some propriety characterizing the material that constitutes the sample. Depending on the kind of the microscope used, and on its magnification, the morphology of the sample surface shows the structure on a scale ranging from the macroscale to the nanoscopic one.

With the modern microscopes, such as scanning probe microscopes (SPMs), it

is possible to map the surfaces, obtaining maps of a particular physical or chemical propriety, such as elasticity, adhesion, friction and many others. The term scanning probe microscopy refers to those investigating techniques based on probe microscopes. SPMs scan the surface of specimens with a physical probe, obtaining topographies of the surface. Exploiting the interactions between the probe and the sample it is even possible to analyze quantitatively tribological, electrical, magnetic, biological and chemical properties of the surface itself. This feature made the SPMs more and more interesting in the recent years. Their applications in many different fields, either of scientific or industrial interests, has increased since their introduction, due to the fact that they can be used to investigate and manipulate surfaces down to the atomic scale.

Scanning probe microscopes include different families of instruments: scanning tunneling microscopes (STM), atomic force microscopes (AFM), friction force microscopes (FFM or LFM), scanning electrostatic force microscopes (SEFM), scanning force acoustic microscopes (SFAM), scanning magnetic microscopes (SMM), scanning near-field optical microscopes (SNOM), scanning thermal microscopes (SThM), scanning electrochemical microscopes (SEcM), scanning Kelvin probe microscopes (SKPM), scanning chemical potential microscopes (SCPM), scanning ion conductance microscopes (SICM), and scanning capacitance microscopes (SCM).

1.1 Scanning Tunneling Microscopy

The first SPM proposed was the scanning tunneling microscope, based on the principle of electron tunneling discovered by Giaevier in 1960. By applying a potential difference to two metal surfaces divided by a thin insulating film, electrons would cross the potential barrier causing a current flow. The variable measured with this instrument is then the tunneling current. To be able to measure such current, it

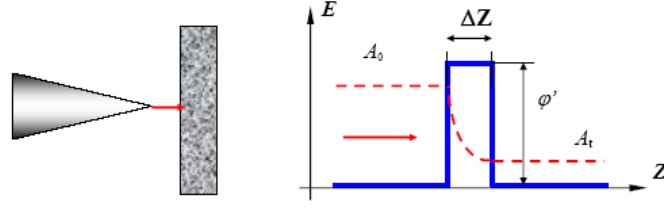


Figure 1.1: STM scheme of principle

is necessary to use a metallic tip and a conductive sample, and they must be spaced no more than 10 nm apart. In this configuration, the height of the potential barrier is a function of the work function from the tip (φ_T) and from the sample (φ_S). The average barrier function shape can be approximated to a rectangular shape where the height is given by the mean value of the two work functions φ' (Fig.1.1):

$$\varphi' = \frac{1}{2}(\varphi_T + \varphi_S) \quad (1.1)$$

According to the quantum mechanics theory, transmission coefficient through a rectangular barrier is given by:

$$W = \frac{|A_t|^2}{|A_0|^2} \cong e^{-k\Delta Z} \quad (1.2)$$

where:

- A_0 is the amplitude of the electrons wave function hitting the barrier;
- A_t is the amplitude of the transmitted electrons wave function;
- k is the attenuation coefficient of the wave function inside the barrier;
- ΔZ is the width of the barrier.

If the tunneling effect occurs between two metals, the coefficient value is:

$$k = \frac{4\pi\sqrt{2m\varphi'}}{h} \quad (1.3)$$

where:

- m is the electron mass;
- φ' is the work function needed to extract one electron from the surface;
- h is the Plank constant.

Applying a bias voltage V_T between the two conductive surfaces the tunneling current J_T is generated. In order to make such current measurable, the operating voltage value has to be in the range of 10 mV-1V. In this case the tunneling current varies between 0.2 and 10 nA, according to its dependence to the bias voltage:

$$J_T = J(V_T)e^{-k\Delta Z} \quad (1.4)$$

With a work function of a few eV, usually around 4 eV, the attenuation coefficient values about 2 \AA^{-1} . This leads to changes of an order of magnitude of J_T for an angstrom change of ΔZ .

According to the exponential Eq.1.4 it is possible to control the gap between the tip and the sample with great accuracy. If the current is kept constant to within 2%, the gap remains constant to within 1 pm.

A scanning tunneling microscope is therefore an electromechanical device based on a negative feedback control which keeps the tunneling current constant to the I_0 value imposed by the user. It was first introduced by Binnig et al., who used vacuum tunneling combined with lateral scanning. With that configuration, the vacuum provides the ideal barrier for tunneling, and the lateral scanning allows imaging the surface with a resolution sufficient to define the position of single atoms. The vertical resolution can be less than 0.1 nm thanks to the exponential dependence of the tunneling current to the tip-sample distance, as mentioned above. The lateral resolution, typically less than 1 nm, depends upon tip radius R on the order of \sqrt{R} . In order to increase the lateral resolution, it is possible to perform in situ sharpening of the tip by gently touching the surface or by applying high fields (on the order

of 10^8 V/cm) for an appropriate period of time. Besides the tip radius, lateral resolution is affected by the atomic structure of the tip apex. The ideal condition is to have a single atom, or at least a very small group of atoms, protruding from the apex of the tip. In that case the actual tip radius would be much smaller than the nominal radius of the curvature.

The STM can be operated in two different modes to obtain the topography of the scanned surface: the *constant current mode* or the *constant height mode* (Fig.1.2). In the constant current mode the tunneling current is kept constant by the feedback system, which changes the height z of the tip. The displacement of the tip, given by the voltage applied to the piezoelectric drive $z = f(x,y)$, yields to a topographic map of the surface.

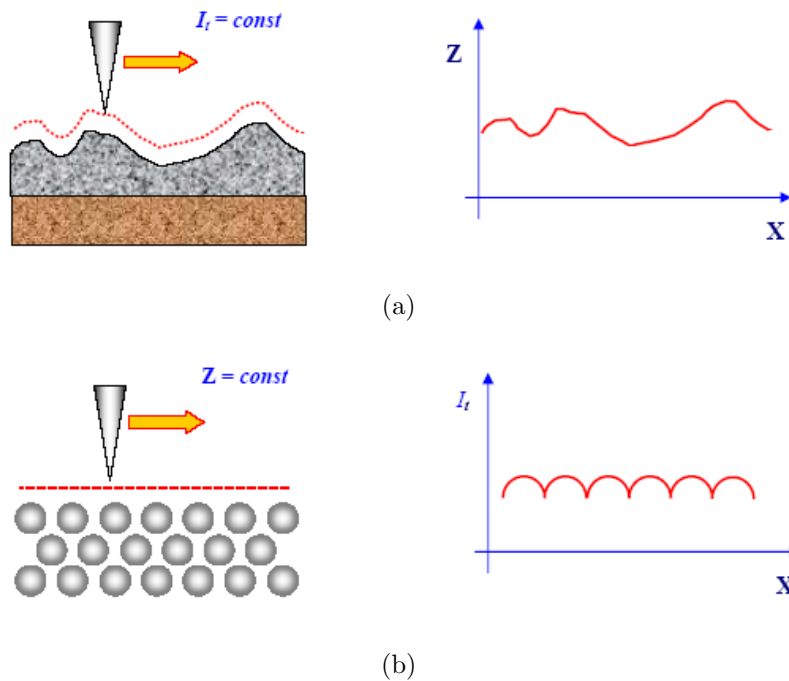


Figure 1.2: STM operation modes: (a) constant current mode; (b) constant height mode

Alternatively, in the height constant mode, the metal tip is moved across the surface at a distance of a few angstroms, which is kept nearly constant, and at a

constant voltage. The current signal $I = f(x,y)$ is monitored and then showed as a STM image. Operating in this mode, the scan of the surface can be held with no feedback, or either with such high velocity that the feedback network can follow just partially the topographic modulations. It is then possible to use very high scan velocities, observing the surfaces changes in about real time. The constant height mode is practical for very flat surfaces; the current mode, on the other hand, is generally used for atomic-scale images.

It should be noted that if different atomic species are present in a sample, they may produce different tunneling currents for a given bias voltage. Thus the height data may not be a direct representation of the topography of the surface of the investigated sample [69].

1.2 Atomic Force Microscopy

Like the STM, the AFM relies on a scanning technique to produce very high resolution, 3D images of sample surfaces. The differences between the STM and the AFM are mainly two:

1. in the AFM the tip and the sample are in direct contact, so the nature of their interaction is more complicated than the one that occurs in the STM;
2. in the AFM instrument a cantilever deflection detector is needed. This makes the apparatus more complex.

The AFM has been invented by Binnig, Quate and Herber in 1986, and it measures the ultra small (less than 1 nN) interaction forces between the tip and the sample. Those forces are quantified by measuring the motion of a very flexible cantilever beam with an ultra small mass constituting the probe. The force applied to the tip by the scanned surface flexes the cantilever. By monitoring that flexure

it is possible to evaluate the force presents between the AFM tip and the sample surface (Fig.1.3).

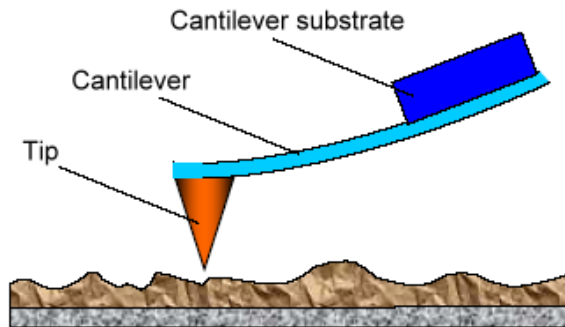


Figure 1.3: Principle of operation of the AFM

The AFM topography is obtained from the cantilever deflection. That signal has been collected using different techniques during the years: tunneling current detection similar to that used in the STM; capacitance detection; piezoresistive detection; and four different optical techniques, optical interferometry using optical fibers, optical polarization detection, laser diode feedback and laser beam deflection. The optical detection techniques are believed to be the more sensitive, reliable and easily implemented methods than the others. Between those four techniques, the optical beam deflection method is the more common in commercial AFMs due to its large working distance, its insensitiveness to distance changes and its capability of measuring angular changes, which allows an estimation of friction forces. This deflection detection system is based on the optical lever principle. The light from a laser diode is focused on the free edge of the cantilever and reflected to a photodiode. The detector is segmented into four closely spaced devices, and initially the light ray is set to hit the photodiode in the middle of the four subdiodes. Any deflection of the cantilever will cause an imbalance of the number of photons reaching each sector of the detector. Hence, the electrical currents on the photodiodes will be unbalanced

too. Labeling $I_{01}, I_{02}, I_{03}, I_{04}$ the current intensities when the cantilever is not scanning the surface, and I_1, I_2, I_3, I_4 the corresponding values when the cantilever is deflected by the interactive forces between the tip and the sample surface, it is possible to quantify the intensity and the direction of the cantilever deflection by the difference of each pair of values: $\Delta I_i = I_i - I_{0i}$ (Fig.1.4). This optical cantilever

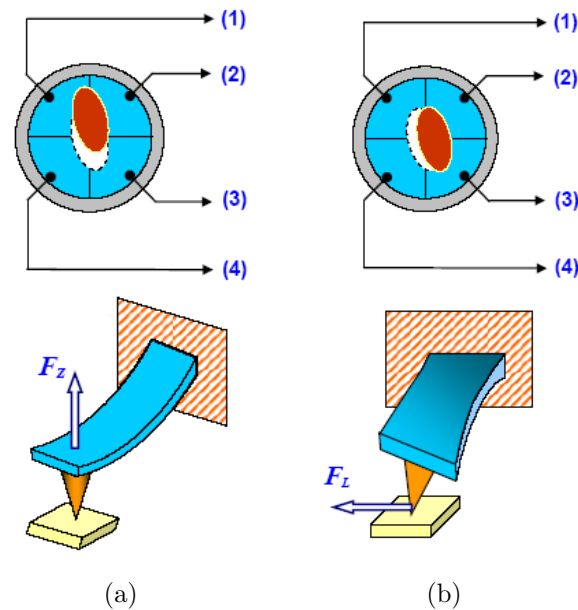


Figure 1.4: (a) Normal forces bend the tip, therefore the reflected beam moves vertically; (b) the cantilever is twisted by lateral forces, consequentially the reflected laser beam moves horizontally on the photodetector

deflection system allows to detect normal and lateral force signals simultaneously. When the tip is subjected to attractive or repulsive forces from the surface, the reflected laser beam moves vertically on the detector. If lateral forces occur, the cantilever is twisted and the reflected beam will be deflected perpendicular to the ordinary deflection direction, as shown in Fig.1.4.

The AFM operates in both *constant height* and *constant force* modes. In the force mode the normal force applied is kept constant, so the feedback circuit is used to modulate the voltage applied to the piezoelectrical scanner holding the sample, in

order to adjust the PZT height. In this way, the cantilever vertical deflection, given by the current intensity difference between the top and the bottom detector, will remain constant during the scanning. The change in the piezo height is collected by the system and it is used as a direct measure of the surface roughness of the sample. When the feedback gains are low, the piezo remains at an almost constant height and the cantilever deflection data are stored in a matrix, which constitute the AFM topographic images of the sample.

Besides constant force and constant height mode, the AFM can be operated in contact mode, non-contact mode and intermittent contact (tapping) mode [70].

1.2.1 Contact Mode

In contact mode, the tip makes soft physical contact with the sample. Since the tip-surface distance is very small, repulsive van der Waals forces are dominant and the cantilever is consequently deflected to accommodate the changes in topography. This deflection is due to the feature of the cantilever to bend under the effect of applied forces, which lets it to be modeled as a spring. The deflection signal is monitored during the scanning in order to generate the feedback signal which makes the piezoelectric stage moving the sample to maintain a constant deflection/force, according to the mode in use. It is a static measurement, so the contact mode it is often referred as static AFM. The position of the stage is used to generate the topographical image. The contact mode is generally used to image flat samples that can withstand lateral forces during scanning. In addition, scanning rough samples may cause the tip breakage before the feedback system can respond, when it approaches large surface features.

The forces experienced by the cantilever as it approaches from several microns above the surface can give information about long-range interactions, such as electrostatic effects (Fig.1.5). As the cantilever comes closer to the surface, shorter

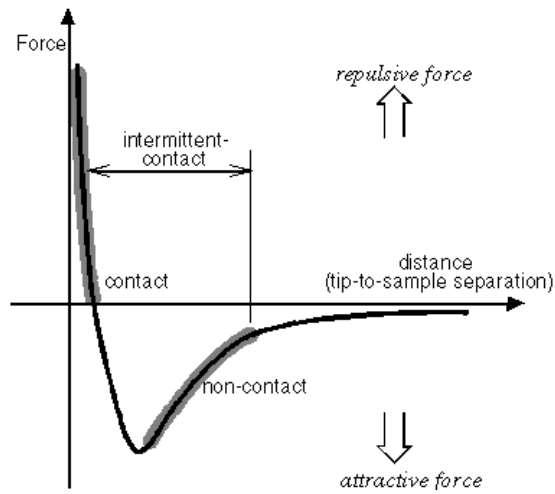


Figure 1.5: Interatomic force vs. distance curve

range forces, like capillary or van der Waals forces, can be measured (Fig.1.6). Once the tip approaches the sample, the cantilever may be pushed into the surface with some force. In that case it is possible to investigate the viscoelastic properties of the sample, to obtain Young's modulus, stiffness for different strain rates or maximum applied force. Pulling the tip away from the surface allows to measure adhesive forces [71, 12, 55].

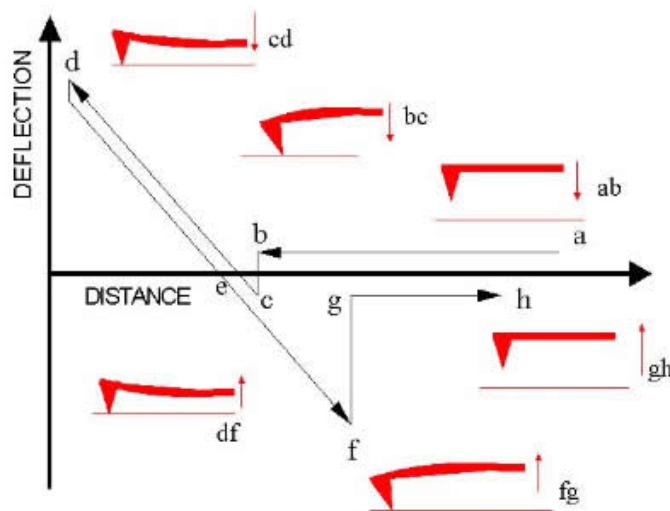


Figure 1.6: Typical force-distance curve for a tip in contact mode

Force Plots

In order to study the interactions between the tip and the surface above mentioned, it is necessary to use the force calibration mode. In this mode the x and y voltages applied to the piezo are held to zero, and a sawtooth voltage is applied to the z electrode of the piezo tube. As the cantilever approaches the surface, initially the forces are too small to give a measurable deflection of the cantilever, so it remains in its undisturbed position. By changing the applied voltage, the sample can be moved up and down relative to the stationary cantilever tip. As the piezo moves the sample up and down, the cantilever deflection signal is monitored. The plot of the cantilever tip deflection signal versus the voltage applied to the piezo tube gives the force plot showed in Fig.1.6. The flat portion of the curve indicates the initial approach of the cantilever to the sample. As the tip approaches the surfaces to within a few nanometers (point b), the attractive van der Waals and capillary forces overcome the cantilever spring constant and the tip jumps in contact with the surface. The tip is pulled toward the surface and contact occurs at point c in the graph. From this point on, the tip is in contact with the sample and the cantilever gets deflected as the piezo extends further (portion cd of the force curve). As the piezo retracts, the tip moves beyond the zero deflection line due to the attractive forces, into the adhesive regime, deflecting downwards. At point f in the graph, the tip breaks free of the adhesive forces and it is again in free air. The horizontal distance between point c and point g along the retracing line represents the distance moves by the tip in the adhesive regime. According to Hooke's law, the adhesion force is obtained by multiplying that distance by the cantilever spring constant [72].

The main disadvantage of the contact mode is related to the fact that the tip is in direct contact with the sample. This may cause the breakage of the tip or, for soft samples, the damage of the surface. Therefore a non-contact mode is more suitable for soft sample analysis.

1.2.2 Tapping Mode

Operating the AFM in tapping mode, the position of the cantilever is slowly moved toward the sample as it is vibrated close to its resonance frequency. In this way the tip is not in constant contact with the surface, therefore the risk of damaging either the tip or the surface is reduced. Once the tip starts tapping the surface, under the influence of the interactive forces between the probe and the sample, the phase of the resonant frequency of the cantilever will shift and its amplitude will decrease [73]. Monitoring these changes it is possible to obtain topographic maps of the scanned surface. The setpoint prescribed by the operator is the ratio between the tapping mode amplitude over the amplitude of the freely vibrating cantilever. This ratio is maintained during the scan by the electrical feedback system of the AFM.

Modeling the AFM as a coupling of two springs, where the cantilever is represented by the spring with stiffness k , the second spring, with spring constant k_{ts} , represents the force interaction between the tip and the surface. The stiffness of the interaction spring is given by the derivative of the force gradient of the force with respect to the tip-sample distance F_{ts} . Therefore, the AFM is characterized by a spring constant given by:

$$k_{tot} = k + k_{ts} = k - \frac{\partial F_{ts}}{\partial z} \quad (1.5)$$

According to the simple harmonic oscillator, the resonant frequency ω is shifted by $\Delta\omega$ from the free resonant frequency ω_0 due to the force interaction:

$$\omega^2 = (\omega_0 + \Delta\omega)^2 = \frac{k + \frac{\partial F_{ts}}{\partial z}}{m^*} \quad (1.6)$$

where m^* is the effective mass of the cantilever.

Since $\Delta\omega$ is much smaller than ω_0 , it is possible to write the approximated

relation:

$$\frac{\Delta\omega}{\omega_0} \cong -\frac{1}{2k} \frac{\partial F_{ts}}{\partial z} \quad (1.7)$$

Eq.1.7 shows the proportional relation between the frequency shift and the force gradient of the tip-sample interaction.

According to the simplified model above presented, the dynamic force microscopy is based on the dependence of the oscillation frequency on the force gradient, while static AFM measures the force itself.

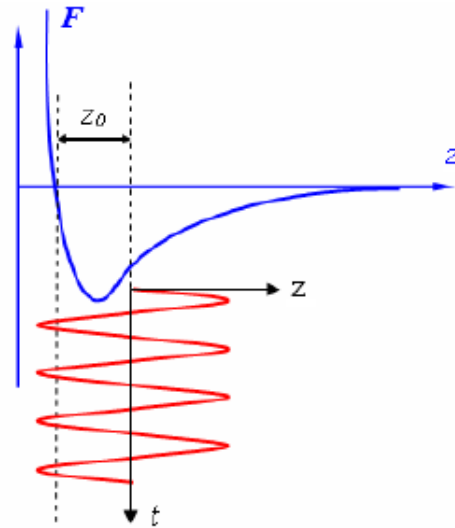


Figure 1.7: Simplified diagram of the oscillation in Tapping Mode: the red curve represents the oscillation trajectory; the blue trace is the force-distance curve

In tapping mode, or amplitude-modulation (AM) AFM, the cantilever is excited externally at a constant frequency close to its resonance frequency ω_0 . The amplitude of one oscillation cycle ranges from 10 to 100 nm, and the tip interacts with the surface during the lower semioscillation of the cycle (Fig.1.7). During one full cycle, the tip-sample interaction ranges over attractive and repulsive forces. Therefore the measured force is a convolution of the force-distance curve with the oscillation

trajectory. At the same time, the resonant frequency of the cantilever changes due to the appearing force gradient, according to Eq.1.7.

At large distances, the forces between the tip and the sample are negligible, so the cantilever oscillates with its free oscillation amplitude. Upon approach of the probe toward the surface, the amplitude gets smaller with continuously decreased tip-sample distance, due to the interaction forces. The decrease of the oscillation amplitude can be explained by the force-distance curve reaching the repulsive part, which hinders the tip from indenting further into the sample.

The TM imaging is based on monitoring the voltage of the z electrode of the piezo. The cantilever is oscillated at a frequency ω close to its resonant frequency ω_0 , with amplitude u_0 . During the scanning, the feedback system moves the piezo in order to maintain the vibrational amplitude constant at the value A imposed by the user. The voltage supplied to the z electrode of the piezo is stored as topographical data of the surface.

Amplitude Diagrams

The piezo excites the cantilever with an harmonic load:

$$u = u_0 \cos(\omega_0 t) \quad (1.8)$$

The cantilever trajectory can be analyzed solving the differential equation of the motion:

$$m^* \ddot{z} = -k(z - u) - \gamma \dot{z} + F_0 \quad (1.9)$$

where $\gamma \dot{z}$ represents the viscous force, and F_0 represents the constant forces may affect the tip. At the equilibrium position, F_0 is given by Hooke's law. It has to be noted that the z -position of the probe is not equivalent to the real tip-sample distance at equilibrium position, since the cantilever might bend statically due to

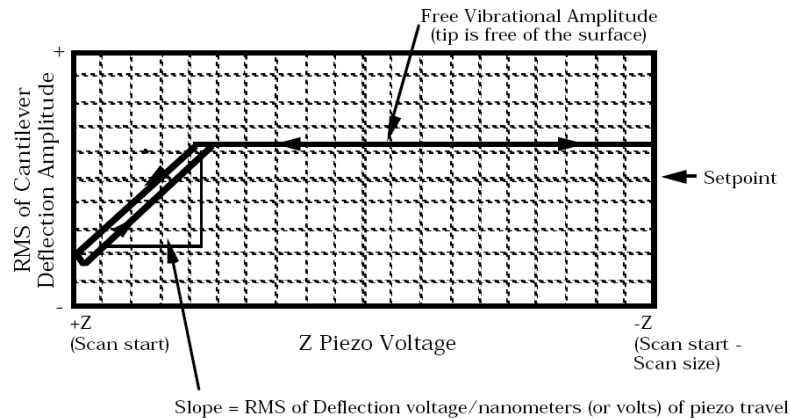


Figure 1.8: Typical amplitude vs. z position plot for TM AFM

the interaction forces. When the cantilever is oscillated at its resonant frequency, the typical amplitude diagram has the shape represented in Fig.1.8. The right side of the plot reflects the free vibration amplitude of the cantilever: the distance between the tip and the sample is not close enough to influence the vibration amplitude. As the piezo brings the cantilever closer to the sample, the amplitude decreases when the probe contacts the surface. During the time the cantilever is in contact with the surface, for each nanometer of the cantilever position decreases by two nanometers the amplitude of the oscillation. At the point of the vibration cycle when the piezo begins to retract the sample, the vibrational amplitude of the cantilever begins to increase. It will increase until the tip is again free of the surface, then it levels off at the free standing amplitude [74].

1.3 AFM Probes

For an AFM study, various probes can be used. However, for all probes, the cantilever has to have some characteristics:

- *low normal spring constant*: in order to have a cantilever deflection under a nanoNewton force, the normal stiffness has to be on the range of 10^{-2} to 10^2

N/m to go down to atomic resolution in contact mode;

- *high resonance frequency*: its value influences the imaging rate. To achieve a large image bandwidth the AFM cantilever should have a resonance frequency value above 10 kHz;
- *a sharp protruding tip*: the tip radius has to be chosen according to the corrugations in the sample. It has to be much smaller than the radii of the surface features in order to image accurately;
- *high lateral spring constant*: its high value reduces the effect of lateral forces and it is strongly related to the tip length. For friction measurements, it is preferred a cantilever with low lateral spring constant;
- *short cantilever length*;
- *optical properties for deflection sensing* (i.e. incorporating a mirror);

Low spring constants and high resonance frequencies are obtained by reducing the cantilever mass. Small size and low mass can be achieved by conventional microfabrication techniques, which allow to obtain planar thin-film structures with submicron lateral dimensions. Triangular V-shaped cantilevers have higher lateral spring constants than rectangular cantilevers. Tips can reach near-atomic dimensions thanks to microscopic asperities on the 50 nm corner radius obtainable by photolithography.

Cantilevers are available in many different materials. The most common are silicon nitride (Si_3N_4), silicon or diamond. Important parameters are Young's modulus and material density, because they determine the resonant frequency aside from the geometry, and hardness, as an indicator for the cantilever's durability. Between the range of materials that can be used to make cantilevers, silicon nitride is the cheapest one. Si_3N_4 cantilevers are very asperous, and well suited for imaging in almost

any kind of environment, especially with organic and biologic materials. The most common ones are microfabricated triangular silicon nitride beams with integrated square pyramidal tips made with the plasma-enhanced chemical vapor deposition (PECVD) technique. Four cantilevers are located on a single substrate made of boron silicate glass (Pyrex). They are characterized by different sizes and spring constants, but all have the same thickness of $0.6 \mu\text{m}$. The most commonly used cantilever beam has a $115 \mu\text{m}$ nominal length and wide leg with a vertical spring constant of 0.58 N/m . To analyze soft samples cantilevers with smaller spring constant are more suitable. The pyramidal tip on the free edge is highly symmetric and has a radius in the range of 20 and 50 nm. Its side wall angle is 30° and the lengths of the edges of the tip at the cantilever base are about $4 \mu\text{m}$ long. Si_3N_4 commercial cantilevers typically have a width:length ratio of 10 over 30, which results in spring constants from 100 to 1000 time stiffer in lateral direction than in normal direction. Thus, those cantilevers are not well suited for torsion, hence their use is not recommended for friction measurements, where sensitiveness to later force is needed.

Other widely used cantilevers are made of single-crystal silicon with integrated tips. Those tips are sharper than the Si_3N_4 tips because they are formed directly by anisotropic etching a single-crystal of Si, rather than grown by deposited material. Tip radii $< 10 \text{ nm}$ are commercially available on rectangular cantilevers with square pyramidal tips. Rectangular cantilever have smaller torsional spring constant, compared to the V-shaped cantilevers, because of their lower thickness, larger tip and longer cantilevers. Typically, lateral spring constants are about two order of magnitude larger than normal spring constants (Fig.1.9).

In order to conduct tribology tests, such as scratching, indentating and wearing, diamond tips are used. Typically, those tips are made of one single crystal natural diamond shaped into a three-sided pyramid with an apex angle of either 60° or 80°

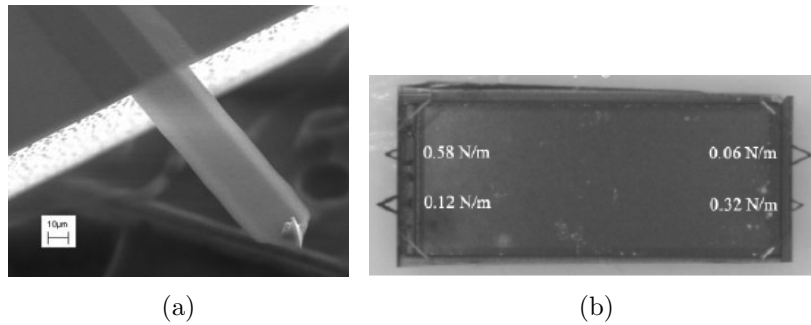


Figure 1.9: (a) Typical rectangular Si AFM cantilever; (b) Si₃N₄ cantilever substrate with the cantilevers spring constants. On the left side there are the narrow legged cantilevers; on the right side the wide-legged ones

and an apex radius of about 100 nm. The tip is bonded to a gold-plated stainless steel spring sheet, the cantilever, using a conductive epoxy. In order to have a range of beam stiffness to choose from, diamond tips are produced with different free edge lengths.

Carbon nanotube probes

For those applications requiring high-resolution imaging of trenches, carbon nanotube tips are used, thanks to the small diameters of the nanotube attached to the tip, and high aspect ratios. They can be made of single walled carbon nanotubes (SWNT), which are microscopic graphitic cylinders with 0.7-3 nm diameters and lengths up to a few micrometers, or multi walled carbon nanotubes (MWNT), obtained by nested, concentrically arranged SWNT, which reach diameters in the 3-50 nm range [75]. The high resolution is achieved by the small diameter of the CNT tips, while the length allows imaging of rough surfaces with steep and deep features. Furthermore, CNT tips are very robust because of their strength and elastically buckling ability. Carbon nanotubes, whose growing methods are described in 3.1, can be attached on a scanning probe by different approaches. The first technique developed by Dai et al., uses a polymeric adhesive to attach a bundle of MWNTs

to the tip of a commercial silicon probe. Hafner et al. developed a method to grow a SWNT directly onto the tip of a silicon probe by chemical vapor deposition (CVD) using ethylene gas as feedstock. Nakayama et al. used electrostatic attraction, welding and carbon deposition to produce CNT tips [40]. The simplest technique to fabricate MWNT probe has been developed by Stevens et al. A low-density, vertically aligned forest of MWNTs is prepared by CVD, and then a single MWNT is transferred to a silicon cantilever by applying a DC electric field between the cantilever and the MWNTs cartridge source. The length of the MWNTs ranges from less than 1 to 10 μm [15].

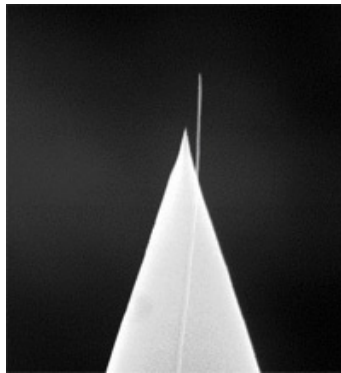


Figure 1.10: SEM image of a MWNT AFM tip

Tips often require a shortening process by an *in situ* AFM manipulation. This technique uses a high potential (>7 V) and it is run in an AFM operating in tapping mode, setting the amplitude voltage at 1 V, the Z distance at 1000 nm and the scan rate at 1 Hz. The sample used is an electrode substrate of a 20 nm ion-beam-sputtered Ir film on a low resistive (<0.001 Ωcm) Si chip. The contact between the tip and the sample is manually adjusted in the force-distance plots in order to guarantee a soft contact. By applying a 1-2 s pulse of 2-3 V DC field to the negatively biased CNT tip as it intermittently makes contact with the metal surface, the diameter of the MWNT is reduced [16].

Chapter Two

Friction and wear on the atomic scale

With the appearance of tip-based microscopes and computational techniques for simulating tip-surface interactions and interfacial properties, the fields of microtribology, nanotribology, molecular tribology or atomic-scale tribology has developed. This area is concerned with experimental and theoretical investigation of processes based on different scales. In macrotribology, the tests are conducted on components with relatively large mass under heavy loading conditions. On the other hand, micro and nanotribology tests are carried out under light loading conditions where at least one of the mating component has a relatively small mass. In this situation, negligible wear occurs and the surface properties dominate the tribological performance.

2.1 Friction Force Microscopy (FFM)

The FFM, also called lateral force microscope, is used to quantify the dissipative processes on an atomic scale by observing the interactions between the surface scanned and a sharp tip sliding on it. The first FFM was produced in 1987 by Mate in order to study friction on the atomic scale. He used a tungsten wire as a tip, and applied different techniques to detect the lateral forces.

The general principle of the FFM is to create a relative motion between the tip, held by a cantilever, and the surface. That motion is made by a scanner, constituted by piezoelectric elements, which moves either the sample or the tip, perpendicularly along the surface with a certain periodicity. By setting the scanner, it is possible to choose the normal force F_N applied to the cantilever, and consequentially to the surface. Such force induces the deflection of the cantilever. If during the scan the normal force increases because the tip is facing a local surface slope, the scanner is retracted by a feedback loop. On the other hand, if F_N decreases, the scanner is extended to bring the tip closer to the surface. Monitoring the vertical position of the scanner allows the determination of the surface topography line by line. There are different ways to achieve that goal, one of those is the laser beam deviation mode introduced by Marty and Meyer. A light beam is focused on the free edge of the cantilever, and it is reflected to a photodetector. When the cantilever moves, the reflected beam moves as well, causing a variation of the photocurrent in the detector, corresponding to a variation of the normal force applied to the surface.

The laser beam deflection is not the only way to measure the forces between the tip and the surface: it can also be used a capacitance detection method, a dual fiber interferometry technique, or piezolevers. In the capacitance detection, two plates are positioned close to the cantilever, so the capacitance variation can be measured during the scan; the second technique uses two optical fibers to detect the cantilever deflection along the two orthogonal directions inclined with a 45° with

respect to the surface normal. If the detection mode is based on the piezolevers, cantilevers connected to two Wheatstone bridges measure the normal force, which is proportional to the sum of the bridges signals, and the lateral force, proportional to the difference of the two signals.

It has to be noted that sliding the tip over the sample surfaces causes a lateral force F_L due to friction. The direction of such force is opposite to the scanning velocity direction, so it hinders the motion of the tip. Because of this force, the cantilever is subjected to a torsion: by detecting also the lateral movement of the lever, it is possible to get a complete topography of the surface. This is possible using the four-quadrants photodetector described in sec.1.2.

2.2 Force calibration

To calibrate the force, one should first check the actual dimensions of the cantilever, using either an optical or an electron microscope, or by determining some of them from the resonance frequency of the cantilever itself. For rectangular cantilevers, once the actual dimensions (width w , length l , thickness t , tip height h) are known, it is necessary to measure the photodetector sensitivity S_z (nm/V). For hard surfaces (e.g. Al_2O_3), the S_z is the slope of the measured force vs. distance curves. In that case, elastic deformations are negligible and the vertical movement of the scanner corresponds to the cantilever deflection.

Typically, when the tip is brought close to the surface, no vertical signal V_N from the four-quadrant photodetector is registered until the tip reaches the surface. Further extension or retraction of the scanner results in an elastic behavior until the tip jumps again out of contact. The slope of the elastic part of the curve gives the sensitivity S_z . Assuming that the beam is focused on the free edge of the cantilever, right above the probing tip, the normal force F_N and the lateral force F_L are related

to the voltages V_N and V_L , respectively, according to the following relations:

$$F_N = c_N S_z V_N \quad (2.1)$$

$$F_L = \frac{3}{2} c_L \frac{h}{l} S_z V_L \quad (2.2)$$

where:

- $c_N = \frac{Ewt^3}{4l^3}$ is the normal constant spring;
- $c_L = \frac{Gwt^3}{3h^2l}$ is the lateral constant spring.

If cantilevers with different shapes are used, it is necessary to perform a finite element analysis, although in few cases analytical formulas can be derived. For some application, it may also be important to define the radius of curvature R of the tip.

2.2.1 Friction force measurement techniques

For macrofriction analysis it is possible to obtain a direct measurement of the normal force N and the friction force F_L separately, hence the coefficient of friction μ can be easily evaluated by the relation: $\mu = F_L/N$. The evaluation of the micro/nanofriction force is more complicated because the relation between the lateral deflection response of the AFM photodetector and the corresponding tilt angle of the AFM cantilever is to be identified in the process of measurement. The most challenging task is the determination of the actual torsional stiffness of the cantilever, since it is affected by various uncertainties, such as thickness, material properties and coatings. There are many different calibration methods to measure atomic-scale friction. Ruan and Bhushan [61] proposed two methods of lateral force calibration.

The Ruan and Bhushan lateral force calibration method

Defining the scanning angle as the angle relative to the long axis of the cantilever, the y -axis, a zero degree scanning angle corresponds to the sample scanning in the

y direction, and a 90 degree scanning angle corresponds to the sample scanning in the x axis perpendicularly to the y axis on the xy plane.

Method I: Height mode with parallel scans

Operating the AFM in height mode (sec.1.2) and scanning the sample in the y direction, it is possible obtain the topographical image of the surface and to measure the friction force. Theoretically, if there were no friction between the tip and the sample, the only factor causing the cantilever to deflect vertically would be a topographic feature. But friction occurs on all contact surfaces when two objects are relatively moving, so the friction force appearing between the tip and the sample also contributes to the cantilever deflection. Calling W_0 the normal force between the tip and the sample when the sample is stationary, and W_f the friction force generated during the scan of the tip against the sample, the direction of the friction force is reversed as the scanning direction is reversed:

$$\vec{W}_{f(y)} = -\vec{W}_{f(-y)} \quad (2.3)$$

When operating in height mode, the vertical cantilever deflection is kept constant, and this is done by maintaining the total force, given by the normal and the friction forces, applied to the tip constant. Since the friction force works against the tip motion, its direction changes as the traveling direction of the sample is reversed: in order to keep the deflection of the cantilever constant, it is then necessary to adjust the normal force accordingly to the sample traveling direction. Taking as reference point the point where the cantilever joints the substrate, the difference of the normal forces between the two traveling directions at a given friction force can be calculated as follow:

$$(W_0 - \Delta W_1)L + W_f l = (W_0 + \Delta W_2)L - W_f l \quad (2.4)$$

where:

- ΔW_1 and ΔW_2 are the absolute values of the changes of the normal force when the sample is scanning in $-y$ and y directions, respectively;
- L is the length of the cantilever;
- l is the vertical distance between the end of the tip and the joint point where the cantilever is attached to its substrate.

The friction force is evaluated by Eq.2.4:

$$W_f = \frac{(\Delta W_1 + \Delta W_2)L}{2l} \quad (2.5)$$

and can be used to calculate the coefficient of friction μ :

$$\mu = \frac{W_f}{W_0} = \frac{(\Delta W_1 + \Delta W_2)L}{W_0 2l} \quad (2.6)$$

It has to be noted that other attractive forces, such as adhesive and interatomic forces, between the tip and the substrate occur in all circumstances. If these forces can be neglected, the normal force is given by the product of the initial cantilever deflection h_0 times the spring constant of the cantilever. The quantity $(\Delta W_1 + \Delta W_2)$ can be measured by multiplying the same spring constant by the height difference of the PZT between the two traveling directions of the sample. Thus, Eq.2.6 can be rewritten as:

$$\mu = \frac{W_f}{W_0} = \frac{(\Delta h_1 + \Delta h_2)L}{h_0 2l} \quad (2.7)$$

If the adhesive forces between the tip and the sample are too large to be neglected, they need to be taken into account in the calculation of the normal force.

In order to minimize the uncertainty in determining the normal force, Ruan and Bhushan proposed to make the measurements at different normal loads and to use $\Delta(h_0)$ and $\Delta(\Delta h_1 + \Delta h_2)$ from the measurements in Eq.2.7. It has to be noted that Eq.2.6 and Eq.2.7 are derived under the assumption that the friction

force W_f is the same for the two scanning directions. This is an approximation, but the difference between the normal forces in the two directions is much smaller than W_0 that it is reasonable to ignore the second-order correction.

Method II: Aux mode with perpendicular scan

Another method to evaluate friction force is suggested by Meyer and Amer. Force is related to the change of the light intensity from the two horizontal quadrants of the photodetector as the sample is scanned perpendicularly to its long axis. With this settings, the cantilever is twisted by the action of friction during the scanning of the surface, therefore the reflected beam will have a different intensity between the two horizontal detectors. The differential signal between the left and the right detectors is denoted as FFM signal and it is defined as $FFM = \frac{L-R}{L+R}$. The magnitude of the friction force can be evaluated by the degree of the cantilever twist, which is related to the FFM signal.

As pointed out by Ruan and Bhushan, the friction force may not be the only factor contributing to the FFM signal. Many other variables can interfere, from the simple engagement of the tip to the surface, to the misalignment of the detectors with respect to the reflected laser beam. Focusing on the alignment of the laser beam on the photodetector, it has to be noted that the differential friction signal detected changes as the normal force applied to the probe changes, even if the tip is not experiencing any friction. This component of the signal, referred to as FFM_F , is not related to the actual friction force, whose signal component is called FFM_T , or the cantilever deflection, thus it has to be removed from the signal. In order to do that, the sample can be scanned in both positive and negative directions along the x -axis, while recording the FFM signal. Based on the reversing direction of the friction force as the scanning direction reverses, the part of the signal due to

misalignment can be removed by subtracting the two recorded signal:

$$FFM(x) - FFM(-x) = FFM_T(x) - FFM_T(-x) = 2FFM_T(x) \quad (2.8)$$

It is also possible to evaluate the FFM_F component of the monitored signal by averaging the signals recorded in each direction, obtaining:

$$FFM(x) + FFM(-x) = 2FFM_F \quad (2.9)$$

By subtracting this value from the FFM signal, the actual friction signal FFM_T is obtained.

Observations about the calibration methods

Method I, the *height mode*, is very easy to use, and, technically, provides 3D friction profiles and the corresponding topographical map of the surface. However, there are some problems. Under most circumstances, the PZT scanner is affected by hysteresis when the scanning is run in both positive and negative directions along the y -axis. Therefore the measured topographic profiles will be shifted relative to each other along the scanning axis. However, it is still possible to measure the average height difference between the two scans in order to be able to evaluate the average friction.

Method II is a more accurate approach since the subtraction of the FFM_F signal from FFM does not introduce errors to local friction data. The ideal approach for this method would be to add the average value of the two profiles to get the error component of the signal, FFM_F . Thus, subtracting that component from either profiles would allow to get real friction maps in each direction of the scan. It is also possible to map any directionality and local variation of friction by recording the FFM signal at different loads and then by averaging the coefficient of friction value.

In order to obtain the absolute values of normal and friction forces in Newtons, it is necessary to have an accurate value of the cantilever spring constant k_c . Once such

value is obtained, the normal force applied to the cantilever is given by multiplying the cantilever deflection by its stiffness, for those samples whose adhesion force is very small. In the cases where the adhesion force is large, it should be added to the normal force calculation. The magnitude of the friction force is determined by multiplying the coefficient of friction by the normal load.

The *wedge method*

The Ruan and Bhushan calibration force method based on the optical beam deflection has numerous advantages. The sensitivity and the signal/noise ratio are good, and changing the cantilever is relatively simple. The main drawback is the strong dependence of both the absolute and the ratio value of the normal and friction forces on the precise alignment of the laser beam with the respect to the cantilever. Since the angular deflection of the commercial cantilever caused by lateral forces can be one or two orders of magnitude lower than the vertical deflection, small misalignments can lead to significant errors in lateral force measurements due to the cross-talk between the normal and the lateral deflections. In order to avoid such error, by experimentally measuring the combined response of the lateral force transducer and the deflection sensor, Ogletree et al. [76] developed the so called *wedge method* of force calibration.

This approach is based on lateral and normal force signals measurements on a sloped surface. In this situation, the lateral force has a geometrical contribution from the product of the applied load and the tangent of the slope. The proposed experimental force calibration is made by sliding the tip across a surface of known slope and measuring the lateral force signal as a function of the applied load. Theoretically this could be carried out on any kind of surface that is tilted with respect to the lateral scanning direction. Practically this is not possible because there would be some uncertainty in the tilt angle, the cantilever chip side may touch the sample

surface during the scan, and this method requires to scan two different tilted surfaces. Thus, this force calibration can be carried out only using a particular sample, which Ogletree suggested to be the faceted $\text{SrTiO}_3(305)$ proposed by Sheiko et al. as a tool to measure the tip sharpness.

While scanning a sloped surface, the tip applies to the surface two forces: the vertical load N and the horizontal tractive force T . Those forces must be balanced by a reaction force from the surface, which can be divided into the two components: the normal load F_N and the friction force F_L . At a given load, tractive, friction and normal forces depend on the direction of motion. For the uphill motion:

$$F_N = N \cos \theta + T \sin \theta \quad F_L = T \cos \theta - N \sin \theta \quad (2.10)$$

By measuring the voltage from the FFM ($F_{L,0}$), this signal can be related to the friction force by the calibration constant α , in N/V. The value of α is a product of all the factors of the experiment: the cantilever lateral force constant, the deflection of the reflected laser beam as function of the lateral probe displacement, and the photodiode angular sensitivity. In order to calibrate the lateral force, it is then needed to find out the functional relation $F_L(N) = \alpha F_{L,0}(N)$. This can be obtained either by empirical fitting the $F_{L,0}$ measurements on a flat surface, or by using a theoretical form from the Hertz or the Johnson-Kendall-Roberts (JKR) theories.

Scanning a flat surface, the friction force can be calculated by taking half the difference between the two directions lateral forces, which corresponds to the half-width of the friction loop $W(N)$. For the tilted sample scanning, the forces are direction-dependent and the offset of the friction loop, $\Delta(N)$, is not zero, and is load-dependent. By calculating the slopes:

$$\Delta' \equiv \frac{d\Delta}{dN} = \alpha \Delta'_0 = \frac{(1 + \mu^2) \sin \theta \cos \theta}{\cos^2 \theta - \mu^2 \sin^2 \theta} \quad (2.11)$$

$$W' \equiv \frac{dW}{dN} = \alpha W'_0 = \frac{\mu}{\cos^2 \theta - \mu^2 \sin^2 \theta} \quad (2.12)$$

it is possible to evaluate the friction coefficient, which is given by the ratio of the two equations:

$$\nu + \frac{1}{\nu} = \frac{2\Delta'_0}{W'_0 \sin^2 \theta} \quad (2.13)$$

Once ν is determined, α can be found by one of either Eq.2.11 or Eq.2.12 by defining Δ' or W' , respectively.

This wedge method is strongly limited to integrated probes with sharp tips, and it can only be performed on specific calibrated gratings. To overcome those limits, Varenberg et al. [77] presented a new calibration method.

The improved *wedge* calibration method

The lateral force calibration method developed by Varenberg requires the use of a calibration grating suitable for both colloidal and integrated probes. Scanning a tilted surface the force applied to the tip by the sample are the contact load N , the adhesion force A and the friction force F_L . These forces are balanced by the normal load L , the lateral force T and the torsion moment M exerted by the cantilever on the tip. All those entities are direction dependent. In equilibrium conditions, assuming small cantilever torsion angle ϕ and referring, for sake of simplicity, just to the uphill motion, the equation for the momentum is:

$$M + L \left[R \sin \theta - \left(h - R + \frac{t}{2} \right) \phi \right] - T \left(R \cos \theta + h - R + \frac{t}{2} \right) \quad (2.14)$$

where:

- h the tip height;
- R is the tip radius of curvature;
- t is the cantilever stiffness;
- the force T is assumed to act through its mid section.

The torsion moment M and the torsion angle ϕ are related by the well-know relation:

$$\phi = \frac{Ml}{GJ} \quad (2.15)$$

where:

- l is the cantilver lenght;
- G is the shear modulus;
- J is the torsion constant of the cross section.

Substituting Eq.2.15 in Eq.2.14 the equilibrium equation assumes the from:

$$MC + LR \sin \theta - T \left(R \cos \theta + h - R + \frac{t}{2} \right) \quad (2.16)$$

where:

$$C = \frac{GJ/l - L(h - R + t/2)}{GJ/l} \quad (2.17)$$

During the scan, the AFM measures the torsion angle ϕ in terms of voltage output M_0 , which gives the value of the torsion moment M by $M = \beta M_0$. The calibration constant β is the equivalent of α in the wedge calibration method, and it is the product of all the factors of the system. It is possible to relate the friction force F_L , applied to the tip during the scanning of a flat surface, to the resulting moment M by combining the equilibrium equation along the axis parallel to the sample surface:

$$T \cos \theta - L \sin \theta - F_L = 0 \quad (2.18)$$

and Eq.2.16, obtaining:

$$F_L^{flat} = T^{flat} = \frac{M^{flat}}{h + t/2} = \alpha M_0^{flat} \quad (2.19)$$

where the calibration constant $\alpha(N/V)$ is given by:

$$\alpha = \frac{\beta}{h + t/2} \quad (2.20)$$

It has to be noted that for an integrated probe $h \gg R$, while for colloidal probes $h = 2R$. Due to reflected beam misalignment with respect to the photodiode, and to crosstalk between deflection and torsion signals, it is impossible to determine the exact zero of the torsion signal and, hence, the actual torsion loop offset Δ_0 . The half-width of the torsion loop is insensitive to this problem since it is a differential value involving a difference from two torsion signals where all absolute errors cancel out. In order to find the zero value of the offset, this method proposes to scan a grating characterized by flat and sloped facets, obtaining the torsion loop offset by subtracting the torsion loop offset measured on the flat surface, Δ^* , to the inaccurate torsion loop Δ_0^* :

$$\Delta_0 = \Delta_0^* - \Delta_0^{flat} \quad (2.21)$$

From the equilibrium equations both for the uphill and downhill motions, along the axis parallel to the scanning surface, it is possible to evaluate the equations that give the value of the lateral force T . Hence, it is possible to calculate the momentum equilibrium equations, which, substituted in the torsion loop half-width W , leads to:

$$\frac{\mu(L + A \cos \theta)}{\cos^2 \theta - \mu^2 \sin^2 \theta} = \frac{W}{h + t/2} = \alpha W_0 \quad (2.22)$$

Following the same procedure, substituting all the known variables in the offset loop definition equation, it is possible to write:

$$\frac{\mu^2 \sin \theta (L \cos \theta + A) + L \sin \theta \cos \theta}{\cos^2 \theta - \mu^2 \sin^2 \theta} = \frac{\Delta}{h + t/2} = \alpha (\Delta_0^* - \Delta_0^{flat}) \quad (2.23)$$

By dividing Eq.2.23 by Eq.2.22, a quadratic equation for μ is obtained:

$$\sin \theta (L \cos \theta + A) \mu^2 - \frac{\Delta_0^* - \Delta_0^{flat}}{W_0} (L + A \cos \theta) \mu + L \sin \theta \cos \theta = 0 \quad (2.24)$$

This equation, for a given applied load L and adhesion force A , provides two possible solutions for the coefficient of friction μ . The only real and acceptable one is the one whose value is smaller than the quantity $(1/\tan \theta)$, in order to avoid a negative calibration factor α . If both solutions satisfy the condition respect to $\tan \theta$, the real value is the one which, once substituted in Eq.2.22 leads to the value of the calibration coefficient α that gives two values for μ , corresponding to the flat ($\theta = 0$) and the sloped surface, close enough to each other.

For colloidal probes, following the procedure above described and substituting $h = 2R$, the equation for the system is:

$$\frac{\mu(L + A \cos \theta)}{\cos^2 \theta - \mu^2 \sin^2 \theta} = \frac{\beta W_0}{R(1 + \cos \theta) + t/2} \quad (2.25)$$

From the offset definition equation, and recalling that $\Delta = \beta(\Delta_0^* - \Delta_0^{flat})$, the following relation is obtained:

$$\frac{\mu^2 \sin \theta (L \cos \theta + A) + L \sin \theta \cos \theta}{\cos^2 \theta - \mu^2 \sin^2 \theta} - \frac{LR \sin \theta}{R(1 + \cos \theta) + t/2} = \frac{\beta(\Delta_0^* - \Delta_0^{flat})}{R(1 + \cos \theta) + t/2} \quad (2.26)$$

Referring to the flat portion of the scanned sample, characterized by $\theta = 0$, the equation:

$$\mu^{flat} = \frac{\beta W_0^{flat}}{(2R + t/2)(L + A)} \quad (2.27)$$

yields to the appropriate constant β , which, substituted in Eq.2.20, gives the calibration coefficient for the friction force detected by colloidal probes.

The improved parallel scan method

In a recent study, Wang et. al [78] proposed an improved parallel scanning calibration, based on Ruan and Bhushan method. As explained above, the Ruan and Bhushan procedure is based on two assumptions:

- *moment-deflection assumption*: the total force moment caused by both friction and normal force is constant relative to the clamped end of the cantilever, when the deflection at the free end of the cantilever maintains at a constant level;
- *constant friction force assumption*: the friction forces for both positive and negative scans have the same value ignoring the variation of normal load applied when the scanning direction is inverted.

Those assumptions are not exactly satisfied in the parallel scan. In the first assumption, even if the deflections at the free end of the cantilever are the same, there may be different combinations of friction and normal forces that make different total force moments, so the deflection might not be at a constant level for both positive and negative scan. This is due to the application of a moment to the end of the cantilever by the friction force, which results in a different distribution of bending moment, and hence to that resulting from a normal force.

During the parallel scan, the direction of the friction force changes accordingly to the scanning direction, and the normal force is consequently adjusted to keep the deflection of the cantilever at a constant level. The constant friction assumption is satisfied only in those situations where the variation of the normal force is not large enough to cause apparent friction variation. Since the normal load changes when the sample motion is reversed, the magnitude of the friction force is different for the positive and the negative directions scans.

When the cantilever is scanning along the direction parallel to its long axis, as explained earlier, there are two forces acting on the tip: the friction force F_L and the normal force F_N . Both can be decomposed into the parallel component, F_P , and the vertical component F_V respect to the long axis. For each direction of scanning, the following relations are valid:

$$F_L \cos \alpha - F_N \sin \alpha = F_P \tag{2.28}$$

$$F_L \sin \alpha + F_N \cos \alpha = F_V \quad (2.29)$$

The bending angles are proportional to the correspondent force components by the compliances, well known from mechanics and related to the cantilever shape, according to the relations:

$$\theta_P = c_{\theta P} F_P \quad \theta_V = c_{\theta V} F_V \quad (2.30)$$

The total bending angle is given by the sum of the two components: $\theta_{tot} = \theta_P + \theta_V$.

When the AFM operates in contact mode in constant deflection mode, the total bending angle remains the same for both scanning directions. Thus, from the equations 2.30, the coefficient of friction can be calculated:

$$\mu = \frac{(F_{N1} - F_{N2}) (L \cos \alpha - 2h \sin \alpha)}{(F_{N1} + F_{N2}) (L \sin \alpha + 2h \cos \alpha)} \quad (2.31)$$

where the subscripts 1 and 2 refer to the positive and the negative scanning directions, respectively. The two terms $(F_{N1} - F_{N2})$ and $(F_{N1} + F_{N2})$ can be related to the piezotube height signal by the spring constant k of the cantilever: $(F_{N1} - F_{N2}) = k(h_1 - h_2)$ and $(F_{N1} + F_{N2}) = k(h_1 + h_2)$. In order to eliminate the influence of the adhesion force, the term $(h_1 - h_2)/(h_1 + h_2)$ is replaced by $\Delta(h_1 - h_2)/\Delta(h_1 + h_2)$ [61]. Eq. 2.31 can be rewritten in the new form:

$$\mu = \frac{\Delta(h_1 - h_2) (L \cos \alpha - 2h \sin \alpha)}{(h_1 + h_2) (L \sin \alpha + 2h \cos \alpha)} \quad (2.32)$$

Substituting the horizontal distance $L \cos \alpha - h \sin \alpha$ and the vertical distance $L \sin \alpha + h \cos \alpha$ into the μ defining equation obtained by Ruan and Bhushan method, the coefficient of friction takes the form:

$$\mu = \frac{\Delta(h_1 - h_2) (L \cos \alpha - h \sin \alpha)}{(h_1 + h_2) (L \sin \alpha + h \cos \alpha)} \quad (2.33)$$

Eq.2.31 and Eq.2.33 lead to two values of coefficient of friction whose difference increases as the h/L ratio increases. The two values will be close when the cantilever length L greatly exceed its tip height h .

2.2.2 The one-dimensional Tomlinson Model

The friction force profile drawn with FFM is characterized by a typical sawtooth pattern. That profile is the direct consequence of the *stick-slip phenomena*, which was first discussed in 1929 by Tomlinson.

According to the Tomlinson model, the tip motion is influenced by the interaction with the atomic lattice of the examined surface and the elastic deformation of the cantilever. The shape of the potential between the tip and the surface, $V(r)$, depends on several factors, such as the chemical composition of the materials involved and the atomic arrangement of the tip apex. For sake of simplicity, it will be considered a sinusoidal profile with the periodicity of the atomic lattice a , and a peak-to-peak amplitude E_0 . It is also possible to introduce a single parameter, the lateral spring constant k_{eff} , to consider both the elasticity of the cantilever and the contact area. If the cantilever moves along x with constant velocity v , the total energy of the system is:

$$E_{tot} = -\frac{E_0}{2} \cos\left(\frac{2\pi x}{a}\right) + \frac{1}{2} k_{eff} (vt - x)^2 \quad (2.34)$$

At the initial instant t_0 , the tip is in a position corresponding to the absolute minimum of the system energy. When the tip starts moving, the energy amount increases until the tip is in an instable position at $t = t^*$.

At a general instant t , the position of the tip can be determined by equating to zero the first derivative of the total energy respect to the spatial variable x :

$$\frac{\partial E_{tot}}{\partial x} = \frac{\pi E_0}{a} \sin\left(\frac{2\pi x}{a}\right) - k_{eff} (vt - x) = 0 \quad (2.35)$$

The critical position x^* , corresponding to the time t^* , can be calculated by equating to zero the second derivative of the energy, obtaining:

$$x^* = \frac{a}{4} \arcsin\left(-\frac{1}{\gamma}\right) \quad (2.36)$$

where $\gamma = \frac{2\pi^2 E_0}{k_{eff} a^2}$ is a coefficient that considers the strength of the interaction between the tip and the surface with the stiffness of the system.

At the instant t^* , because of the lateral force F^* , the tip suddenly jumps to the next minimum of the potential profile. The amount of the force can be evaluated using the following equation:

$$F^* = \frac{k_{eff} a}{2\pi} \sqrt{\gamma^2 - 1} \quad (2.37)$$

According to what mentioned above, the *stick-slip* phenomena can only be observed when $\gamma > 1$, so when the system is not too stiff or the tip-surface interaction is strong enough. Plotting the value of the lateral force vs. the cantilever position x , it is possible to notice the typical sawtooth pattern. By moving the probe first rightward then leftward, the F_L - x curve is characterized by a positive part, the one deriving from the rightward movement, and a negative portion. The area included in that *friction loop* gives the amount of the total energy dissipated in the scanning action.

2.2.3 The Frenkel-Kontorova-Tomlinson Model

So far a one-atom apex tip has been considered, but it possible to generalize the concept considering a few-atoms flat tip. That will lead to the problem of two periodic atomically flat surfaces sliding one on the other. This situation has been analyzed in the Frenkel-Kontorova-Tomlinson model, where the atoms of a surface are considered to be harmonically coupled with their nearest neighbors. The further discussion is limited to quadratic symmetries, with a_1 and a_2 periodicity for the upper and the lower surface, respectively.

Considering the continued fraction of the friction:

$$f = N_0 + \frac{1}{N_1 + \frac{1}{N_2 + \dots}} \quad (2.38)$$

The slowest convergence is obtained when all $N_i = 1$, which corresponds to the golden mean:

$$\bar{f} = \frac{\sqrt{5} - 1}{2} \quad (2.39)$$

Thus, for a 1-D model, Weiss and Elmer found that the friction decreases with decreasing commensurability, and the minimum is reached when:

$$\frac{a_1}{a_2} = \bar{f} \quad (2.40)$$

2.3 Thermal effects on atomic friction

The Tomlinson model gives a good approximation for the mechanical phenomena of the stick-slip, but some differences between the theoretical model and the actually observed behavior can be pointed out. First, the peaks in the sawtooth profile have different heights; second, the mean friction force shows a logarithmical dependence on the scan velocity v .

Considering the energy profile earlier discussed, as first approximation, it is possible to assume that $\gamma \gg 1$. At the given time $t < t^*$, the tip jump is impeded by the energy barrier

$$\Delta E = E(x_{max}, t) - E(x_{min}, t) \quad (2.41)$$

where x_{max} is the position of the first maximum observed, and x_{min} is the actual position of the tip. The amount of the energy barrier decreases with time, or, equivalently, with the friction force F_L . It vanishes once F_L reaches the F^* value. Closer to the critical point, the energy barrier can be approximated with the following equation:

$$\Delta E = \lambda(\tilde{F} - F_L) \quad (2.42)$$

where \tilde{F} is the force value close to the critical value:

$$F^* = \frac{\pi E_0}{a} \quad (2.43)$$

At finite temperature T , the lateral force which induces the tip to jump is actually lower than F^* . The most probable value of F_L at this point can be estimated from the probability p that the tip will not jump. p is time dependent according to the equation:

$$\frac{dp(t)}{dt} = -f_0 \exp\left(-\frac{\Delta E(t)}{k_B T}\right) p(t) \quad (2.44)$$

where f_0 is the resonance frequency of the system. The probability of a reverse jump is neglected since the energy barrier to overcome would be much higher than ΔE . Substituting in Eq.2.44 the time with the corresponding lateral force, it is possible to write:

$$\frac{dp(F_L)}{dF_L} = -f_0 \exp\left(-\frac{\Delta E(t)}{k_B T}\right) \left(\frac{dF_L}{dt}\right)^{-1} \quad (2.45)$$

Substituting

$$\frac{dF_L}{dt} = \frac{dF_L}{dX} \frac{dX}{dt} = k_{eff} v \quad (2.46)$$

and referring to the approximation in Eq.2.41, it is possible to explicitly write the F_L dependence on the scan velocity, by annull the second derivative of the probability p respect to the force, obtaining:

$$F_L(v) = F^* - \frac{k_B T}{\lambda} \ln \frac{v_c}{v} \quad (2.47)$$

where the critical velocity is given by:

$$v_c = \frac{f_0 k_B T}{k_{eff} \lambda} \quad (2.48)$$

In this way it is demonstrated the experimentally observed dependence of the lateral force to the scan velocity. The approximation for the energy barrier, though, does

not hold when the tip jumps in a very close position to the critical position x^* , which occurs at very high velocities. In that situation, the factor $\left(\frac{dF_L}{dt}\right)^{-1}$ is very small, so it can be neglected in Eq.2.45. Thus, p does not change significantly until it reaches the unit value, so when $t \rightarrow t^*$. This means that friction is about constant at high velocities, according to the classical Coulomb's friction law.

Sang et al. noticed that the energy barrier close to the critical point can be well approximated with the following equation:

$$\Delta E = \mu(F^* - F_L)^{3/2} \quad (2.49)$$

This new approximation leads to:

$$\frac{\mu(F^* - F_L)^{3/2}}{k_B T} = \ln \frac{v_c}{v} - \ln \sqrt{1 - \frac{F^*}{F_L}} \quad (2.50)$$

and the critical velocity value now takes the form:

$$v_c = \frac{\pi\sqrt{2} f_0 k_B T}{2 k_{eff} a} \quad (2.51)$$

This is a discriminating parameter: if $v \ll v_c$, the second logarithm in Eq. 2.50 can be neglected, so the new dependence of the lateral force to the scan velocity becomes:

$$F_L = F^* \left(1 - \frac{v_c}{v}\right)^2 \quad (2.52)$$

In this situation, the lateral force F_L leads to the F^* value, as expected.

The value of the critical velocity varies with the materials involved in the relative motion. Gourdon et al. found that at $v_c = 3.5 \mu\text{m/s}$ value discriminates between an increasing friction and a constant friction regime for lipid films on mica. Bennewitz et al., in their studies on copper and sodium chloride, demonstrated the logarithmical dependence of friction to the scan velocity as long as $v < 1\mu\text{m/s}$. According to those and several other studies, it is possible to state that the increase of friction

with increasing scan velocity is related both with the materials involved and the environment in which the measurements are conducted. As a matter of fact, Riedo et al. observed that friction actually decreases with increasing velocity on hydrophilic surfaces, and the rate of such decrease depends on humidity. On partially hydrophilic surfaces the logarithmical dependence can be observed again.

2.4 Geometry effects on atomic friction

Besides the dependence of friction on materials, temperature and scan velocity previously discussed, friction is also related to the actual shape of the contact between the two surfaces in relative motion. On macroscopic scale, the contact between two sliding bodies is studied within continuum mechanics, based on the Hertz theory. That approach is still valid in FFM as long as the contact area extends for a few nanometers. Going down to a few atoms contacts, it is necessary to switch to other approaches, like molecular dynamics.

The lateral force F_L between two sliding surfaces is related to the contact area, A , and to the size, which can actually be a few orders of magnitude smaller than the geometrical apparent contact area. As first approximation, it is possible to assume a linear relation between F_L and A with a proportional shear strength σ coefficient:

$$F_L = \sigma A \quad (2.53)$$

If plastic deformation occurs, the asperities are compressed until the pressure p to which they are subjected reaches a yield value p^* . At that point, the resulting contact area is:

$$A = \frac{F_L}{p^*} \quad (2.54)$$

The corresponding Amontons' law is:

$$F_L = \mu F_N \quad (2.55)$$

where $\mu = \frac{\sigma}{p^*}$ is the coefficient of friction. The same observation can be made for a contact based on many asperities, leading again to the Amontons' law.

Referring to a sphere, characterized by a radius R , pressed on a flat surface, elastic deformation can be studied. In that case, the contact area is:

$$A(F_N) = \pi \left(\frac{R}{K} \right)^{2/3} F_N^{2/3} \quad (2.56)$$

where:

- $K = \frac{3}{4}E^*$
- E^* is the effective Young's Modulus referred to the elastic moduli E_1 and E_2 and the Poisson's moduli, ν_1 and ν_2 of the sphere and the plane, respectively

It is related to such parameters by the equation:

$$\frac{1}{E^*} = \frac{1 - \nu_1^2}{E_1} + \frac{1 - \nu_2^2}{E_2}$$

Linear relation between F_N and F_L in many asperities contacts can be obtained in some particular case.

Considering also adhesive forces between the asperities, other effects can be observed. If the range of action of those forces is smaller than the elastic deformation, the Johnson-Kendall-Roberts relation can be used:

$$A(F_N) = \pi \left(\frac{R}{K} \right)^{2/3} \left(F_N + 3\pi\gamma R + \sqrt{6\pi\gamma R F_N + (3\pi\gamma R)^2} \right)^{2/3} \quad (2.57)$$

where γ is the surface tension between the sphere and the plane. The actual contact corresponding to a null load is finite and the sphere can be taken away just by pulling it with a certain force.

In the opposite case, when the range of action of adhesive forces is larger than the elastic deformation, the relation between contact area and load is simpler:

$$A(F_N) = \pi \left(\frac{R}{K} \right)^{2/3} (F_N - F_{off})^{2/3} \quad (2.58)$$

In Eq.2.58, called Hertz-plus-offset relation, F_{off} is the negative load necessary to interrupt the contact.

2.4.1 The estimation of the contact area

It is not possible to measure directly the contact area using an FFM, but it is possible with other instruments like a surface force apparatus. Thus, it is necessary to adopt an indirect estimation based on contact stiffness measurements. Modeling the contact between the tip and the surface as a series of two springs, the effective constant k_{eff}^2 of the series is given by:

$$\frac{1}{k_{eff}^2} = \frac{1}{k_{contact}^2} + \frac{1}{c_N} \quad (2.59)$$

where:

- c_N is the normal stiffness of the cantilever;
- $k_{contact}^2 = 2aE^*$ is the normal stiffness of the contact, related to the contact area radius a .

Since typical values of k_{eff}^2 are orders of magnitude higher than the c_N values, it is not possible to operatively apply Eq.2.59.

Carpick et al. proposed a different method for such estimation. According to various models, the lateral contact stiffness of the contact between a sphere and a flat surface is:

$$k_{contact}^* = 8aG^* \quad (2.60)$$

where the effective shear stress G^* , in analogy to the effective Young's modulus E^* , is defined as:

$$\frac{1}{G^*} = \frac{2 - \nu_1^2}{G_1} + \frac{2 - \nu_2^2}{G_2}$$

Modeling again the contact between the tip and the surface as a series of two springs, the effective constant of the series is given by:

$$\frac{1}{k_{eff}^*} = \frac{1}{k_{contact}^*} + \frac{1}{k_{tip}^*} + \frac{1}{c_L} \quad (2.61)$$

In that Eq.2.61 the lateral stiffness of the tip is also included, and its value is comparable to the lateral spring constant. Since the effective spring constant can be easily evaluated by the slope of the friction loops, the radius a of the contact area can be obtained from k_{eff}^2 .

2.5 Wear on atomic scale

By imposing a normal force F_N to the tip whose value is higher than the critical value, the surface of the sample would permanently be modified. In some cases, wear is exploited to create patterns with well-defined shape. In wear tests it is important to observe the lateral force behavior while scratching. Multiplying the mean lateral force by the scanned length, the total amount of the dissipated energy can be obtained. Since an FFM image has a pseudo-atomic resolution, lateral force images allow the determination of the number of the atoms which have been removed from the surface. In this way it is possible to estimate that nearly the 70% of the dissipated energy went into wear-less friction. The surface damage increases proportionally with the load increasing, but it is not affected by a change in the scan velocity.

Kopta et al. conducted their experiments on mica, and they assumed that wear is initiated by atomic defects. When those defects accumulate beyond a critical concentration, they grow from a scar. Such process is related to thermal activation. The number of defects n_{def} created in the contact area $A(F_N)$ is given by:

$$n_{def}(F_N) = t_{res} n_0 A(F_N) f_0 \exp\left(-\frac{\Delta E}{k_B T}\right) \quad (2.62)$$

where:

- n_0 is the surface density of atoms;
- t_{res} is the residence time of the tip;

- f_0 is the attempt frequency to overcome the energy barrier ΔE to break a Si-O bond, which depends on the applied load.

A hole nucleates when the defect density reaches the critical value. The friction force during the nucleation of the hole could be estimated by the thermal activation Kopta et al. derived from their experiments:

$$F_L = c(F_N - F_{off})^{2/3} + \gamma F_N^{2/3} \exp(B_0 F_N^{2/3}) \quad (2.63)$$

The first term gives the wear-less dependence of friction in the Hertz-plus-offset model; the second term is the contribution of the defect production.

2.5.1 Molecular dynamics simulations of atomic friction and wear

Continuum mechanics modeling has several limitations. First of all, this approach is not applicable for atomic-scale processes like stick-slip, but this can be overcome by referring to models like the Tomlinson's. The actual limit is the determination of the contact stiffness for contacts with just a few nanometers radius. The estimation of the contact area earlier presented leads to contact radii of atomic, or smaller, size, in contradiction to the minimal contact size given by adhesion forces. Macroscopic quantities, such as the shear modulus or the pressure, do not describe the effective mechanical behavior of atomic contacts. Because of these limitations a microscopic modeling including the atomic structure is needed. This purpose is satisfied by a *molecular dynamics* (MD) simulation of the contact. In such simulations, the sliding contact is modeled by boundaries of fixed atoms in relative motions; the atoms involved in contact can realize their positions according to interactions between each pair of atoms.

The first experiments carried out to analyze friction features were performed on layered materials, often graphite. Tang et al. developed a theoretical study

of forces between an atomically sharp diamond tip and a graphite surface. They noticed that there is a strong dependence between force and distance: the strongest contrast appeared at different distances or normal and lateral forces due to the strong displacement of surface atoms. The order of magnitude found in their study was 1 nN, which is much less than in many other experimental reports. Tang et al. also observed that the distance dependence of forces could even change the symmetry of the observed lateral forces. The same situation has been studied with numerical simulations, where a simplified one-atom potential for the tip-surface interaction has been used, considering also the spring potential of the probing force sensor. Their goal was to observe an hexagonal pattern in the friction force, while the surface graphite atoms are structured in a honeycomb shape. The simulation revealed how the jump path of the tip under a lateral force depends on the force constant of the probing force sensor.

The stick-slip phenomena on the atomic scale has been observed on surfaces of ionic crystals by several research groups, with a lateral force modulation of the order of 1 nN. The first performer of atomistic simulation of sliding contacts was Landman. His experiment, conducted by imposing a lateral movement to the tip, showed an oscillation with the atomic surface periodicity and an amplitude decreasing from 8 nN of the lateral force. Analyzing the atomic positions, a wear process by shear cleavage of the tip was found. Such transfer of atoms from the surface to the tip plays a key role in atomic friction.

Shluger et al. performed a simulation with a lateral scan using a MgO tip on a LiF(100) surface. Initially they noticed that there was an irregular oscillation of the system's energy with atoms transfer between tip and surface. After a while the tip structure changed because of the adsorption of Li and F ions. This phenomena showed up with a non-destructive sliding characterized by a regular oscillation of

the energy with the periodicity of the surface. The authors called this process self-lubrication, and deduced that, in general, a dynamic self-organization of the tip surface might promote the observation of periodic forces. In other studies, Tang et al. found that significant atomic force contrast can be expected with distance between tip and surface below 0.35 nm, but distances below 0.15 nm can result in destructive forces. Using the dynamic model in lateral force measurements, it is possible to obtain atomic resolution of defects when the regime distance is between 0.2 e 0.4 nm.

Recent experiments in atomic friction on ionic crystal surfaces include the velocity dependence of lateral forces and atomic-scale wear processes. In that situation, though, the molecular dynamics approach is not applicable because the actual scanning time scale is too far from the atomic relaxation time scales that govern MD simulations. Furthermore, the number of freely transferable atoms that can be included in a simulation is limited by meaningful calculation time. Landman et al. focused their studies on the high reactivity system constituted by a silicon tip sliding on a silicon surface. They observed a clear stick-slip variation of the lateral force. Intense atoms displacements created an interstitial atom under the influence of the tip, which is annealed when the tip is moved on. If the tip enters in the repulsive forces regime a permanent damage can be predicted [75, 55].

Chapter Three

Carbon Nanotubes

In the 1970's and 1980's, carbon filaments with diameters less than 10 nm were prepared by the decomposition of hydrocarbons at high temperatures in presence of transition metal catalyst particles. However, only in 1991 carbon nanotubes, usually referred to as CNTs, have been observed by Iijima [1]. They are seamless cylindrical structures made of sheets of graphite-like arrangements of C atoms, *graphene*, ranging from 4 to 30 nm in diameters and up to a few millimeters in length. Each sheet is a polyaromatic mono-atomic layer made of hexagonal display of sp^2 hybridized carbon atoms [75], and it constitutes the tube once it is rolled up about the filament axis. In this way the hexagons are organized in a helical structure characterized by a mirror symmetry. Carbon nanotubes exist in three forms: single walled nanotubes (SWNT) constituted of one atomic plane of carbon atoms perfectly rolled into a cylinder [79]; doublewalled nanotubes (DWNT) formed by two layers of graphene; multiwalled nanotubes (MWNT), characterized by concentric cylindrical shells of

graphene, where the intershell interaction is predominantly van der Waals [80].

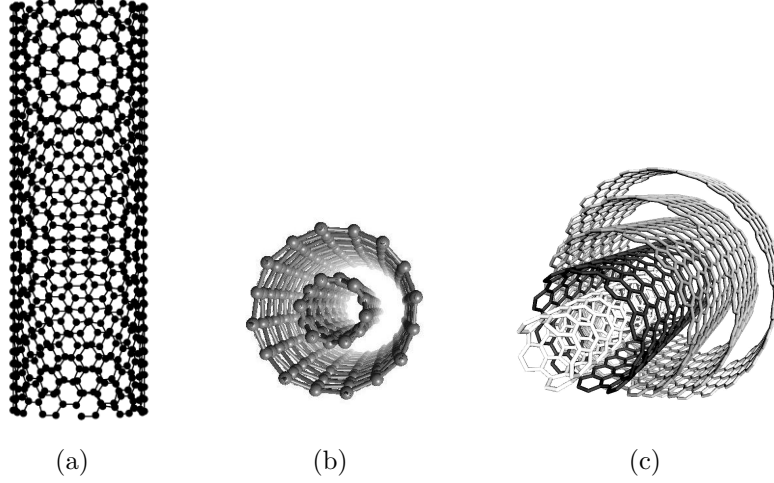


Figure 3.1: Structure of a (a) single walled nanotube; (b) doublewalled nanotube; (c) multiwalled nanotube

Despite structural similarity to a single graphite sheet, the electrical properties are different. Graphite is a semiconductor with zero band gap, while SWNTs can be either metallic or semiconducting, depending on the sheet direction about which the graphene sheet is rolled on. Their structure is explained in terms of the one-dimensional unit cell, defined by two vectors: the chiral vector \vec{C}_h and the translation vector \vec{T} . The SWNT circumference is completely described by the equation:

$$\vec{C}_h = n\vec{a}_1 + m\vec{a}_2 \quad (3.1)$$

which connects two crystallographically equivalent sections on a 2D graphene sheet. The nanotube type is thus denoted by the pair of integers (n,m) which describes the circumference. By rolling up the graphene sheet into a cylinder it is possible to obtain three different structures: the *zigzag* SWNT corresponds to the $n = 0$ or $m = 0$ case, with the chiral angle θ of 0° ; the *armchair structure* is characterized by a chiral angle of 30° , and $n = m$ integers; *chiral* nanotubes have θ value ranging between 0 and 30° and are characterized by any other value of n and m . From the

electrical point of view, all armchair SWNTs are metals; those with $n - m = 3k$, with k a nonzero integer, are semiconductors with a tiny band gap. All other SWNT structures are semiconducting with a band gap width inversely depending on the nanotube diameter.

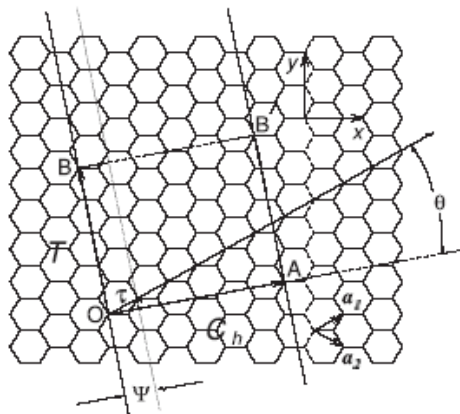


Figure 3.2: The chiral angle θ is defined by the chiral vector \vec{C}_h and the zigzag direction corresponding to $\theta = 0^\circ$. The honeycomb lattice of the graphene sheet is defined by the unit vectors \vec{a}_1 and \vec{a}_2

The weak bound, based on van der Waals forces, between cylinders constituting a multiwalled carbon nanotube make its electronic properties rather similar to those of a perfect SWNT. Because of the nearly one-dimensional electronic structure, electronic transport in metallic SWNTs and MWNTs occurs ballistically over long tube lengths. Such propriety enables CNTs to carry high currents with no heating.

3.1 Synthesis of Carbon Nanotubes

Synthesis of carbon nanotubes can be achieved by many different methods: laser ablation, arc discharge, pyrolysis or chemical vapor deposition are the oldest and more common ones. MWNTs can be grown without the employment of catalyst, where the use of metal catalyst species, such as the transition metals Fe, Co or Ni,

is a requirement for the SWNTs production [2].

The arc-discharge technique is conducted in a reaction vessel through which an inert gas, typically helium, flows at a controlled pressure. The carbon atoms are evaporated by plasma of the gas ignited by high currents passed through opposite carbon anode and cathode. By applying a potential of about 18 V, either AC or DC, between two graphite rods with different diameters placed in the vessel, Ebben et al. [3] noticed that as the smaller rod, whose diameter was about 6 mm, was consumed, a carbonaceous deposit formed on the second rod, and it contained nanotubes. The electric current depended on the rod dimensions, their separation and the gas pressure, but its value was typically about 100 A. The rate at which the rod deposit formed depended on the gas pressure, usually about 500 torr: in the best conditions, they found to be a few millimeters per minute. Such deposit formed a microscopic tubular structure packed with nanotubes. The core material containing the nanotubes, which could have been easily removed from the shell, had a fibrous structure, and the fibers were parallel to the current direction. Iijima [4] developed an arc-discharge method to grow SWNT by using two carbon rods of 10 mm and 20 mm diameters in a evaporation chamber with a gas mixture consisting in 10 torr of methane and 40 torr argon. By applying a DC current of 200 A at 20 V between the electrodes, and using a iron filing melted to form droplets, he obtained SWNT capped and with diameters that range from 0.7 to 1.6 nm. In a later work, Journet et al. [81] obtained single walled nanotubes with diameters around 1.4 nm and an average distance between them of 1.7 nm, by using a graphite rod of 16 mm diameter as cathode, and a 6mm-diameter graphite rod with a 3.5 mm diameter hole filled with a mixture of metallic catalyst and graphite powder as an anode in a helium atmosphere at 660 mbar pressure.

Smalley et al. developed a laser ablation method to grow high quality SWNT at the 1-10 g scale. Their technique utilized intense laser pulses to ablate a carbon

target, placed in a furnace heated to 1200°C, containing 0.5 atomic percentage of nickel and cobalt. In order to collect the grown downstream of nanotubes on a cold finger, a flow of inert gas was passed into the growth chamber during the ablation. The SWNTs obtained with this technique are mostly in the form of ropes consisting of tens of individual nanotubes close-packed into hexagonal crystals by van der Waal forces [2].

Endo et al. [82] applied a pyrolysis technique in order to produce carbon nanotubes. The apparatus they used was constituted by a ceramic reaction tube, where benzene and hydrogen were blew into, and an artificial graphite rod was centrally placed into it. The furnace temperature had been kept at 1000 °C for one hour. After that time, the temperature was let cool down to room temperature and hydrogen was replaced by argon. The substrate was then took out the reaction tube, and the nanostructures formed on it were heat treated in a carbon resistance furnace under argon at temperature between 2500 and 3000 °C for 10-15 minutes. In this way, multiwalled nanotubes with interlayer spacing of about 0.34 nm, length of 100 nm or more and diameter of about 10 nm were obtained. Satichkumat et al. [83], based on Terrones [84] method, employed a pyrolysis apparatus constituted by stainless steel gas flow lines and a two-stage furnace system fitted with a quartz tube with inner diameter of 10 mm. About 100 mg of presublimed ferrocene were placed inside the quartz tube, which was then placed in the first furnace, heated to 623 K at a fast heating rate (100°/min). An argon gas flow carried the ferrocene vapor into the second furnace, where the temperature was maintained at 1373 K. As the stream introduced the chamber, methane, acetylene or *n*-butane was introduced in the pyrolysis zone. This process allows the production of large quantities of aligned nanotube bundles with a length of a few tens of microns and diameters ranging between 2 and 13 nm.

The chemical vapor deposition (CVD) growth technique involves heating a catalyst material to high temperatures in a tube furnace and flowing hydrocarbon gas through the reactor for a period of time. Materials grown on the catalyst are collected upon cooling the system to room temperature. Typically, transition-metal nanoparticles formed on a support material such as alumina are used as active catalysts. In the CVD process, nanotubes grow by the dissociation of hydrocarbon molecules catalyzed by the metal particles, wherein carbon atoms are dissolved until saturation. From the saturated metal catalysts, carbon precipitates and forms tubular carbon solids in the sp^2 structure. Since the tube does not contain dangling bonds, it is a low energy form, therefore it is favored over the graphene sheet with open edge structure formation. The most common feedstock are ethylene or acetylene, and the growth temperature is usually in the range of 550-750 °C. Catalytic metals preferably used are iron, nickel or cobalt because at high temperatures carbon has finite solubility in these materials, leading to the formation of metal-carbon solutions that allow the growth mechanism described above.

Large arrays of aligned carbon nanotubes have been synthesized by Ren et al. [85] using a plasma-enhanced hot filament chemical vapor deposition (PE-HF-CVD) method. First a thin layer of nickel has been deposited on clean glass by radio frequency magneto sputtering at a working pressure of 20 to 60 mTorr. After the deposition of nickel, the samples were moved to a CVD chamber, where the pressure was pumped down to $6 \cdot 10^{-6}$ torr. Acetylene and ammonia gases were then blew into the chamber in order to maintain a working pressure in the 1-6 torr range. Once the working pressure was stable, a tungsten filament and the plasma generator were turned on to heat and generate plasma. The growth period lasted from 5 to 20 min, and it led to carbon nanotubes characterized by 20 μm in length and about 100 nm in diameter. Lee et al. [66] used CVD to grow aligned carbon nanotube on a large area of Co-Ni codeposited Si substrates using C_2H_2 gas. Co-Ni metal

alloys with 100 nm in thickness were thermally evaporated at room temperature in a vacuum of 10^{-6} torr on oxidized Si(100) substrates. The samples were then preheated using NH_3 gas at 800-900°C. CNTs were synthesized using C_2H_2 gas flow for 10-20 minutes at the same ammonia pretreatment temperature. At the end of the synthesis, the chamber was slowly cooled down at room temperature in argon ambient. With this process, it is possible to grow well-aligned nanotubes, with a 5 μm length and a diameter of about 200 nm. It has to be noted that the nanotubes present a transition-metal cap. As presented in Choi [86], Bonnot [87] and many other works, it is possible to grow CNTs with different properties and structures by changing catalysts characteristics or synthesis conditions.

3.2 Mechanical properties of carbon nanotubes

Graphite sheets have a very high elastic modulus. This propriety may make carbon nanotubes the stiffer and stronger elements in nanoscale devices ever known. CNTs have molecular size and morphology, but they also have enough translational symmetry to perform nanocrystals, with a well defined primitive cell. This allows their study as well defined engineers structures, and many properties can be discussed in traditional terms of moduli, stiffness, geometry size and shape.

The mechanical properties, whose understanding is important to any proposed application, are predicted to be sensitive to details of the carbon nanotubes structure, and to the presence of defects. In particular, the Young's modulus is directly related to the cohesion of the solid, and therefore to the chemical bonding of the constituent atoms. In the case of covalently bounded solids, the elastic properties of an ideal crystalline solid are determined by the shape of the potential energy of a pair of atoms, as a function of inter-particle separation. Thus, in order to determine mechanical properties, it is necessary to perform measurements on each nanotube.

Falvo et al. [45] repeatedly bent MWNTs using an AFM tip in order to observe their response to the high-strain deformation imposed. They noticed that carbon nanotubes are extraordinary flexible under large strain, and resist failure under repeated bending. In their experiments, they observed reversible, periodic buckling of nanotubes, consistent with calculation based on continuum mechanics.

Wong et al. [46] developed a method to directly determine the bending force as a function of displacement in order to obtain a measurement of the stiffness, strength and toughness of nanotubes. This technique involves the use of an AFM to acquire force-displacement curves, from which it is possible to calculate the Young's modulus of the CNTs. The tests were performed on MWNTs vertically aligned on molybdenum disulfide surfaces. By the AFM tip, different loads were applied along the axis of the nanotubes, at different positions from the fixed pinned point on the substrate. The $F-d$ curves acquired in this way showed a linear increase of the force with the increase of the displacement after the tip contacted the nanotube. This linear region decreased for data recorded at increasing distance from the pinning point. Such curves led to a value for the Young's modulus of 1.26 TPa, which is similar to the in-plane modulus of graphite, 1.06 TPa. By analyzing the $F-d$ curves they obtained, it has been noted that the initial linear slope abruptly decreased when nanotubes were deflected by relatively large amounts. This behavior corresponds to an elastic process. This ability to elastically sustain loads at large deflection angles enables carbon nanotubes to store or adsorb considerable energy. In this work, Falvo also evaluated the bending strength of MWNTs, which is defined as the strain determined at the initial buckling point. The maximum bending strength determined was 28.5 GPa; however, the average value was 14.2 ± 8.0 GPa. The toughness was quantified by integrating the measured $F-d$ curves, and it was found to be 100 keV for 30-nm-diameter nanotubes. Focusing on the measurement of the Young's modulus, Salvetat et al. [88] developed a method based on AFM imaging

with silicon nitride tips of CNTs deposited on an alumina ultrafiltration membrane at different loads. The average value of the Young's modulus for MWNTs with diameters in the range of 26-76 nm, was found to be 1.28 ± 0.59 TPa.

Yu et al. [50] built a manipulation tool inside a scanning electron microscope (SEM) to measure the stress-strain response and the strength at failure of single arc-discharge grown MWNTs under tensile load applied by an AFM tip. They obtained a Young's modulus for the outer layer in the range from 270 to 950 GPa; the strain at failure can be as high as the 12% change in length. The nominal engineering E values based on the cross-sectional area are found to be in the 1.4-1.9 GPa range for the nominal tensile strength, and between 18 and 68 GPa for the elasticity modulus. It has to be noted that the strength of the nanotubes is significantly affected by the presence of defects in their structure. Yu's group extended this method to the study of the elastic modulus of ropes of SWNTs [89]. The average breaking strength of the perimeter SWNTs ranged from 13 to 52 GPa, and the average Young's modulus, obtained by the linear fit of the measured stress-strain curves, was found to be in the 320-1470 GPa range. They did not notice any dependence of the strength or the E value on the rope diameter.

Large amplitude deformations, beyond the Hookean behavior, have been observed in carbon nanotubes. This reveals nonlinear properties of CNTs, unusual for other molecules or for the graphite fibers. If external loads are applied to the nanotubes, they accommodate significantly changing their shape without any irreversible atomic rearrangements. Under compression and bending stresses, they develop kinks or ripples; if twisted, they flatten into deflated ribbons. The resilience is unexpected for graphite-like materials, but it can be explained by the small dimensions of nanotubes, which do not allow the formation of stress-concentrators such as micro-cracks or dislocation failure piles. Numerous experimental observations show the capability of CNTs to sustain significant nonlinear elastic deformations.

Nakajima et al. [49] measured the elastic moduli of identical CNTs, analyzing the bi-linear reaction to an applied bending moment. They conducted their measurements both by buckling process and by electromechanical resonance. The Young's modulus value found for the first case was 1.87 GPa, where the electromechanical resonance method led to a 43 GPa value. The difference between the two moduli is due to the fact that in static measurements, by buckling of a CNT, its elasticity is in the first bi-linear region, which means that the force is small enough for non emergence of the wavelike distortion or ripples on the inner arc of the bent CNT; this bending mode is referred to as the ripping mode. On the contrary, by dynamic measurements, the elasticity falls apparently because it must be involved the ripping mode of CNTs.

Vertically aligned carbon nanotubes (VACNT) have been subject of investigation due to their numerous potential applications ranging from field emission and vacuum microelectronic devices to the creation of super-hydrophobic surfaces and a source of well defined CNTs. In order to study VACNTs mechanical properties, Qi et al. [90] proposed a method based on nanoindentation tests conducted with an AFM, following the standard procedure. Based on their indentation test on a MWNT forest by a diamond tip, the effective bending modulus ranges from 0.91 to 1.14 TPa, and the effective axial modulus to be in the 0.9-1.23 TPa range.

3.3 Carbon nanotubes applications

Carbon nanotubes have many outstanding properties, such as well-defined geometries, high aspect ratio, high tensile strength, low mass density; moreover they are chemically inert, high electron and heat conductive. Therefore they have been regarded as promising materials for nanostructures and nanodevices; in many cases, CNTs are regarded as ultimate one-dimensional wire and applied the linear model

for analysis. Many nanotubes can form secondary structures such as ropes, fibers, papers and thin films with aligned CNTs, all with their specific properties. The main limit is their cost, which depends on both the quality and the production process. However, carbon nanotube synthesis is constantly improving, and sale prices are falling rapidly. Therefore the application of carbon nanotubes is a very fast moving field.

Near-field microscope probes

The mechanical robustness of nanotubes, and the low buckling force make CNTs exceptional candidates for use as force sensors in SPM, since their properties increase probe life and minimize sample damages during repeated hard crashes into substrates. The cylindrical shape and the small diameter of the nanotubes enable imaging in narrow, deep crevices, and improve resolution in comparison to conventional SPM probes. Commercial nanotube-based tips use MWNTs for processing convenience. This choice is also supported by the fact that the flexural modulus of a SWNT is too low, resulting in artifacts that affect the lateral resolution when scanning a rough surface. A very interesting potential of such tips is the possibility to be functionalized. This means that it could be possible to image selectively basing on chemical discrimination in chemical force microscopy (CFM). Ideally, the very tip of the nanotube can be functionalized, so the interactions between the chemical species on the tip and the chemical functions present on the surface of the scanned sample can be recorded with great sensitivity, allowing the chemical mapping of molecules.

Field emission devices

Applications of SWNTs and MWNTs in electronic devices use them as field emission electron sources for flat panel displays, lamps, gas discharge tubes providing

surge protection, and X-ray and microwave generators. The principle of a field emission-based screen is based on the high local fields generated by a potential applied between a CNT-coated surface and an anode, as the result of the small radius of the nanofiber tip and the length of the nanofiber. These local fields cause electrons to tunnel from the nanotube tip to the vacuum. Electrons are directed toward the anode by the electric fields, and there a phosphor produces light. Replacing the glass and protecting the electron-sensitive screen using a polymer-based material should even permit the development of flexible screens.

Nanotube field-emitting surfaces are relatively easy to manufacture by screen-printing nanotube pastes and do not deteriorate in moderate vacuum (10^{-8} torr). The structural perfection of nanotubes allows higher electron emission stability than regular metallic electron-emitting tips, higher mechanical resistance, longer lifetimes and low emission threshold potentials. Their application saves energy even because the tip works at lower heating temperature.

Nanotube-based lamps are similar to displays in comprising a CNTs-coated surface opposing a phosphor-coated substrate, but they are less technically challenging and require less investment. High-performance lamps show a more than 8000 hours lifetime, high efficiency for green phosphors of environmentally problematic mercury-based fluorescent lamps, and the high luminescence required for large stadium-style displays.

Replacing the phosphorescent screen with a metal target and increasing the accelerating voltage X-rays, instead of light, are emitted. Probably due to the narrower energy range of the impacting electrons than that for thermoionic electron sources, the resulting X-ray source allows a higher quality imaging of biological samples. The compact geometry of nanotube-based X-ray tubes suggests their possible use in X-ray array for medical imaging, possibly even for X-ray endoscopes.

Chemical sensors

The nanotube electronic transport and their voltage between junctions, caused by interjunctions temperature difference (thermopower), are very sensitive to changes in the chemical composition of the surrounding atmosphere at room temperature, due to charge transfer between the nanotubes and the molecules from gases adsorbed onto SWNT surfaces. It has been shown that there is a linear dependence between the concentration of the adsorbed gas and the change in the electrical properties, and that the adsorption is reversible. The main advantage is the minute size of the nanotube sensing element, therefore only a very small amount of material is required for a response. Moreover, they can operate at room temperature, they have a high selectivity and the sensitivity of such nanotube-based sensors are three order of magnitude higher than those of standard solid state devices.

Catalyst support

Activated carbons are currently employed as catalyst supports due to their high surface areas, their stability at high temperatures under nonoxidizing atmospheres, and the possibility of controlling both their porous structure and the chemical nature of their surfaces. The morphology and size of carbon nanotubes, in particular their aspect ratios, can play significant role in catalytic applications due to their ability to disperse catalytically active metal particles. Their electronic properties are also of primary importance, since the conductive support may cause electronic perturbations as well as constraining the geometries of the dispersed metal particles. Their mechanical strength is also important, since it makes them resistant to attrition when recycled. Their internal and external surfaces are strongly hydrophobic and adsorb organic molecules strongly. With nanotube supports, the mass transfer of the reactants to the active sites is unlimited, due to the absence of microporosity (pores < 2 nm), and the apparent contact time of the products with the catalyst is

diminished, leading to more active and more selective catalytic effects.

Application related to adsorption

The adsorptive properties of carbon nanotubes can be applied in chemical sensors, as far as molecular absorption is concerned, or in gas storage and separation. The possibility of storing gases, hydrogen in particular, has received most attention for the potential use in highly efficient H₂ fuel cells in transportation vehicles. Many studies focused on this application, but neither experimental nor theoretical results are yet able to demonstrate that an efficient storage of hydrogen is possible for carbon nanotubes. Further efforts have to be made to enhance the quality of these materials, in particular by adjusting the surface properties and the structure of the material, such as the pore size.

Precise separation tools could be developed using carbon nanotubes, since they have regular geometry that can, to some extent, be controlled. If the sorption mechanisms are known, it should be possible to control sorption of various gases through particular combinations of temperature, pressure and nanotube morphology. This field is still at its beginning phase, so no actual devices have yet been developed.

The shown capability of carbon nanotubes to adsorb some toxic gases such as dioxins, fluoride, lead and alcohols, makes CNTs suitable for cleaning filters applications in many industrial processes with hazardous by-products. Experimental results obtained so far suggest promising applications, but further work is still needed.

Nanometers biosensors can be obtained by attaching molecules of biological interest to carbon nanotubes. The interaction between the probe and the studied medium would lead to chemical changes or interactions with the target species, hence the electrical conductivity of the functionalized nanotubes would be modified. Using the internal cavities of CNTs to deliver drugs would be another interesting application, but the toxicity of the carbon nanotubes into the human body still needs

further investigation. Nanotube-based biosensors already developed are based either on field effect transistors involving CNTs functionalized with biomolecules, or on electrochemical detection.

Applications related to composite systems

Carbon nanotubes are looked at as promising reinforcement materials on composites with ceramics, metals and polymers thanks to their exceptional morphological, electrical, thermal and mechanical characteristics. Many variables have to be taken into account in order to determine the structural perfection, surface reactivity and aspect ratio of the reinforcement: the good dispersion of the nanotubes, the good control of the nanotube/matrix bonding, the densification of bulk composites and thin films, the nanotube type and origin. Nanotube-metal composites are still rarely studied. On the contrary, much more effort has been focused on CNTs-ceramic matrix composites in order to obtain tougher ceramics. Composites can be processed using the regular processing procedures, where the nanotubes are usually mechanically dry or wet mixed with the matrix and then densified using hot-pressing sintering. The first realized major commercial application of MWNTs is their use as electrically conducting components in polymer composites. Nanotubes-polymer composites have now been intensively studied, in particular the epoxy-polymethylmethacrylate (PMMA)-matrix composites. The strength and toughness of the fibrous reinforcement, its orientation and good interfacial bonding are the three main variables which affect the mechanical characteristics of the composites. The strong bond between the reinforcement and the matrix is achieved by the ability of the polymer to form large-diameter helices around individual carbon nanotubes. The weak frictional interactions between layers of MWNTs and between SWNTs in bundles make isolated SWNTs preferable than MWNTs or bundles for dispersion in a matrix. The main mechanisms of load transfer are micromechanical interlocking,

chemical and van der Waals bonding between the fibers and the matrix. When a high interfacial shear stress occurs, it transfers the applied load to the fiber over a short distance. It has to be noted that two critical issues have to be considered when using nanotubes as components for advanced composites: one is to choose between single and multiwalled nanotubes, the other is to tailor the nanotube/matrix interface with respect to the matrix.

One of the major benefits expected from incorporating carbon nanotubes into other solid or liquid materials is that they endue the material with some electrical conductivity while leaving the rest of the properties or behaviors unaffected. The adjustment of the nanotube volume fraction in the formerly insulating material allows to obtain the desired electrical conductivity of a bulk material.

It is often a requirement for materials to be multifunctionals; for examples, to have both high electrical conductivity and high toughness, or high thermal conductivity and high thermal stability. This goals have usually been achieved by associating several materials, each of them bringing one of the desired features. The exceptional features and properties of CNTs make them likely to be a perfect multifunctional material in many cases.

As reported earlier in the chapter, SWNTs can be either metallic or semiconducting. Metallic SWNTs can be used as mere ballistic conductors, or they can be one component of a rectifying diode by joining it with a semiconductor SWNT. Moreover, by attaching a semiconductor SWNT over two electrodes deposited on an insulating substrate working as a gate electrode, field effect transistors (FET) can be built. The association of two of such FET makes a voltage inverter. SWNT-based integrated circuits are not constructed on a routine basis yet since progress is still needed. First, it is necessary to be able to selectively prepare metallic or semiconducting nanotubes, then it is mandatory to develop a method to obtain

defect-free nanotubes. By exploiting graphene ability to expand slightly when electrically charged, nanotubes can act as actuators. Different studies have been carried out on nanotweezers and nanothermometers design, demonstrating the ability of CNTs to provide building blocks for future nanodevices, including nanomechanical systems.

Speaking on a wide application basis, in the automotive gas lines and filters, the nanotube filler dissipates charge buildup that can lead to explosions and better maintains barrier properties against fuel diffusion than do plastic filled with carbon black. Plastic semiconductor chips made from carbon nanotube composites avoid contamination associated with carbon black sloughing. Similar materials are also used for conductive plastic automotive parts, such as mirror housing that are electrostatically painted on the assembly line, thereby avoiding separate painting and associated color mismatch.

Because of the high electrochemically accessible surface area of porous nanotube arrays, combined with their high electronic conductance and useful mechanical properties, CNTs can be used as electrodes for devices that use electrochemical double-layer charge injection. An example is given by supercapacitors: they consist of two electrodes immersed in an electrolyte, separated by an insulating ion-permeable membrane. The capacitors are charged by applying a potential between the two electrodes; in this way the cations and the anions move toward the oppositely charged electrode. In contrast to ordinary planar sheet capacitors, the capacitance for an electrochemical capacitor depends on the distance between the electrode and the countercharge in the electrolyte. Since in a superconductor this separation is about a nanometer, very large capacitance result from the high nanotube surface area accessible to the electrolyte. In fact, the surface area should consist of an appropriate combination of mesopores, so the electrolyte components can circulate well in relation to the charging speed, and micropores, whose walls provide the attractive

surfaces and fixations sites for the ions. This capacitances, between 15 and 200 F/g, result in large amounts of charge injections when only a few volts are applied. This charge injection is used for energy storage in nanotube supercapacitors, and to provide electrode expansions and contractions that can do mechanical work in electromechanical actuators. Current work in this area will lead to further optimization of both the nanotube material architecture and the nanotube-supported conductive polymers [10, 12].

Chapter Four

Nanotribological characterization of carbon nanotubes

Carbon nanotubes are of great importance for various applications, from field emitters, molecular transistors, microfluidics, biosensors, to fillers in nanocomposites, biomimetics, nanotwizers, functionalized devices for biomedical and optoelectronic applications, electrode devices for flat panel displays [6, 7, 8, 9, 10, 11, 12].

Because of their small radii and their high mechanical robustness, individual carbon nanotubes are well suited for atomic force microscopy probes [13, 14, 15]. In fact, the cylindrical shape and the small diameter of the nanotubes enable imaging in narrow, deep crevices, and improve lateral resolution in comparison to conventional AFM probes [16].

Due to their mechanical strength, combined with their low density, carbon nanotubes seem to be the optimal fillers in composites with various materials. Different

studies have demonstrated that the use of carbon nanotube in polymeric matrices can considerably improve the mechanical properties and tribological of the composites [17, 18, 19, 20, 21, 22, 23]. CNT metallic composites are interesting for their high wear resistance [24, 25, 26, 27, 28], and their thermal properties, making them suitable for high thermal management of high power devices [29]. Carbon nanotubes have also been added to ceramic matrices. In particular, it has been shown that they can improve the elastic deformation characteristics and the fracture toughness of SiC and alumina matrices [30, 31, 32, 29].

It has been observed that the vertical orientation of CNTs with respect to the substrate increase the field emission of such nanostructures [33, 34], and it can also affect their thermal properties [35]. It is then of interest to study the aligned nanotube arrays.

It is of interest to create nanofiber structures using CNT arrays for various applications, including mimicking gecko feet and lotus effect [36, 37, 38, 39].

Focusing on the CNT tips, although many studies on their characteristics have already been reported, all of them have been conducted in tapping mode. Nguyen et al. [40] analyzed the stability and the lateral resolution capability of CNT scanning probes applied to AFM, using a MWNT and a SWNT probe. By imaging in tapping mode, they compared the resolution reachable using CNT tips or conventional silicon probes. With this work, Nguyen and coworkers illustrated how the MWNT probe does not degrade after a long period of continuous scanning (more than 15 hours) and how the SWNT probe is capable of lateral resolution as small as 2 nm. Larsen et al. [41] compared the wear and degradation of conventional commercial etched-silicon probes with those of multi-walled carbon nanotubes during tapping mode imaging on fragile samples, such as a polycrystalline silicon surface. Their tests led to the conclusion that using a CNT tip, neither the sample nor the probe is affected by the imaging of over 1100 scans. In a later work, Guo et al. [42] conducted

experiments on wear characteristics of CNT and silicon probes. Their tests led to the conclusions that CNT probes are wear resistant, accordingly featuring a good anti-wear characteristic and a long lifetime, compared to silicon probes; and that CNT tips produce much less damage to the scanned sample when compared to silicon probes.

The mechanical properties of the CNTs have been studied using theoretical and experimental methods. Nonlinear elastic responses and mechanical robustness of nanotubes and nanorods have been analyzed by various researchers [43, 44, 45, 46, 47, 48, 49]. Yu et al. [50] analyzed the breaking mechanism of MWNTs under tensile loads, while Daraio et al. [51, 52] focused on the dynamic nanofragmentation mechanism, the nonlinear contact interaction and the impact response of carbon nanotube forests. Cao et al. [53] reported the fully reversible compressive behavior of CNT films.

Besides the analysis of the mechanical properties, the understanding of the nanotribological behavior, such as the adhesion and the friction, between the CNTs and different materials plays a key role in the exploration of new applications for the CNTs [54, 55]. Kinoshita et al. [56] studied the frictional behavior of a vertically aligned carbon nanotubes forest against an atomic force microscope gold tip in air. Turq et al. [57] focused on the effect of the environment on the tribological properties of vertically aligned carbon nanotubes. Their experiments were conducted using a gold tip, under controlled relative humidity varying from 0 to 100%. Due to the micrometer scale of the tip radii and of the applied forces, these studies concern the microtribological characterization of the samples more than their nanometer scale analysis. Due to the emerging potential application of the nanotubes in structures which mimic the gecko feet and lotus effect and in composites in order to achieve different properties, such as the electrical conductivity or the improvement of the mechanical strength of polymer composites, the analysis of the interaction between

the CNTs and different materials on a nanometer scale is still needed.

In this context, an accurate nanotribological characterization of CNT AFM tips is still needed, in terms of adhesive and friction investigation on different materials, as well as a wear resistance analysis. Moreover, a tribological characterization of CNT arrays is scarcely reported and focused on the micrometer scale analysis of the tribological behavior of aligned carbon nanotubes.

4.1 Experimental

4.1.1 AFM tips

The multi-walled AFM tip used in this study is shown in Fig.4.1. Low-density

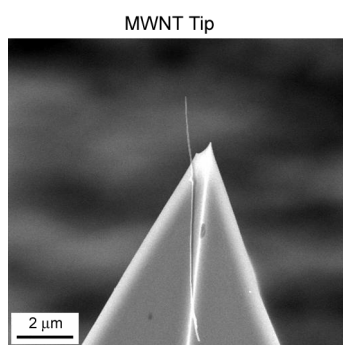


Figure 4.1: SEM image of the MWNT tip

and individually separated multiwalled carbon nanotubes (MWNTs) were grown by chemical vapor deposition on a Pt wire coated with a liquid catalyst solution as previously reported [58]. Using an inverted microscope at 500x magnification, a single MWNT with typical length greater than 10 μm was transferred to the tip of a Si cantilever that was coated with a 15 nm Ni Film. The relative position of the MWNT to the Si tip was manually manipulated using a pair of microtranslators. When the nanotube and the Si tip were in close proximity, an electrical potential of 1-2 V was applied in order to improve the alignment of the nanotube with respect to

the apex of the Si tip. Once the desired alignment of the nanotube is achieved, the MWNT was detached from its source by increasing the voltage to 10 V and above. The detachment occurs at the point of defects along the length of the MWNT due to Joule heating at this highest electrical resistivity. The applied voltage also caused local heating at the MWNT-Ni-coated-Si-tip interface, which strengthens the interface through perhaps physical welding the MWNT to the Ni film and/or formation of chemical bonds between the MWNT and the Ni-coated Si tip. The diameters of the MWNT tips typically ranged from 10-30 nm, with a length, beyond the silicon structure varying widely from a few μm to tens of μm . The MWNT are open, since their diameter is relatively large for cap closing to occur. The cantilever has a resonance frequency of about 75 kHz and nominal force constant of 2 N/m. The actual length of the cantilever has been measured with an optical microscope to be about 200 μm . The total height of the tip, including the supporting silicon tip structure and the length of the attached MWNT tip is approximately 17 μm , with the length of the nanotube protruding beyond the Si apex to be about 2 μm , as seen in Fig.4.1.

For comparison, a force modulation etched silicon tip (RFESP, Veeco) and an oxide-sharpened silicon nitride tip for dimension (NP-S, Veeco) were used for the same measurements of the adhesion force and the coefficient of friction. The RFESP silicon tips are made from a 0.5-2 Ωcm phosphorus (n) doped Si (100) wafer by being cleaned in hot HCl:H₂O₂:DI water, etched in 6:1 HF:DI water buffered with ammonium fluoride, followed by potassium hydroxide, hot phosphoric acid, and then HF etching. After etching, the tips are rinsed in DI water and blow-dried with nitrogen that had flow through a plastic tube. The length of the cantilever on the tip is 225 μm , its nominal resonance frequency is 75 kHz, and its nominal spring constant is 3 N/m. The nominal tip height is 15 μm , with a nominal radius of about 10 nm. Silicon nitride tips are held by a cantilever with 115 μm nominal length and 0.58 N/m nominal spring constant. Their height is in the 2.5-3.5 μm range,

and their nominal tip radius is 20-50 nm. The tests on the vertically aligned CNTs arrays have been performed with two etched silicon tips (RFESP, Veeco).

4.1.2 Test samples

In order to study the effect of the MWNT tip interacting with different materials, the tests were performed on single crystal silicon (100), mica, single crystal aluminum, and gold film samples. The first represents a ceramic material, while the second two represent ductile metals. The gold film is 100 nm thick and was deposited on a silicon substrate by evaporation.

For the second part of the study, two different vertically aligned carbon nanotubes arrays were tested (Fig.4.2). One array is composed of SWNTs, with diame-

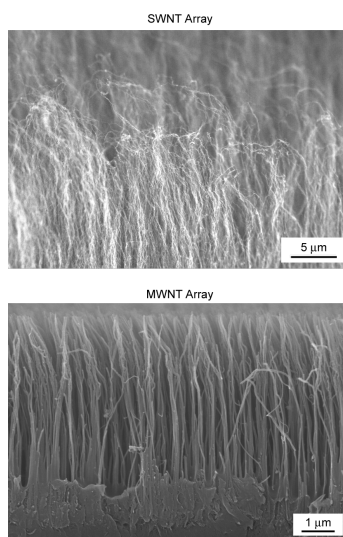


Figure 4.2: SEM images of the CNT arrays used for the study

ter less than 5 nm. The second array is formed by MWNTs, with diameter between 20-50 nm. For the two arrays, the length of the nanotubes is between 5 and 10 μm. The nanotubes are open with no capping. The aligned SWNTs were synthesized by deposition of ~1 nm Fe on Al (~10 nm) coated SiO₂/Si substrate, followed by

PECVD (80 W, 13.56 MHz) of ~ 30 mTorr C_2H_2 for 10-15 minutes at 750 °C. After the synthesis, the SWNTs were transferred onto gold film by sputter coating, followed by $\sim 10\%$ HF aqueous solution etching [59]. The aligned MWNT/polymer sample was prepared according to the method of Qu and Dai [60]. An appropriate polymer thin film, polystyrene (PS) in our case ($M_w = 350,000$; T_g (glass transition temperature) ~ 105 °C; T_m (melting point) ~ 180 °C; T_c (decomposition temperature) ~ 350 °C; thickness: ~ 50 μm) was first placed on the top surface of a vertically aligned carbon nanotube array [59]. By heating the SiO_2/Si substrate by an underlying hot plate to a temperature above T_m and below T_c , the melted PS film gradually filtrated into the nanotube forest through a combined effect of the gravity and capillary forces. The infiltration depth (i.e. the embedment length) of PS into the nanotube forest depends strongly on the temperature and heating time. After a predetermined heating time, the polymer-infiltrated nanotube array was peeled off from the SiO_2/Si substrate in an aqueous solution of HF (10% wt) to generate a free-standing film of vertically aligned carbon nanotubes embedded into the PS matrix.

4.1.3 Adhesive force, friction force, and wear measurements

Adhesive and friction forces were measured using a MultiMode AFM (Digital Instruments, Santa Barbara, CA). The adhesion force calibration and the friction measurements with the Si and Si_3N_4 tips were carried out on a 2 μm scan line, with a 4 $\mu\text{m}/\text{s}$ tip velocity (corresponding to 1 Hz scan rate) and 90° scan angle, with applied normal load ranging from 0 to 250 nN. Three sets of measurements for each tip on each sample have been performed, increasing and decreasing the applied load for three times [55]. The corresponding coefficients of friction were evaluated following the method II presented by Ruan and Bhushan [61]. The coefficient of friction is obtained from the slope of the average TMR (Trace Minus Retrace) vs normal load

curves, whose values are monitored during the scan of the tip perpendicularly to the cantilever long axis direction. With the carbon nanotube tip, the same settings were used, except for the scan angle, which was kept at 0° in order to scan the tip parallel to the cantilever long axis direction as required by method I of Ruan and Bhushan [61] procedure. The coefficients of friction were obtained from the slope of the average TMR vs. Z central position value. Friction data was collected for three loading and unloading cycles on three different locations for each sample.

The wear tests were performed on a $2 \times 2 \mu\text{m}^2$ area, with a scan velocity of $4 \mu\text{m/s}$, corresponding to a scan rate of 1 Hz, with a normal load applied to the cantilever using 100 and 200 nN [55]. In order to analyze the sample wear, the surfaces were scanned in the tapping mode after each test. To measure the tip wear, the method proposed by Tao and Bhushan [62] was followed. When scanning an isolated structure that is much sharper than the tip, the resulting image is a scan of the tip itself. Therefore, a silicon TGT1 grating sample (NTMDT, Moscow, Russia) was scanned with the CNT tip and one of the etched silicon tips for the preliminary tip characterization. The grating sample has an array of sharp tips on the surface, arranged on each corner and the center of a $3 \times 3 \mu\text{m}^2$ square. The height of each tip is $0.4 \mu\text{m}$, the tip angle is about 30° , and the radius is less than 10 nm. The scanning was performed on a $2 \times 2 \mu\text{m}^2$ area, at an average tip velocity of $2 \mu\text{m/s}$, corresponding to 0.5 Hz scan rate, in the direction parallel to the cantilever axis. SPIP software (Image Metrology A/S, Denmark) was used to characterize the tips used for the tests, and to evaluate their radii and cone angles. The image was obtained by scanning the TGT1 grating sample, then the surface of the tips were generated using blind tip reconstruction algorithm from the scanning image. A 2-D profile was generated from the tip surface for each tip. The characterization of the shape of the MWNT tip using the SPIP software could not be carried out due to the structure of the nanotube. Since its end is open, its radius is infinite. Therefore

it is not possible to image it using the silicon grating.

All experiments have been performed in ambient conditions, at 22 ± 1 °C and 45-55% relative humidity.

4.2 Results and discussion

4.2.1 Adhesive forces and friction measurements

MWNT Tip on Si, Al and mica samples

The force calibration plots obtained from our measurements of adhesive forces, reported in Fig.4.3, show a nonlinear behavior that can be related to the effects of the tip-surface interactions. The nanotube on the tip comes in contact with the surface

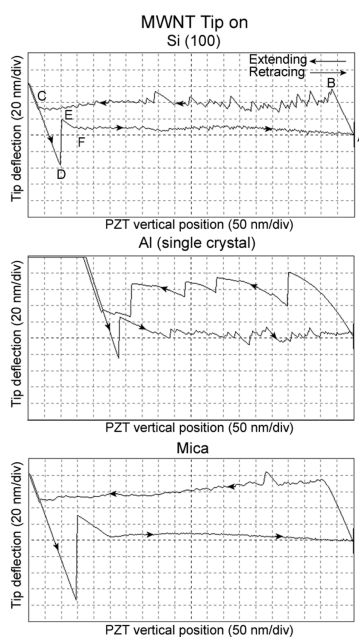


Figure 4.3: Force calibration plots using the MWNT tip on the Si, Al, and mica samples

(point A). As the tip continues to be pressed, the contact forces cause the linear deflection of the cantilever. After this initial bending, as the tips travels toward

the sample (from B to C), the cantilever deflection (load) remains about constant with some variations. A similar nonlinear behavior has been observed operating the AFM in tapping mode by Lee et al. [63]. The nonlinear behavior indicates that, as the tip is continuously pushed into the surface, it induces the MWNT to bend and buckle, and the nanotube deflection is more than the cantilever deflection (Fig.4.3). It is noted that during buckling, the graphitic C-C bonds, more specifically the σ and π bonds along the sp^2 hybridized chains, transform from the sp^2 to the sp^3 hybrid form when a mechanical stress is imposed along the nanotube axis. Such transformation is due to the breakage of the π C-C bonds, and it is reversible since the sp^2 C-C bonds are more thermodynamically stable than the sp^3 bonds [64]. The nanotube buckles until the applied force reaches the Euler buckling force [65]:

$$F = \frac{2EI}{L^2} \quad (4.1)$$

where E is the MWNT Young's modulus (1 TPa, [46]), I is the area moment of inertia ($I = (r_2^4 - r_1^4)/4$ where r_1 and r_2 are inner and outer radii of the nanotube, $r_2 \sim 10$ nm for the tip) and L is the nanotube length (2 μ m). Above the buckling force, the MWNT becomes unstable and buckles sideways, and lies on the surface and slides. The buckling force for the nanotube tip under study is calculated to be about 20 nN. This suggests that, since the load being applied at point B (~ 100 nN) is on the order of the buckling force, the nanotube buckles from point B to C and lies sideways. Friction between the nanotube and the surface with some roughness and continuous bending of the nanotube is responsible for the some variations observed from point B to C.

At point C, the silicon tip supporting the MWNT snaps into contact with the surface, inducing a linear deflection of the cantilever. When the tip is retracted by the piezo (point D), the elastic force of the cantilever overcomes the adhesion between the tip and the sample, the tip jumps out of contact (point E). Once the silicon tip jumps out of contact (point E), the elastic energy stored by the

MWNT is released (from E to F). After that, the bent MWNT will gradually unload its stress accumulated earlier in the extending regime, when the tip continuously moves away from the sample. This process is expected to generate a repulsive force comparable to that in the extending regime as shown by Lee et al. [63]. However, this is in contradiction to what we observed since the cantilever deflection during the retracting regime F-A is significantly lower than that during the extending regime B-C. The discrepancy here is explained by the change in sliding direction between the MWNT and the sample. The friction force reverses its direction when the silicon tip detached from the sample surface, reducing the stress stored in the MWNT instead of increasing it during the extending regime B-C. In addition, the deflection at point E is just in the middle of point C and point F, corresponding to an intermediate status before the friction force reverses its direction.

From the force calibration plots, the adhesion forces have been estimated (D-E), and the corresponding values are reported in Tab.4.1. It is a joint contribution

Sample	Tip		
	Si	Si ₃ N ₄	CNT
Si	80	250	40
Al	150	200	25
Mica	200	200	30

Table 4.1: Adhesive forces (nN) with different tips on various samples

from the adhesion between the silicon tip supporting the MWNT tip and the bent MWNT tip with the sample as well as the elastic stresses stored in the bent MWNT. Although we cannot exclude the possibility that during the jumping-out event, the MWNT lying on the sample surface might be slightly peeled off, the contribution to the measured adhesion from peeling of the MWNT can be safely neglected since the peeling length should be no longer than the jumping-out distance of 50 nm, which is much smaller than the length of MWNT itself $\sim 2 \mu\text{m}$. Moreover, as reported by Barber et al. [67], CNTs have a contact angle of about 80° , and they are better

wetted by water than graphite because of their higher polar energy component, but their structure is still hydrophobic. Therefore, any interactive capillary forces from the peeled segment of the MWNT tip should not make a large contribution to the observed adhesive forces. These values may be attributed to the combination of the bent nanotube in sliding contact and the Si tip in static contact with the sample.

For comparison, the adhesive forces have also been estimated using a Si and a Si_3N_4 tip, and the data are presented in Fig.4.4. The adhesion experienced by the

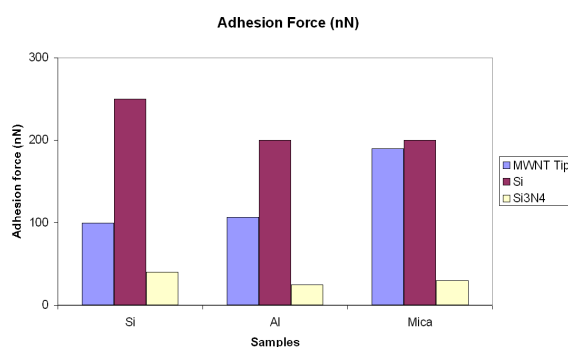


Figure 4.4: Mean values of the adhesive forces with various tips on three different samples. The σ values are about 15% of the mean values

silicon tip is the highest. This can be explained with the higher capillary force to which silicon is subjected to due to its low contact angle of 51° [62]. Silicon nitride is characterized by a contact angle of 48° [91], therefore the adhesive force should have a magnitude compared to the one observed for the silicon tip. The difference in the adhesion may be related to the differences in surface energy [54].

For the MWNT tip sliding on different samples, the coefficients of friction has been evaluated, and the data are presented in Fig.4.5 and Tab.4.2.

The coefficients of friction evaluated with the MWNT tip on the silicon and the mica surfaces are slightly higher than the values measured using the Si and the Si_3N_4 tips. Such trend can be due to the surface chemistry and the bending of the nanotube during the scan. As the tip is pushed against the surface, the nanotube

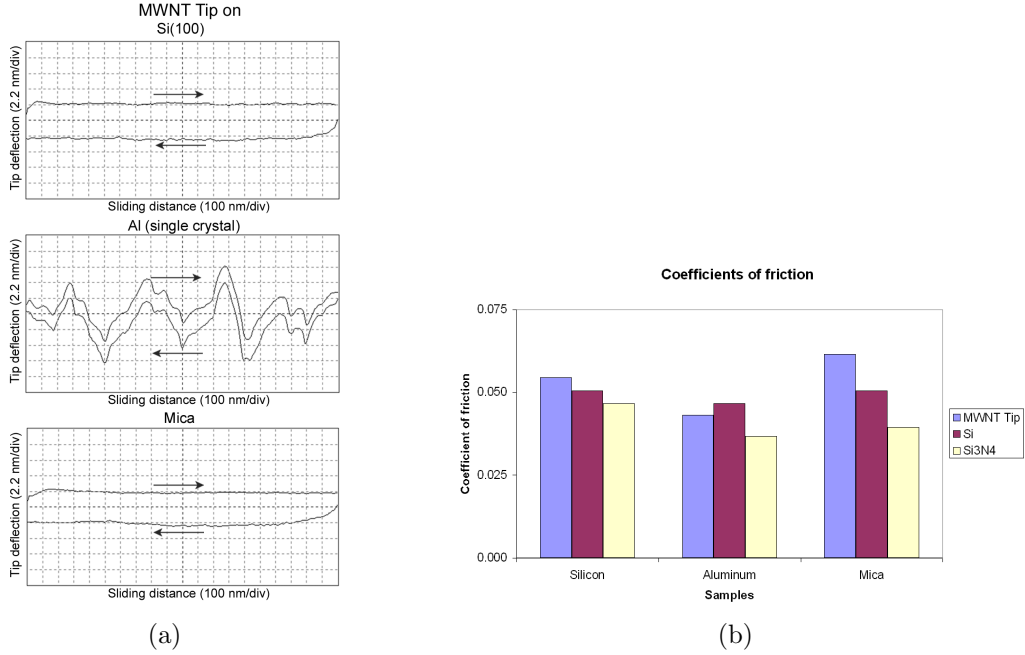


Figure 4.5: (a) Vertical deflection of the MWNT tip on the Si, Al, and mica samples during the friction measurements; (b) mean values of coefficients of friction for various tips on three samples. The σ values are about 15% of the mean values

Samples	Tips		
	Si	Si ₃ N ₄	CNT
Si	0.051	0.047	0.054
Al	0.047	0.037	0.043
Mica	0.050	0.040	0.061

Table 4.2: Coefficients of friction with different tips on various samples

buckles and bends laterally, leading to an increase of the contact area, which causes higher resistance to tip motion. In the case of the Al sample, the large variation of lateral deflection signals appears to be the consequence of the surface roughness.

Si tip on SWNT and MWNT arrays

The adhesion experiments were performed on the SWNT and the MWNT arrays, whose AFM images are shown in Fig.4.6. The data are presented in Tab.4.3.

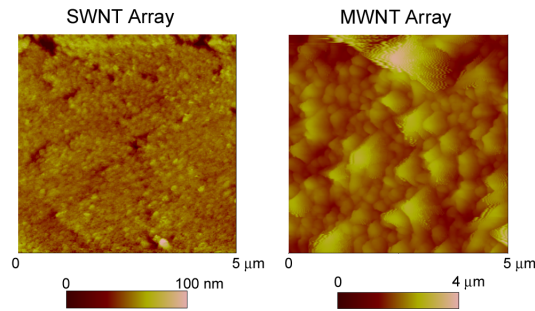


Figure 4.6: Tapping mode images of the SWNT and the MWNT arrays

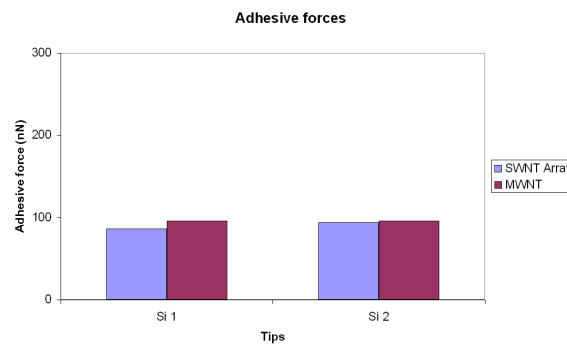


Figure 4.7: Mean values of the adhesive forces with Si tips on the CNT arrays. The σ values are about 40% of the mean values

Based on the adhesion force values presented in Fig.4.7 the values are lower for the SWNT array as compared to that for MWNT array.

The force calibration curves of the Si tip on the SWNT and MWNT arrays are shown in Fig.4.8. From those force plots it can be observed that, once the engagement occurs with the surface and the tip is pushed further, the cantilever is smoothly deflected until the piezo retraces in a nonlinear pattern, different from the linear pattern we usually observe on homogeneous samples. This can be explained as follows: as the tip is pushed further down in the array, more nanotubes get into contact with the tip, gradually contributing to repulsion. This condition is reversed when the tip is retracted from the arrays, leading to a non-linear detaching curves. The adhesive force values found here come from the high van der Waals forces in the

Samples	Tips	
	Si ₁	Si ₂
Si ₁	86	96
Si ₂	94	96

Table 4.3: Adhesive forces (nN) between the Si tips and the SWNT and MWNT arrays

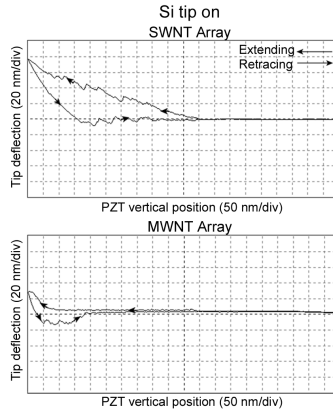


Figure 4.8: Force calibration plots of the Si tips on the SWNT and the MWNT array

contact of the tip with many different carbon nanotubes or with a large contact area between the tip and a single nanotube due to its flexibility. Although the nanotubes are hydrophobic, the capillary force may still play an important role in the adhesion between the silicon tip and the nanotube arrays due to the high surface energy of the nanotubes [36]. It has been shown that nanotube forests, with a 10-15 μm length, have an initial water contact angle of 161° ; however the droplets are not stable and eventually seep into the forest voids after a few minutes. For shorter CNTs, water droplets immediately seep into the voids, and the nanotubes are even forced into bundles under the surface tension effects of the evaporating water between the nanotubes, reducing their hydrophobicity. The force calibration plots monitored in our studies are similar to the ones presented by Decossas et al. [68] in their tests on a MWNT carpet (where the nanotubes are not aligned) with a silicon nitride

tip, and the plots reported by Yurdumakan et al. [37], obtained scanning a silicon tip on a MWNT array. A lot of variability in the value of the adhesion has been observed, and it is expected to be due to the different nanotube arrangements in different points of the samples including the packing density (Fig.4.6).

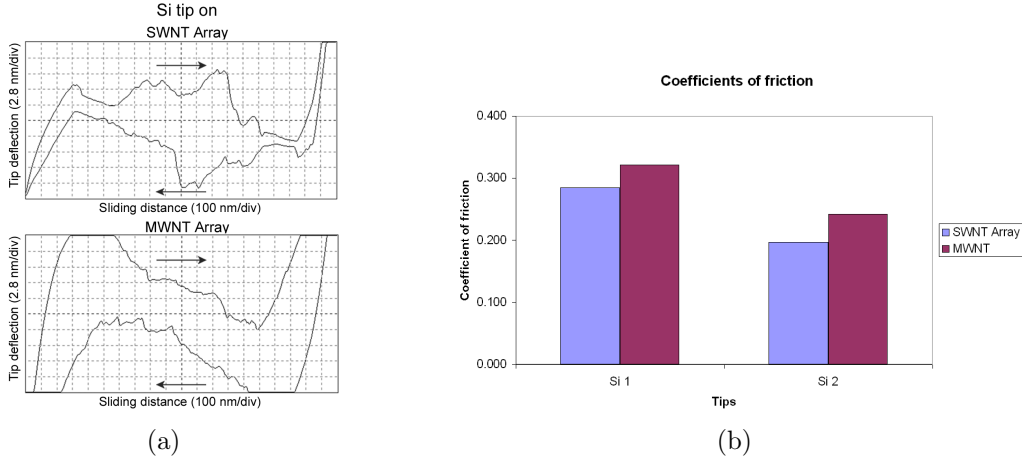


Figure 4.9: (a) Lateral deflection of the Si tip on the SWNT and the MWNT arrays during friction measurements; (b) mean values of the coefficients of friction measured with two different Si tips. The σ values are about 20% of the mean values

Samples	Tips	
	Si 1	Si 1
SWNT	0.223	0.132
MWNT	0.309	0.256

Table 4.4: Friction coefficient evaluated with two Si tips on the SWNT and the MWNT arrays

The friction data measured on the SWNT and the MWNT arrays are reported in Tab.4.4 and shown in Fig.4.9. The SWNT array showed a lower coefficient of friction than the MWNT array, similar to the trends observed for the adhesion forces. Besides the density difference, the higher stiffness of the MWNTs, compared to the SWNTs, may contribute to the high friction. SWNTs have a smaller bending

force constant, since their diameter is smaller, thus they are mechanically more flexible than MWNTs and offer less resistance to the motion of the tip.

Some influence may also occur by the cohesion forces between the nanotubes on the array, which is expected to be higher on the MWNTs array since the nanotubes density is higher than the density of the SWNT vertical array.

4.2.2 Wear tests

MWNT and Si Tip on Au film sample

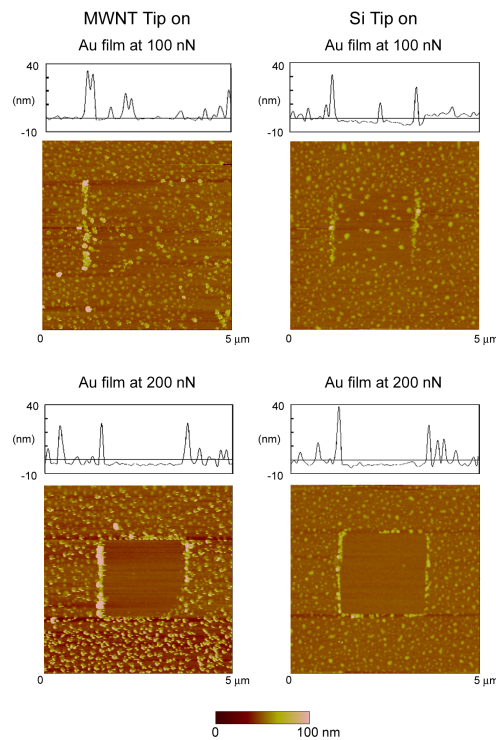


Figure 4.10: Tapping mode topographical images of the gold film after the wear test with the MWNT tip (on the left column) and the Si tip (on the right column) after the 100 nN and after the 200 nN normal loads for 10 minutes

The wear maps on the gold film are shown in Fig.4.10. It is noted that the wear

induced on the surface after the 100 nN normal load tests is very low, the material was pushed in the sliding direction of the tip. The topographical changes are more evident on the sample worn with the Si tip. In particular, it is hard to quantify a wear depth on the sample scanned with the MWNT tip, while the wear depth induced by the silicon tip is quantifiable and is about 3 nm. Low wear using the MWNT tip can possibly be due to the buckling of the carbon nanotube during the scan, which may be absorbing some of the force at contact acting as a compliant spring moderating the impact of the tip on the surface [41, 58]. Moreover, the smaller tip radius of the MWNT tip compared to the Si tip results in less contact area to the surface, which consequently does less damage [54, 42]. By applying a 200 nN load, the damages induced to the gold film are about the same for the two tips used and the average wear depths are about 5 nm for both the MWNT and the Si tips. This result may suggest that under such normal load the silicon tip holding the MWNT may also be in contact with the surface, resulting in the similar wear behavior.

Si tip on SWNT and MWNT arrays

The surface topographical images of the SWNT and the MWNT arrays captured after the wear tests are the same as in Fig.4.6, indicating that no damage was caused on either sample. The tip profiles before and after the wear tests are presented in Fig.4.11. From this figure, it is possible to see how the Si tip wears. Whereas the changes in the shape of the tip are negligible on the SWNT array after the 100 and 200 nN tests, the shape of the tip changes with MWNT array. It appears that Si tip profile after tests with MWNT array at 100 nN load gets sharper which may be due to material pick-up. The departure of the profiles at a distance of about 300 nm may occur due to artifacts in the silicon grating sample. Next, the wear volume of the tip generated by the MWNTs, calculated according to the procedure developed

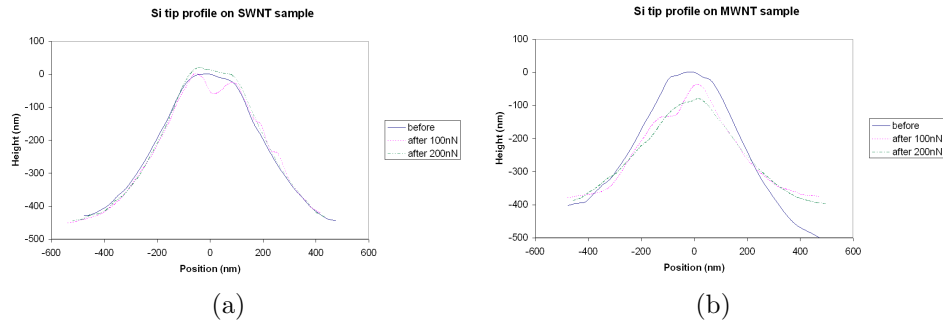


Figure 4.11: (a) Si tip profile after the wear tests on the SWNT array;(b) Si tip profile after the wear tests on the SWNT array

by Tao and Bhushan [62], is found to be $34 \cdot 10^4 \text{ nm}^3$ after the 100 nN normal load tests, and $51 \cdot 10^4 \text{ nm}^3$ after the 200 nN normal load experiments. These values are comparable to the values reported by Tao and Bhushan [62] for Si tips on Si at 100-200 nN normal load.

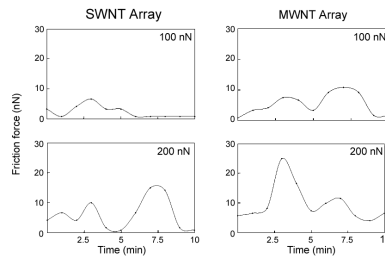


Figure 4.12: Friction forces during the wear tests with the Si tip on the CNT arrays

The friction force values obtained during the wear tests are reported in Fig.4.12. The mean value of the friction force during the entire experiment is higher when the tip is scanned on the MWNT array. It is therefore reasonable to expect wear on the tip after the tests conducted on that sample. The differences in the interactions with the SWNTs and MWNTs, and the fluctuations, have been discussed earlier in section 4.2.1.

Conclusions

In this study, a comprehensive investigation of adhesion, friction and wear of carbon nanotubes has been carried out.

By investigating the adhesion, it is concluded that when the MWNT tip is brought in and out of contact with the surface, it shows a nonlinear behavior mainly due to the bending and buckling resulting into high contact area and the sliding of the nanotube on the surface. Moreover, relatively high values for the adhesive force have been observed, and it is believed to be due to a contribution from the silicon tip, holding the MWNT tip, contacting the surface. The bending and buckling of the nanotube, in addition to the surface chemistry, may also be the reason of the slightly higher coefficient of friction observed with the MWNT tip, with respect of the values recorded for the Si and the Si_3N_4 tips on the silicon (100), single crystal aluminum and mica surfaces. When the nanotube bends, it results into a larger contact area, which causes a higher resistance to the motion.

The adhesive forces evaluated between the Si tips and the SWNT and the MWNT arrays showed a lot of variability. This is related to the density and the arrangement of the nanotubes at the interface. Moreover, the relatively high values of such forces observed on the MWNT array can be due to the presence of large van der Waals forces related to the contact of the tip with numerous nanotubes, or to a large contact area between the tip and a single nanotube. The coefficient of friction estimated for

the SWNT array is lower than the one corresponding to the MWNT array. Such observation can be the consequence of lower van der Waals forces and the larger flexibility of the single walled nanotubes, which may assist rather than oppose to the motion.

The wear tests conducted on the gold film at two normal loads, show the low damage induced by the lower load when the MWNT tip is used. This may be related to the buckling of the nanotube, which acts as a compliant spring, adsorbing part of the force transmitted by the cantilever. When the 200 nN load is applied, no difference in the wear traces can be observed on the surface scanned with either tips. It can be then concluded that such load may bring the silicon tip, holding the MWNT tip, into contact with the substrate.

Wear tests were carried out on the SWNT and the MWNT arrays using the Si tip, and their topographical images did not show any change. The tip showed a negligible wear after the test on the SWNT array. On the contrary, a larger tip wear in MWNT array can be observed. This is consistent with the friction forces monitored during the test: the mean value of the friction force between the tip and the SWNTs is slightly lower than the one recorded for the MWNTs. It can be concluded that the larger flexibility of the SWNTs plays a key role in the interaction with the tip, allowing the nanotubes to bend more than opposing to the tip motion and consequently leading to tip wear.

Bibliography

- [1] S. Iijima. *Helical microtubules of graphitic carbon*. **Nature**, 354:56–58, 1991.
- [2] M.S. Dresselhaus, G. Dresselhaus, P. Avouris, and al eds. *Carbon Nanotubes: Synthesis, Structure, Properties and Application*. Springer Berlin/Heidelberg, 2001.
- [3] T.W. Ebbesen and P.M. Ajayan. *Large-scale synthesis of carbon nanotubes*. **Nature**, 358:220–222, 1992.
- [4] S. Iijima and T. Ichihashi. *Single-shell carbon nanotubes of 1-nm diameter*. **Nature**, 363:603–605, 1993.
- [5] W.A. de Heer, W.S. Bcsa, A. Châtelain, T. Gerfin, R. Humphrey-Baker, L. Forro, and D. Ugarte. *Aligned Carbon Nanotube Films: Production and Optical and Electronic Properties*. **Science**, 268:845–847, 1995.
- [6] P. Kim and C.M. Lieber. *Nanotube nanotwizers*. **Science**, 286:2148–2150, 1999.
- [7] J. Kong, N.R. Franklin, C. Zhou, M.G. Chapline, S. Peng, K. Cho, and H. Dai. *Nanotube molecular wires as chemical sensors*. **Science**, 287:622–625, 287.
- [8] J. Nygård, D.H. Cobden, and P.E. Lindelof. *Kondo physics in carbon nanotubes*. **Nature**, 408:342–346, 2000.
- [9] Y. Nakayama and S. Akita. *Field-emission device with carbon nanotubes for a flat panel display*. **Synthetic Met.**, 117:207–210, 2001.
- [10] R.H. Baughman, A.A. Zakhidov, and W.A. de Heer. *Carbon nanotubes - the*

-
- route toward applications. *Science*, 297:787–792, 2002.
- [11] L. Dai, P. He, and S. Li. *Functionalized surfaces based on polymers and carbon nanotubes for some biomedical and optoelectronic applications*. *Nanotechnology*, 14:1081–1097, 2003.
- [12] B. Bhushan. *Handbook of Nanotechnology*. Springer, second edition.
- [13] H. Dai, J.H. Hafner, A.G. Rinzler, D.T. Colbert, and R.E. Smalley. *Nanotubes as nanoprobe in scanning probe microscopy*. *Nature*, 384:147–150, 1996.
- [14] E.S. Snow, P.M. Campbell, and J.P. Novak. *Single-wall carbon nanotube atomic force microscope probes*. *Appl. Phys. Lett.*, 80(11):2002–2004, 2002.
- [15] B. Bhushan, T. Kasai, C.V. Nguyen, and M. Meyyappan. *Multiwalled carbon nanotube AFM probes for surface characterization of micro/nanostructures*. *Microsyst. Technol.*, 2004.
- [16] C.V. Nguyen, C. So, R.M. Stevens, Y. Li, L. Delzeit, P. Sarrazin, and M. Meyyappan. *High lateral resolution imaging with sharpened tip of Multi-Walled Carbon Nanotube scanning probe*. *J. of Phys. Chem. B*, 2004.
- [17] L.S. Schadler, S.C. Giannaris, and P.M. Ajayan. *Load transfer in carbon nanotube epoxy composites*. *Appl. Phys. Lett.*, 73:3842–3844, 1998.
- [18] D. Quian, E.C. Dickey, R. Andrews, and T. Ranell. *Load transfer and deformation mechanism in carbon nanotube-polystyrene composites*. *Appl. Phys. Lett.*, 76:2868–2870, 2000.
- [19] M.J. Biercuk, M.C. Llaguno, M. Radosavljevic, J.K. Hyun, A.T. Johnson, and J.E. Fisher. *Carbon nanotube composites for thermal management*. *Appl. Phys. Lett.*, 80:2767–2769, 2002.
- [20] D. Shi, J. Lian, P. He, L.M. Wang, F. Xiao, L. Yang, M.J. Schulz, and D.B. Mast. *Plasma coating of carbon nanofibers for enhanced dispersion and interfacial bonding in polymer composites*. *Appl. Phys. Lett.*, 83:5301–5303, 2003.

-
- [21] X. Li, W. Guan, H. Yan, and L. Huang. *Fabrication and atomic force microscopy/friction force microscopy (AFM/FFM) studies of polyacrylamide-carbon nanotubes (PAM-CNTs) copolymer thin films.* **Mater. Chem. Phys.**, 88:53–58, 2004.
- [22] Z. Yang, B. Dong, Y. Huang, L. Liu, F.-Y. Yan, and H.-L. Li. *A study on carbon nanotubes reinforces poly(methyl methacrylate) nanocomposites.* **Mat. Lett.**, 59:2128–2132, 2005.
- [23] H. Lee, S. Mall, P. He, D. Shi, S. Narasimhadevara, Y. Yeo-Heung, V. Shanov, and M.J. Shulz. *Characterization of carbon nanotube/nanofiber-reinforced polymer composites using an instrumented indentation technique.* **Composites: Part B**, 38:58–65, 2007.
- [24] S.R. Dong, J.P. Tu, and X.B. Zhang. *An investigation of the sliding behavior of Cu-matrix composite reinforced by carbon nanotubes.* **Mat. Sci. Eng. A-Struct**, 313:83–87, 2001.
- [25] W.X. Chen, J.P. Tu, L.Y. Wang, H.Y. Gan, Z.D. Xu, and X.B. Zhang. *Tribological application of carbon nanotubes in a metal-based composite coating and composites.* **Carbon**, 41:215–222, 2003.
- [26] L.Y. Wang, J.P. Tu, W.X. Chen, Y.C. Wang, X.K. Lu, C. Olk, D.H. Cheng, and X.B. Zhang. *Friction and wear behavior of electroless Ni-based CNT composite coatings.* **Wear**, 254:1289–1293, 2003.
- [27] X.H. Chen, C.S. Chen, N. Xiao, H., H.B. Liu, L.P. Zhou, S.L. Li, and G. Zhang. *Dry friction and wear characteristics of nickel/carbon nanotube electroless composite deposits.* **Tribol. Int.**, 39:22–28, 2006.
- [28] S.-M. Zhou, X.-B. Zhang, Z.-P. Ding, C.-Y. Min, G.-L. Xu, and W.-M. Zhu. *Fabrication and tribological properties of carbon nanotubes reinforced Al composites prepared by pressureless infiltration technique.* **Composites: Part A**, 38:301–306, 2007.

-
- [29] Viennano, editor. Non-organic matrix materials reinforced with carbon nanotubes for space applications, 2007.
- [30] R.W. Siegel, S.K. Chang, B.J. Ash, J. Stone, P.M. Ajan, R.W. Doremus, and L.S. Schadler. *Mechanical behaviour of polymer and ceramic matrix nanocomposites*. **Scripta Mater.**, 44:2061–20614, 2001.
- [31] A. Peigney, E. Flahaut, C. Laurent, F. Chastel, and A. Rousset. *Aligned carbon nanotubes in ceramic-matrix nanocomposites prepared by high-temperature extrusion*. **Chem. Phys. Lett.**, 352:20–25, 2002.
- [32] J.-W. An, D.-H. You, and D.-S. Lim. *Tribological properties of hot-pressed alumina-CNT composites*. **Wear**, (255):677–681, 2003.
- [33] S. Fan, M.G. Chapline, N.R. Franklin, T.W. Tombler, A.M. Cassel, and H. Dai. *Self-oriented regular arrays of carbon nanotubes and their field emission properties*. **Science**, 283:512–514, 1999.
- [34] Y. Chen, D.T. Shaw, and L. Guo. *Field emission of different oriented carbon nanotubes*. **Appl. Phys. Lett.**, 76:2469–2471, 2000.
- [35] S. Shaikh, K. Lafdi, and E. Silverman. *The effect of a CNT interface on the thermal resistance of contacting surfaces*. **Carbon**, 45:696–703, 2007.
- [36] K.K.S. Lau, J. Bico, K.B.K. Teo, M. Chhowalla, G.A.J. Amaratunga, W.I. Milne, G.H. McKinley, and K.K. Gleason. *Superhydrophobic carbon nanotube forest*. **Nano Lett.**, 3(12):1701–1705, 2003.
- [37] B. Yurdumakan, N.R. Raravikar, P.M. Ajayan, and A. Dhinojwala. *Synthetic gecko foot-hairs from multiwalled carbon nanotubes*. **Chem. Comm.**, (2005):3799–3801, 2005.
- [38] L. Huang, S.P. Lau, H.Y. Yang, E.S.P. Leong, S.F. Yu, and S. Prawer. *Stable superhydrophobic surface via carbon nanotube coated with ZnO thin film*. **J. Phys. Chem. B**, 109:7746–7748, 2005.

- [39] L. Zhu, Y. Xiu, J. Xu, P.A. Tamirisa, D.W. Hess, and C.-P. Wong. *Superhydrophobicity on two-tier rough surfaces fabricated by controlled growth of aligned carbon nanotube arrays coated with fluorocarbon*. **Langmuir**, 21:11208–11212, 2005.
- [40] C.V. Nguyen, K.-J. Chao, M.D.R. Stevens, L. Delzeit, A. Casel, J. Han, and Y. Meyyappan. *Carbon nanotube tip probes: stability and lateral resolution in scanning probe microscopy and application to surface science in semiconductors*. **Nanotechnology**, 12:363–367, 2001.
- [41] T. Larsen, A. Moloni, F. Flack, M. A. Eriksson, M. G. Lagally, and C. T. Black. *Comparison of wear characteristics of etched-silicon and carbon nanotube atomic-force microscopy probes*. **Appl. Phys. Lett.**, 80(11):1996–1998, 2002.
- [42] L. Guo, R. Wang, H. Xu, and J. Liang. *Wear-resistance comparison of carbon nanotubes and conventional silicon-probes for atomic force microscopy*. **Wear**, 258:1863–1839, 2005.
- [43] S. Iijima, C. Brabec, A. Maiti, and J. Bernholc. *Structural flexibility of carbon nanotubes*. **J. Chem. Phys.**, 104:2089–2092, 1995.
- [44] B.I. Yakobson, M.P. Campbell, C.J. Brabec, and J. Bernholc. *High strain rate fracture and C-chain unraveling in carbon nanotubes*. **Comp. Mater. Sci.**, 8:341–348, 1997.
- [45] M.R. Falvo, G.J. Clary, R.M. Taylor II, V. Chi, F.P. Brooks Jr, S. Washburn, and R. Superfine. *Bending and buckling of carbon nanotubes under large strain*. **Nature**, 389:582–584, 1997.
- [46] E.W. Wong, P.E. Sheenan, and C.M. Lieber. *Nanobeam mechanics: elasticity, strength and toughness of nanorods and nanotubes*. **Science**, 277:1971–1975, 1997.
- [47] C.Q. Ru. *Effective bending stiffness of carbon nanotubes*. **Phys. Rev. B**,

- 62:9973–9976, 2000.
- [48] T. Belytschko, S.P. Xiao, G.C. Schatz, and R.S. Ruoff. *Atomistic simulation of nanotube fracture*. **Phys. Rev. B**, (65):235430–1–8, 2002.
- [49] M. Nakajima, F. Arai, L. Dong, and T. Fukua. *Measurements of the bi-linear elasticity of identical carbon nanotubes*. **Nanotechnology**, 1:156–159, 2003.
- [50] M.-F. Yu, O. Lourie, M.J. Dyer, K. Moloni, T.F. Kelly, and R.S. Ruoff. *Strength and breaking mechanism of multiwalled carbon nanotubes under tensile load*. **Science**, 287:637–640, 2000.
- [51] C. Daraio, V. F. Neterenko, J. F. Aubuchon, and S. Jin. *Dynamic nanofragmentation of carbon nanotubes*. **Nano Lett.**, 4:1915–1918, 2004.
- [52] C. Daraio, V. F. Neterenko, and S. Jin. *Highly nonlinear contact interaction and dynamic energy dissipation by forest of carbon nanotubes*. **Appl. Phys. Lett.**, 85:5724–5726, 2004.
- [53] A. Cao, P.L. Dickrell, W.G. Sawyer, M.N. Ghasemi-Nejhad, and P.M. Ajayan. *Super-compressible foamlake carbon nanotube films*. **Science**, 310:1307–1310, 2005.
- [54] B. Bhushan. *Introduction to Nanotribology*. 2002.
- [55] B. Bhushan. *Nanotribology and Nanomechanics An Introduction*. Springer Berlin Heidelberg, 2005.
- [56] H. Kinoshita, I. Kume, M. Tagawa, and N. Ohmae. *High friction of a vertically aligned carbon-nanotube film in microtribology*. **Appl. Phys. Lett.**, 2004.
- [57] V. Turq, N. Ohmae, J.M Martin, J. Fontaine, H. Kinoshita, and J.L. Loubet. *Influence of humidity on microtribology of vertically aligned carbon nanotube film*. **Tribol. Lett.**, 19(1):23–28, 2005.
- [58] C.V. Nguyen, Q. Ye, and M. Meyyappan. *Carbon nanotube tips for scanning probe microscopy: fabrication and high aspect ration nanometrology*. **Meas. Sci. Technol.**, 16:2138–2146, 2005.

-
- [59] S.D. Huang, L. Dai, , and A.W.H. Mau. *Patterned Growth and Contact Transfer of Well-Aligned Carbon Nanotube Films*. **J. Phys. Chem. B**, 103:4223–4227, 1999.
- [60] L. Qu and L. Dai. *Polymer-masking for controlled functionalization of carbon nanotubes*. **Chem. Commun.**, 2007:3859–3861, 2007.
- [61] J.-A. Ruan and B. Bhushan. *Atomic-Scale Friction Measurements Using Friction Force Microscopy: Part I - General Principles and New Measurement Techniques*. **ASME J. of Tribol.**, 116:378–388, 1994.
- [62] Z. Tao and B. Bhushan. *Surface modification of AFM silicon probes for adhesion and wear reduction*. **Tribol. Lett.**, 21(1):1–16, 2006.
- [63] S.I. Lee, S.W. Howell, A. Raman, R. Reifengerger, C.V. Nguyen, and M. Meyyappan. *Nonlinear tapping dynamics of multi-walled carbon nanotube tipped atomic force microcantilevers*. **Nanotechnology**, 15:416–421, 2004.
- [64] T.W. Tombler, C. Zhou, L. Alexseyev, J. Kong, H. Dai, L. Liu, C.S. Jayanthi, M. Tang, and S.-Y. Wu. *Reversible electromechanical characteristics of carbon nanotubes under local-probe manipulation*. **Nature**, 405:769–772, 2000.
- [65] W.C. Young and R.J. Roark. *Roark's formulas for stress and strain*. 6th edition, 2001.
- [66] C.J. Lee, D.W. Kim, T.J. Lee, Y.C. Choi, Y.S. Park, Y.H. Lee, and et al. *Synthesis of aligned carbon nanotubes using thermal chemical vapor deposition*. **Chem. Phys. Lett.**, 312:461–468, 1999.
- [67] A.H. Barber, S.R. Cohen, and H.D. Wagner. *Static and dynamic wetting measurements of single carbon nanotubes*. **Phys. Rev. Lett.**, 92(18):186103–1–4, 2004.
- [68] S. Decossas, G. Cappello, G. Poignant, L. Patrone, A.M. Bonnot, F. Comin, and J. Chevrier. *Interaction forces between carbon nanotubes and an AFM tip*. **Europhys. Lett.**, 53(6):742–748, 2001.

-
- [69] V.L. Mironov. *Fondamenti di microscopia a scansione di sonda*. Technical report, Accademia Russa delle Scienze, Istituto per la fisica delle microstrutture, 2004.
- [70] M. Salerno. *Microscopia 2000, l'analisi odierna dell'estremamente piccolo, con particolare riguardo alle microscopie a scansione di sonda*. 1999.
- [71] R. Campbell. *Recent Advances in Scanning Probe Microscopy*. September 2003.
- [72] Dr. R. Owen. *A practical guide to AFM force spectroscopy and data analysis*. 2004.
- [73] D. Sarid, J.P. Hunt, R.K. Workman, X. Yao, and C.A. Peterson. *The role of adhesion in tapping-mode atomic force microscopy*. **Appl. Phys. A**, 1998.
- [74] Digital Instruments Veeco Metrology Group. *MultiModeTM SPM Instruction Manual*, 1999.
- [75] B. Bhushan. *Springer Handbook of Nanotechnology*. Springer, 2004.
- [76] D.F. Ogletree, R.W. Carpick, and M. Salmeron. *Calibration of frictional forces in atomic force microscopy*. **Rev. Sci. Instrum.**, 67(9):3298–3306, 1996.
- [77] M. Varenberg, I. Etsion, and G. Halperin. *An improved wedge calibration method for lateral force in atomic force microscopy*. **Rev. Sci. Instrum.**, 74(7):3362–3367, 2003.
- [78] Y.-L. Wang, X.-Z. Zhao, and F.-Q. Zhou. *Improved parallel scan method for nanofriction force measurement with atomic force microscopy*. **Rev. Sci. Instrum.**, 78(03617):1–3, 2007.
- [79] L.P. Birò, G.I. Màrk, J. Gyulai, and P.A. Thiry. *STM and AFM investigation of carbon nanotubes*. **Mater. Struct.**, 6(2):104–108, 1999.
- [80] J. Cumings and A. Zettl. *Low-friction nanoscale linear bearing realized from multiwall carbon nanotubes*. **Science**, 289:602–604, 2000.
- [81] C. Journet, W.K. Maser, P. Bernier, A. Loiseau, and M. Lamy de la Chapelle.

-
- Large-scale production of single-wall carbon nanotubes by the electric-arc technique. **Nature**, 388:756–758, 1997.*
- [82] M. Endo, K. Takeuchi, K. Kobori, K. Takahashi, H.W. Kroto, and A. Sakar. *Pyrolytic carbon nanotubes from vapor-grown carbon fibers. **Carbon**, 33(7):873–881, 1995.*
- [83] B.C. Satishkumar, A. Govindaraj, and C.N.R. Rao. *Bundles of aligned carbon nanotubes obtained by the pyrolysis of ferrocene-hydrocarbon mixtures: role of the metal nanoparticles produced in situ. **Chem. Phys. Lett.**, 307:158–162, 1999.*
- [84] M. Terrones, N. Grobert, J. Olivares, J.P. Zhang, and al. *Controlled production of aligned-nanotube bundles. **Nature**, 388:52–55, 1997.*
- [85] Z.F. Ren, Z.P. Huang, J.W. Xu, J.H. Wang, P. Bush, M.P. Siegal, and P.N. Provencio. *Synthesis of large arrays of well-aligned carbon nanotubes on glass. **Nature**, 282:1105–1107, 1998.*
- [86] Y.C. Choi, Y.M. Shin, Y.H. Lee, B.S. Lee, and et al. *Controlling the diameter, growth rate, and density of vertically aligned carbon nanotubes synthesized by microwave plasma-enhanced chemical vapor deposition. **Appl. Phys. Lett.**, 76(17):2367–2369, 2000.*
- [87] A.M. Bonnot, M.N. Séméria, J.F. Boronat, T. Fournier, and L. Pontonnier. *Investigation of the growth mechanism and electron emission properties of carbon nanostructures prepared by hot-filament chemical vapor deposition. **Diam. Relat. Mater.**, 9:852–855, 2000.*
- [88] J.-P. Salvetat, J.-M. Bonard, N.H. Thomson, A.J. Kulik, I. Forrò, W. Benoit, and L. Zuppiroli. *Mechanical properties of carbon nanotubes. **Appl. Phys. A**, 69:255–260, 1999.*
- [89] M.-F. Yu, B.S. Files, S. Arepall, and R.S. Ruoff. *Tensile loading of ropes of single wall carbon nanotubes and their mechanical properties. **Phys. Rev.***

- Lett.*, 84(24):5552–5555, 2000.
- [90] H.J. Qi, K.B.K. Teo, K.K.S. Lau, M.C. Boyce, W.I. Milne, J Robertson, and K.K. Gleason. *Determination of mechanical proprieties of carbon nanotubes and vertically aligned carbon nanotube forests using nanoindentation.* **J. Mech. Phys. Sol.**, 51:2213–2237, 2003.
- [91] Z. Tao and B. Bhushan. *Wetting properties of AFM probes by means of contact angle measurements.* **J. Phys. D**, 39:3858–3862, 2006.